THESIS

Direct measurement of mirror thermal noise

Kenji Numata

Department of Physics, Faculty of Science,
University of Tokyo

December 2002

History		
Version 1.0	Feb. 28th, 2003	Library version
Version 1.1	Dec. 6th, 2003	Note added on page 104 for distribution version

Test cavity mirrors

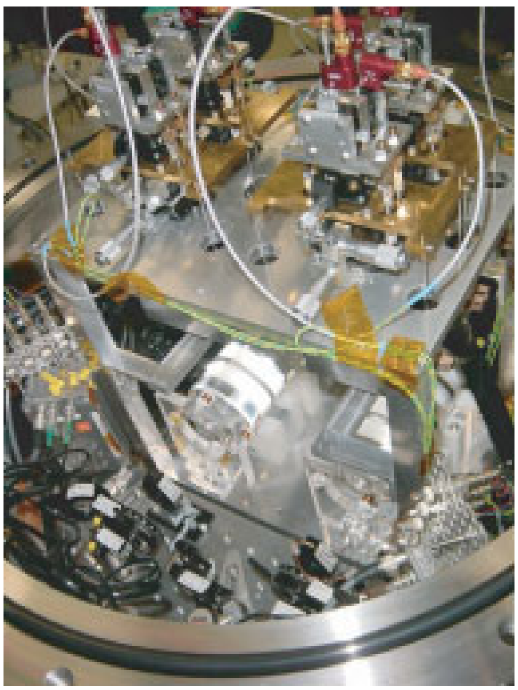

Suspension system for test cavity

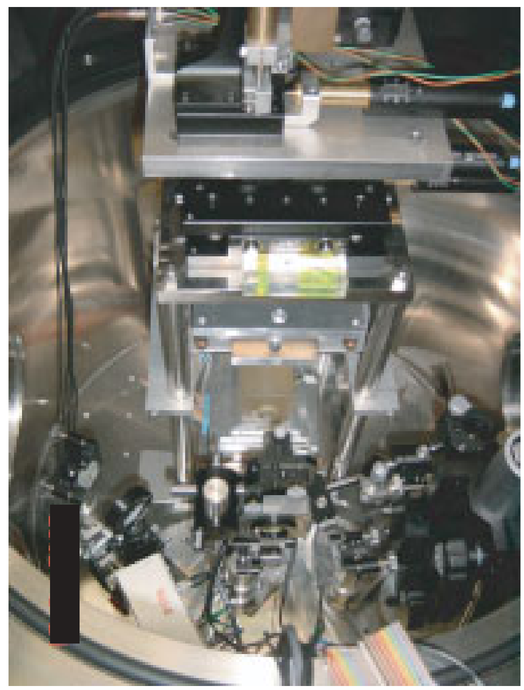

Suspension system for reference cavity

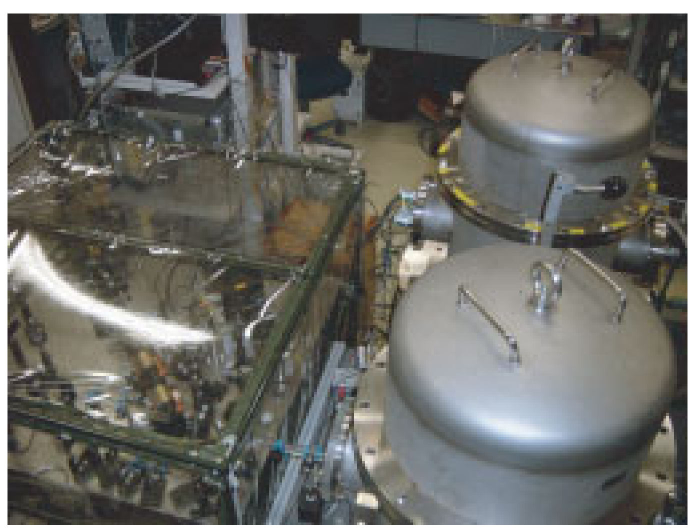

Whole setup

Contents

Chapter 1

Introduction

Gravitational waves are ripples of space-time which propagate across the universe at the speed of light. The gravitational waves were derived from the Einstein equation in the general theory of relatively [1]. Their existence was indirectly proved by an observation of a binary pulsar PSR1913+16 [2]. The observed decrease in the period of its revolution agrees with the theoretical expectation of orbital decay due to gravitational radiation. There is no doubt that gravitational waves exist.

The direct detection of gravitational waves, however, has not been achieved since the experiments were started using a resonant-type detector in the 1960s. Their detection has significant meaning from the viewpoint of physics. Such detection will give a direct verification of the general theory of relativity and other theories for gravitation. Also, direct detection is meaningful for astronomy. These gravitational waves are radiated from dynamic events in the universe such as coalescence of neutron star binaries and supernova explosions. Gravitational waves should bring new information about them to us and are expected to be a powerful window to observe the universe.

In this background, large-scale interferometric gravitational wave detectors are under construction around the world taking advantage of remarkable developments in laser optics and precision measurements in recent years [3, 4, 5, 6]. The interferometric gravitational wave detector detects the gravitational wave as a change in interference fringes caused by the variation of the proper distance between two mirrors. The advantage of the interferometric detector is in its wide observation band, typically 100 Hz to 1 kHz. It will enable us to observe the waveform of the gravitational wave directly.

However, in its observation band, there is an inevitable noise source – the mirror thermal noise. The mirror thermal noise is thermal fluctuation of the mirror surface, on which the interferometer detects the variation of the distance. The thermal fluctuation directly obscures the sensitive measurement at the most important frequency band. Therefore, a clear understanding of the noise and a reduction of the noise are the most required issues in developing the interferometric gravitational wave detectors. However, because the amplitude of the mirror thermal noise to be measured is extremely small, the research had been limited to theoretical estimations or indirect experiments.

According to the fluctuation-dissipation theorem [7, 8, 9, 10], the amplitude of the thermal fluctuation is related to the mechanical losses in the mirror. Two kinds of mirror thermal noises, which could limit the sensitivity of the detector, have been predicted theoretically, depending on the origin of the loss: Brownian noise [11] and thermoelastic noise [12]. Brownian noise is associated with the all forms of dissipation that are homogeneously distributed mechanisms within a material. The origin of the thermoelastic noise is the thermoelastic dissipation in the mirror, which is caused by heat flow along the temperature gradients. Researchers have calculated analytically the amplitude of these thermal noises [13, 14, 15, 16]. We ourselves also established a numerical calculation method for Brownian noise, which is much more generalized than other analytic calculations.

According to the established theories, the amplitude of the Brownian noise should be inversely proportional to the intrinsic mechanical loss. Thus, it should be possible to indirectly evaluate the mirror thermal noise by measuring the intrinsic loss. Based on this consideration, many researchers tried to find low loss materials, or tried to measure the intrinsic loss accurately [17, 18, 19, 20, 21, 22]. Surely the measurement of the loss is practically easier than the measurement of thermal fluctuation, but the loss measurements had a substantial problem: because of the loss due to the support for the measurement, intrinsic loss could not be measured directly. To solve the problem, a decisive measurement technique was proposed by the authors [23, 24]. Our system, called nodal support system, does not introduce any external loss to the sample, by supporting it at their nodal point. As an established system, it is working as a powerful tool to measure the intrinsic loss directly. Through these works, the indirect experiment on the mirror thermal noise is going to be completed.

The biggest problem is whether the developed theoretical and indirect experimental researches had been correct or not. However, before the research described in this thesis, the measurement of thermal noise in mechanics had been demonstrated only in simple systems, such as cantilevers [25, 26], torsion pendulums [27], resonance of elastic body [28], and so on. The mirror thermal noise had not been observed experimentally. The experimental demonstration to directly measure the mirror thermal noise was the significant work to be done for the interferometric gravitational wave detectors. We thus performed the experiment for the direct measurement on a laboratory scale, which imitated the interferometric detectors.

To measure the two kinds of mirror thermal noises — Brownian noise and the thermoelastic noise —, we chose two kinds of mirror substrate: BK7 and CaF_2. The mechanical losses of these substrates were measured by our nodal support system. Based on the measurement and developed theories, these thermal noise levels were theoretically predicted. We set them as our goal sensitivities. Every component was specially and carefully designed to achieve the goal sensitivity without loosing a similarity with the real interferometric detectors. The measurement principle is simple: a frequency-stabilized laser reads a mirror thermal noise in two equivalent short Fabry-Perot cavities. The short cavity length makes the frequency noise of the laser smaller. It also enhances the mirror thermal noise and eases handling. The readout signals from the two equivalent cavities are subtracted, reducing the common mode noise between the two cavities further.

By suppressing any other noises in the cavities, the interferometer successfully achieved high enough sensitivity to observe mirror thermal noise over three decades (100 Hz to 100 kHz). It enabled us to observe clearly the thermal noise at off-resonance and on-resonance of the mirror. Measured Brownian noise and the thermoelastic noise agreed quite well with the corresponding theories. The validity of the present theories, including the fluctuation-dissipation theorem, was well confirmed. The interferometer still has sufficient sensitivity to measure smaller thermal noise. This means that the setup works as a test bench to measure thermal noise just by replacing the mirror. The developed system will play an important role in the investigation of the mirror thermal noise along with the developed theoretical calculations and the indirect experimental technique.

In the following chapters we describe our research on the mirror thermal noise. In Chapter 2, the physical background of gravitational waves, and fundamentals of interferometric detectors and its noise sources are described. In Chapter 3, the theories for the mirror thermal noises are shown. We also review the past experimental approaches on the mirror thermal noise. In Chapter 4, the experimental setup to measure the mirror thermal noise is described. We constructed the interferometer described here and measured two kinds of mirror substrates. In Chapter 5, the measured results by the interferometer are described. We show the measured displacement noises in the two substrates by comparing the theoretical results and our noise analysis. In Chapter 6, we discuss the measured thermal noises mainly around mirror resonances, and the future possibility of the developed interferometer. In Chapter 7, the achievements of this research are summarized. In Appendix A, we introduce the method that we have developed to calculate thermal noise generally and numerically. In Appendix B, we show the measured results of the intrinsic loss of the materials by the nodal support technique.

Chapter 2

Interferometric gravitational wave detector

Gravitational waves are ripples of space-time that propagate across the universe at the speed of light. Einstein theoretically found the existence of the gravitational wave in 1916 by solving the Einstein equation in general relativity in a weak gravitational field within a linear approximation [1]. About 60 years later, in 1978, the existence of the gravitational waves was proved indirectly by J.H. Taylor and R.A. Hulse, who observed binary pulsar PSR1913+16 [2]. However, direct detection was not achieved until after J. Weber started his unsuccessful experiment using a resonant-type detector in the 1960s [29]. Currently, more effective detectors, large-scale interferometric gravitational wave detectors, are under construction to detect gravitational waves over a wide frequency range. The research of this thesis is to study the thermal noises in the interferometric detectors mirror, which prevent the direct detection of gravitational waves in their observation band.

In this chapter, we discuss the physical background of this research. First, we briefly introduce the theory of gravitational waves. The general theory of relativity, the wave solutions of Einstein equation, and its effects on free particles are discussed. Second, we consider generation of gravitational waves. The astronomical events, which radiate gravitational waves, are shown here. Then, we mention the principle of the interferometric gravitational wave detector and current projects in the world. Finally, the noise sources of the interferometric gravitational wave detectors are discussed. We will see how the mirror thermal noise limits the sensitivity of the detector, and this is the most significant issue to be investigated.

2.1 Theory of gravitational waves

The general theory of relativity is believed to be the fundamental theory that governs all of the universe. The gravitational waves are derived from Einstein equations in the general theory of relativity as wave solutions. In this section, we deduce the wave solutions and then consider the effects on free particles, which are closely related to the principle of the interferometric gravitational wave detectors [30].

2.1.1 General theory of relativity

In the general theory of relativity, the proper distance, ds, between two separate points in space-time, is represented by a metric tensor, $g_{\mu\nu}$.

$$ds^2 = g_{\mu\nu} dx^\mu dx^\nu. \tag{2.1}$$

From the metric tensor $g_{\mu\nu}$, the Christoffel symbol, $\Gamma^\mu{}_{\nu\lambda}$, and the Riemann tensor, $R^\mu{}_{\nu\alpha\beta}$, are defined as follows:

$$\Gamma^\mu{}_{\nu\lambda} = \frac{1}{2} g^{\mu\alpha} (g_{\alpha\mu,\lambda} + g_{\alpha\lambda,\mu} - g_{\mu\lambda,\alpha}), \tag{2.2}$$

$$R^\mu{}_{\nu\alpha\beta} = \Gamma^\mu{}_{\nu\beta,\alpha} - \Gamma^\mu{}_{\nu\alpha,\beta} + \Gamma^\mu{}_{\gamma\alpha} \Gamma^\gamma{}_{\nu\beta} - \Gamma^\mu{}_{\gamma\beta} \Gamma^\gamma{}_{\nu\alpha}. \tag{2.3}$$

From this, the Ricci tensor $R_{\mu\nu}$, the Ricci scalar R, and the Einstein tensor $G_{\mu\nu}$ are defined.

$$R_{\mu\nu} = R^\alpha{}_{\mu\alpha\nu}, \tag{2.4}$$

$$R = R^\alpha{}_\alpha, \tag{2.5}$$

$$G_{\mu\nu} = R_{\mu\nu} - \frac{1}{2} g_{\mu\nu} R. \tag{2.6}$$

The Einstein equation is then

$$G_{\mu\nu} = \frac{8\pi G}{c^4} T_{\mu\nu}. \tag{2.7}$$

Here, G and c are the gravitational constant and the speed of light, respectively. The $T_{\mu\nu}$ is the energy-momentum tensor which represents the distribution of mass and energy in time-space. The Eq.(2.7) states that the gravitation exists if the mass exists. However, even in vacuum ($T_{\mu\nu} = 0$), there can be a gravitational field that propagates at the speed of light like an electro-magnetic wave.

2.1.2 Wave solutions of Einstein equation

The flat space-time, Minkowski space-time $\eta_{\mu\nu}$ is the solution of Eq.(2.7) in vacuum. We introduce a small perturbation $h_{\mu\nu}$ from the $\eta_{\mu\nu}$:

$$g_{\mu\nu} = \eta_{\mu\nu} + h_{\mu\nu}. \tag{2.8}$$

Here, $h_{\mu\nu}$ is satisfying $|h_{\mu\nu}| \ll 1$. By substituting this, the Eq.(2.7) is rearranged as[1],

$$\left(-\frac{1}{c^2}\frac{\partial^2}{\partial t^2} + \nabla^2 \right) h_{\mu\nu} = 0. \tag{2.9}$$

This equation dictates that the perturbation $h_{\mu\nu}$ propagates at the speed of light. This is the gravitational wave. By adopting a Transverse Traceless (TT) Gauge Transformation, the wave solution of this equation, which propagates in the z-direction, is described as,

$$h_{\mu\nu} = \begin{pmatrix} 0 & 0 & 0 & 0 \\ 0 & h_+ & h_\times & 0 \\ 0 & h_\times & -h_+ & 0 \\ 0 & 0 & 0 & 0 \end{pmatrix} e^{-i\omega(t-z/c)}. \tag{2.10}$$

The $h_{\mu\nu}$ has the two independent polarizations:

$$h_{\mu\nu} = h_+ e^{-i\omega(t-z/c)} + h_\times e^{-i\omega(t-z/c)}. \tag{2.11}$$

Here,

$$h_+ = \begin{pmatrix} 0 & 0 & 0 & 0 \\ 0 & h_+ & 0 & 0 \\ 0 & 0 & -h_+ & 0 \\ 0 & 0 & 0 & 0 \end{pmatrix}, h_\times = \begin{pmatrix} 0 & 0 & 0 & 0 \\ 0 & 0 & h_\times & 0 \\ 0 & h_\times & 0 & 0 \\ 0 & 0 & 0 & 0 \end{pmatrix}. \tag{2.12}$$

The h_+ is called $+$-polarization or plus mode, and the $h_\times$ is called $\times$-polarization or cross mode.

2.1.3 Effects on free particles

Here we describe the effect of the gravitational waves on free particles. We consider two nearby particles whose positions are $(0, 0, 0)$ and $(\epsilon, 0, 0)$ in the TT gauge. We assume that they are initially at rest. When the gravitational waves pass through the particles, the proper distance Δl between these two free masses changes as follows:

$$\Delta l \equiv \int |ds^2|^{\frac{1}{2}} = \int |g_{\alpha\beta}dx^\alpha dx^\beta|^{\frac{1}{2}} \tag{2.13}$$

[1]We neglect second order term of $h_{\mu\nu}$ and assumed $h^\nu{}_{\mu,\nu} - h^\rho{}_{\rho,\mu}/2 = 0$.

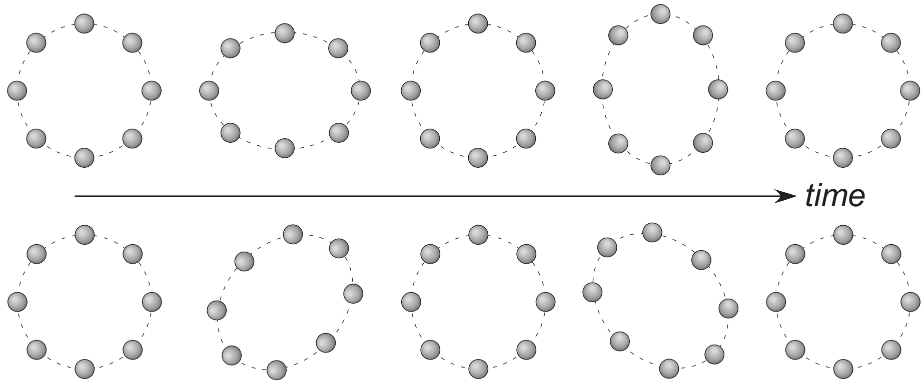

Figure 2.1: Illustration of the effect of a gravitational wave on free particles; The effect of the gravitational wave is illustrated by displaying its effect on a ring of free particles arranged in a plane, which is perpendicular to the propagation direction of the wave. Above: +-mode. Below: ×-mode.

$$= \int_0^{\epsilon} |g_{xx}|^{\frac{1}{2}} dx \simeq |g_{xx}(x=0)|^{\frac{1}{2}} \epsilon \tag{2.14}$$

$$\simeq \left[1 + \frac{1}{2} h_{xx}(x=0)\right] \epsilon. \tag{2.15}$$

This equation means that the proper distance changes with time. Figure 2.1 illustrates the consequence of the effect on a ring of free particles arrayed in a plane perpendicular to the direction of propagation of the gravitational wave. The two polarizations distort the original ring in different ways if the wave carries the +-polarization (above) and the ×-polarization (below). Thus, the gravitational waves can be detected by comparing the position of free masses.

2.2 Generation of gravitational waves

In this section, we describe the gravitational wave sources, which may cause distance changes of detectable amplitude. The only reasonable sources are astronomical dynamic events.

2.2.1 Radiation formula

According to the radiation formula for the gravitational waves, the radiation amplitude is expressed as

$$h_{ij} = -\frac{2G}{c^4} \frac{\ddot{D}_{ij}}{r}, \tag{2.16}$$

where r is the distance from the source. The D_{ij} is the standard trace-free quadrupole tensor represented by,

$$D_{ij} = \int \rho \left(x_i x_j - \frac{1}{3}\delta_{ij} r^2 \right) d^3x. \tag{2.17}$$

Here ρ is the density of the source. Because the gravitational wave radiation is a quadrupole radiation, as these equations show, it cannot be generated by spherical systems. Even when the system is axially symmetric, it never produces radiation if the system is stationary. Also, the mass must be huge to generate a detectable amplitude of gravitational waves[2]. Therefore, the sources, which radiate detectable gravitational waves, are limited to dynamic, non-axial symmetric, and astronomical events, in which huge masses and energies are related.

2.2.2 Gravitational wave sources

In this section we briefly survey some of the gravitational-wave sources predicted by the current astrophysical theory. Expediently, we categorize the sources into high-frequency sources and low-frequency sources [31].

High-frequency sources

High frequency (1 Hz∼10 kHz) gravitational waves are the target of the ground-based interferometric detectors.

The most likely source in this frequency range is the coalescence of neutron star binaries. The two stars increase their rotational frequency, and the gravitational wave frequency until they collapse, loosing rotational energy as gravitational radiation. The amplitude of the gravitational wave also increases during this process, resulting in a "chirp" of the gravitational wave. The frequency is estimated to grow up to 1 kHz according to the calculation using the Post-Newtonian approximation. For the coalescence of the neutron star binaries, the amplitude of the gravitational wave is expected to be $h \sim 10^{-17}$ within our galaxy (∼20 kpc), and $h \sim 10^{-21}$ for sources as far as the Hercules cluster (∼200 Mpc).

Other possible sources in this frequency range are supernova explosions. If the explosion has non-axial symmetry, the explosion emits a burst of gravitational waves. The amplitude of the gravitational wave from these sources is estimated to be $h \sim 10^{-21}$ within the Virgo cluster (∼15 Mpc), and its event rate is estimated to be a few times per year[3].

[2] The c^4 term in Eq.(2.16) makes the h_{ij} smaller.
[3] These are strongly dependent on theories or hypotheses.

There are continuous gravitational wave source such as pulsar rotations or vibrations. They are believed to radiate gravitational waves, whose frequency is twice their rotational or vibrational frequency. Although, the effects are weak because of their small sustainable asymmetries, typically $h \sim 10^{-25}$, they could be detectable by ground-based detectors by performing a long-term observation.

Low-frequency sources

In the low frequency region (10^{-7} Hz to 1 Hz), there are several astronomically important sources. They are the target of the future space gravitational wave antennas, such as LISA [32] and DECIGO [33], because the seismic noise inhibits our observation of them on the ground.

The most certain source is the continuous wave from binaries of a neutron star or a white dwarf. Since their position and their frequencies are already well known by observations using electro-magnetic waves, they will be surely detected by the space antennas. The evolutionary scenario that is expected in neutron star binaries is believed to apply also to more massive star binaries, such as neutron star (NS) - black hole (BH) binaries or BH-BH binaries. They will radiate the gravitational wave more strongly because of their larger mass. Unfortunately, no location of such a system is known yet. Another scenario related to BH gravitational wave radiation is the formation of massive black holes.

Just as the cosmic microwave background was left after the Big Bang, a background of gravitational wave as well should have been left at that time. This is also an assured continuous wave source. Other processes to make background gravitational wave radiation are from inflation of the universe, cosmic strings and so on. These cosmological gravitational waves are believed to be in a very low frequency range ($< 10^{-3}$ Hz). The amplitude is related by cosmology to the critical energy density of the universe. Thus, the detection of background gravitational waves is expected to reveal a lot about the evolution of the universe.

2.3 Interferometric gravitational wave detectors

To detect the gravitational waves mentioned in the previous section, several ground-based interferometric gravitational wave detectors are under construction or in early operation. In this section, we first describe the principle of the interferometric gravitational wave detector. Then we mention the current interferometric ground-based detectors, which have kilometer class optical path length.

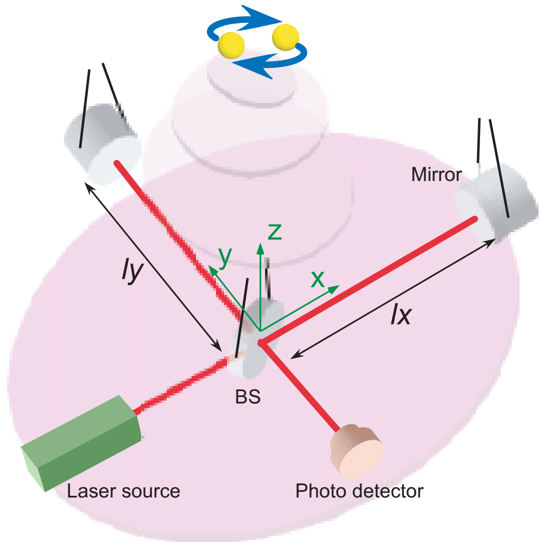

Figure 2.2: Illustration of Michelson interferometer as a gravitational wave detector; BS: Beam splitter.

2.3.1 Principle of the interferometric detector

The principle of the interferometric gravitational wave detector is the detection of the change in distance caused by the gravitational waves using a Michelson interferometer.

Figure 2.2 illustrates the Michelson interferometer as the gravitational wave detector. The optics are suspended as a pendulum so as to act as free masses in the horizontal direction above their resonant frequency. The emitted beam from the laser source is divided into two directions by a beam splitter, and reflected back by two mirrors, and then interferes at the photo detector. When a gravitational wave, which carries the +-polarization, comes from the z-direction, the proper distance ds^2 is given by,

$$ds^2 = -c^2dt^2 + (1 + h(t))dx^2 + (1 - h(t))dy^2 + dz^2. \tag{2.18}$$

For the light which propagates on the x-axis, this can be rewritten as,

$$\frac{dx}{dt} = \pm\frac{c}{\sqrt{1 + h(t)}}, \tag{2.19}$$

because $dy = dz = 0$ and $ds^2 = 0$. Here, the sign $\pm$ represents the direction of light propagation. We consider the phase of the light at time t. We assume that the light entered into the interferometer at time t_1, and round-tripped over a distance of l_x. By integrating Eq.(2.19) from time t_1 to t, we obtain,

$$\int_{t_1}^{t} \frac{dt'}{\sqrt{1 + h(t')}} = \frac{1}{c}\left(\int_0^{l_x} dx + \int_{l_x}^{0} (-dx)\right) = \frac{2l_x}{c}, \tag{2.20}$$

for the right term. Since the amplitude of the gravitational waves is small ($h \ll 1$), the left term is approximated as,

$$\int_{t_1}^{t}\left(1-\frac{1}{2}h(t')\right)dt' \simeq (t-t_1)-\frac{1}{2}\int_{t-\frac{2l_x}{c}}^{t} h(t')dt'. \tag{2.21}$$

Therefore, the round-trip phase for x-direction light $\phi_x(t)$ is represented by,

$$\phi_x(t) = \Omega t_1 = \Omega\left[t-\frac{2l_x}{c}-\frac{1}{2}\int_{t-\frac{2l_x}{c}}^{t} h(t')dt'\right], \tag{2.22}$$

where Ω is the angular frequency of the light. The round trip phase of the beam that propagates along y-axis, $\phi_y(t)$, is obtained similarly — just the sign of the gravitational wave is different:

$$\phi_y(t) = \Omega t_2 = \Omega\left[t-\frac{2l_y}{c}+\frac{1}{2}\int_{t-\frac{2l_y}{c}}^{t} h(t')dt'\right]. \tag{2.23}$$

Here, t_2 is the time when the light entered into the y-arm, and l_y is the y-arm length. As a result, the relative phase difference of these two lights becomes

$$\Delta\phi(t) = \phi_x(t)-\phi_y(t) = -\frac{2\Omega(l_x-l_y)}{c}-\Delta\phi_{\mathrm{GR}}(t), \tag{2.24}$$

$$\Delta\phi_{\mathrm{GR}}(t) = \Omega\int_{t-\frac{2l}{c}}^{t} h(t')dt'. \tag{2.25}$$

To obtain these equations, we used the approximation of $l_x \simeq l_y = l$. This Eq.(2.25) represents the effect of the gravitational wave on the interfered light. By decomposing $h(t)$ into Fourier components as

$$h(t) = \int h(\omega)e^{i\omega t}d\omega, \tag{2.26}$$

the gravitational-wave effect becomes,

$$\Delta\phi_{\mathrm{GR}}(t) = \int h(\omega)e^{i\omega t}H_{\mathrm{MI}}(\omega)d\omega, \tag{2.27}$$

$$H_{\mathrm{MI}}(\omega) = \frac{2\Omega}{\omega}\sin\left(\frac{l\omega}{c}\right)e^{-il\omega/c}. \tag{2.28}$$

This $H_{\mathrm{MI}}(\omega)$ is the transfer function from the incoming gravitational wave to the phase change of the Michelson interferometer. If we fix the observation frequency as $\omega = \omega_{\mathrm{obs}}$, its absolute value is maximized at the certain length, l_{opt}:

$$l_{\mathrm{opt}} = \frac{\pi c}{2\omega_{\mathrm{obs}}} = 250\ [\mathrm{km}]\left(\frac{300\mathrm{Hz}}{f}\right). \tag{2.29}$$

Here, f is the frequency which satisfies $f = \omega_{\mathrm{obs}}/2\pi$.

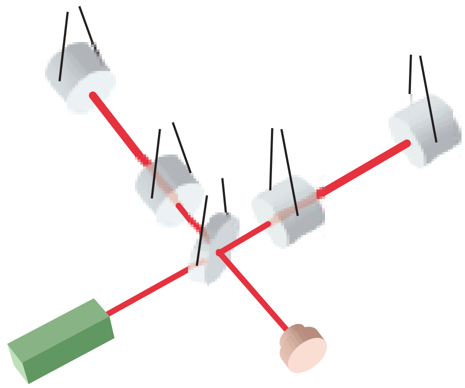

Figure 2.3: Fabry-Perot Michelson interferometer.

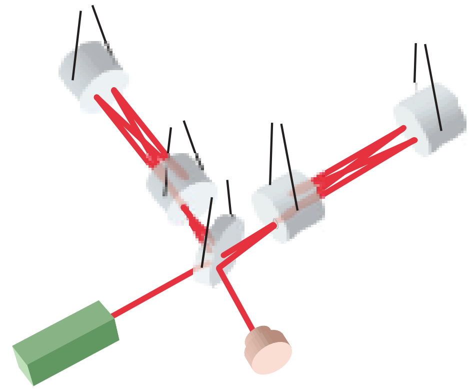

Figure 2.4: Delay-Line Michelson interferometer.

Table 2.1: Projects of large-scale interferometers for gravitational wave detection; FP: Fabry-Perot type, DL: Delay line type.

Project	Country	Arm length	Type	Site	Observation start
LIGO	USA	4 km(×2)	FP	Hanford/Livingston	2002
VIRGO	FRA/ITA	3 km	FP	Pisa	2003
GEO	GER/UK	600 m	DL	Hannover	2001
TAMA	JPN	300 m	FP	Mitaka	2000

2.3.2 Large-scale interferometric detectors

Based on the above-described principle, large-scale interferometric gravitational wave detectors are currently under construction in the world.

For a ground-based detector which targets a few hundred Hz of the gravitational wave, it is not realistic to adopt an arm length of $\sim 100\,\mathrm{km}$ as the Eq.(2.29) requires. Few kilometer arm length is a practical limit. Therefore, in order to increase the interaction time between the gravitational wave and the interferometer without increasing the physical arm length beyond reasonable lengths, one of two kinds of configuration is usually adopted: Fabry-Perot type (Fig.2.3) or Delay-line type (Fig.2.4). The former has Fabry-Perot cavities in the arms, in which the light resonate between the two faced mirrors. The latter uses optical delay lines to generate a physically long arm length by folding several optical paths in shorter arms.

Table 2.1 shows the running large-scale projects. There are four projects: LIGO [3], VIRGO [4], GEO [5], and TAMA [6]. Except for GEO, every project adopted Fabry-Perot cavities in the arms to enhance the phase change inside the arms. The research on this thesis is mainly on the mirror thermal noise in the Fabry-Perot cavities.

2.4 Noise sources of the interferometer

There are many noise sources that limit the sensitivity of the interferometer. In this section, several possible noise sources are explained. In the detectors, every displacement of the mirror and of its surface becomes noise, because the interferometer cannot distinguish between these displacements and the path-length change caused by the gravitational waves. We divide the noises in the interferometer into the following four categories:

- **Thermal noise**: mirror thermal noise, suspension thermal noise, and others.
- **Optical readout noise**: shot noise and radiation pressure noise.
- **Noises in the laser source**: laser frequency noise and laser intensity noise.
- **Non-fundamental noises**: seismic noise, electric circuit noise, and residual gas noise.

We describe the four categories in this order[4]. Finally, a typical sensitivity curve of the gravitational wave detector is shown.

2.4.1 Thermal noise

According to the fluctuation-dissipation theorem, a body in the heat bath with a finite temperature is buffeted by a fluctuating force, whose amplitude is proportional to the mechanical losses in the body itself. The surface thermal motion of the mirror is called mirror thermal noise, and the fluctuating motion of the entire mirror body as a pendulum is called suspension thermal noise.

Mirror thermal noise

There are two kinds of mirror thermal noises considered[5].

[4]Because, displacement noises inside Fabry-Perot-Michelson type gravitational wave detectors differ from that in a single Fabry-Perot cavity except for a simple factor in many cases, we consider the noise in the single Fabry-Perot cavity for simplification.

[5]The mirror thermal noise is the main topic of this thesis. Its details are discussed in the next chapter.

The first is the Brownian noise, which couples with the background loss of the mirror substrate $\phi_{\rm sub}(\omega)$. Its spectral density is estimated by [13, 15],

$$\delta x_{\rm Brown} = \left[\frac{4k_{\rm B}T}{\omega}\frac{1-\sigma^2}{\sqrt{\pi}E_0 w_0}\phi_{\rm sub}(\omega)\right]^{\frac{1}{2}} \ [\mathrm{m}/\sqrt{\mathrm{Hz}}] \tag{2.30}$$

in the frequency range below the mechanical resonances of the mirror. Here, $k_{\rm B}$ is the Boltzmann constant[6], T is the temperature, σ is the Poisson ratio of the substrate material, E_0 is the Young's modulus, and ω is the angular frequency ($\omega = 2\pi f$). w_0 is the beam radius on mirror [7]. Even though the exact origin of the mechanical loss $\phi_{\rm sub}(\omega)$ is unknown, it is usually assumed to be frequency independent $\phi_{\rm sub}(\omega) = \phi_{\rm sub}$. The amplitude of the spectrum depends only on the mechanical parameters including the mechanical loss and the beam radius. By making the beam radius larger, or by adopting a material which has smaller mechanical loss $\phi_{\rm sub}$, the Brownian noise is lowered.

The second mirror thermal noise is the thermoelastic noise. The origin of the mechanical loss is the phase delay of the relaxation of thermal distributions. At an adiabatic limit (mentioned in Chapter 3), its spectrum density is represented by [12],

$$\delta x_{\rm thermo} = \left[\frac{16}{\sqrt{\pi}}\alpha^2(1+\sigma)^2\frac{k_{\rm B}T^2}{\rho^2C^2}\frac{\kappa}{w_0^3}\frac{1}{\omega^2}\right]^{\frac{1}{2}} \ [\mathrm{m}/\sqrt{\mathrm{Hz}}]. \tag{2.31}$$

Here, α is the thermal linear expansion of the material, κ is the thermal conductivity, ρ is the density, and C is the heat capacity. The amplitude is determined by the thermal parameters of the substrate and the beam radius[8]. Fused silica, which is the most common material for mirrors, has relatively small α and κ, resulting in a small amplitude of thermoelastic noise compared to Brownian noise[9]. On the other hand, other kinds of material, for example, sapphire, can have comparable thermoelastic and Brownian noise. Fortunately, the amplitude of thermoelastic noise decreases faster than Brownian noise, by making the beam radius w_0 larger.

Suspension thermal noise

The mirror for the test mass is suspended as a pendulum in the interferometer. The pendulum is also buffeted by the fluctuating thermal forces. If we simply relied on a modal expansion (also mentioned in Chapter 3), and assumed the loss in the pendulum

[6] $k_{\rm B} = 1.382 \times 10^{-23}$[J/K].

[7] We define the w_0 as the distance from the center at which the power of the beam becomes $1/e^2$ compared to the value at the center. Some researchers use the other definition r_0, at which the power becomes $1/e$. These two are related by $\sqrt{2}r_0 = w_0$.

[8] and the Poisson ratio σ.

[9] At room temperature, and under a reasonable beam spot size for the GW detectors.

joint material has constant loss angle[10] of ϕ_p, the thermal motion would be expressed as,

$$\delta x_\mathrm{pend} = \sqrt{\frac{4k_\mathrm{B}T\omega_\mathrm{p}^2\phi_\mathrm{p}}{m}\frac{1}{\omega^5}}\ [\mathrm{m}/\sqrt{\mathrm{Hz}}], \tag{2.32}$$

at $\omega \gg \omega_\mathrm{p}$. Here, m is the mass of the mirror and ω_p is the pendulum resonant frequency. Surely, the amplitude of the pendulum thermal noise steeply degrades with increasing frequency ($1/f^{5/2}$), but this noise is an additional limiting factor of the detectors sensitivity, when the detector's observation band is expanded to include a lower frequency in the future.

Other type of thermal noise

Other thermal noises have been considered theoretically. For example, there is a noise called thermo-refractive noise, which is related to a change in refraction index of the optical coating on the mirror caused by a fluctuation of the temperature. The effect is estimated to be small in most cases [34]. Another type of "thermal" noise[11] called the Photon-thermal noise has been proposed. The noise is caused by absorbed power on the coating (substrate), which fluctuates statistically. It becomes a displacement noise through a thermal expansion of the substrates. The detailed analysis is shown in [12, 16, 35].

2.4.2 Optical readout noise

There are two unavoidable noises in all optical measurements: shot noise and radiation pressure noise. These two are called optical readout noise[12].

Shot noise

The shot noise originates in the photon counting statistics at the signal detection port of the interferometer. When the photocurrent of i_DC [A] flows in the photo detector, the output spectrum of the photocurrent becomes,

$$i_\mathrm{shot} = \sqrt{2ei_\mathrm{DC}}\ [\mathrm{A}/\sqrt{\mathrm{Hz}}], \tag{2.34}$$

[10] In reality, there are many things to be considered for the adequacy of the constant loss ϕ_p. Usually, it should be depend on frequency, dimension of the wire and the test mass, surface loss or thermoelastic loss of the wire, the loss at the clamping point, and so on.

[11] It is not related to the fluctuation-dissipation theorem.

[12] The optical readout noise gives the Standard Quantum Limit (SQL) given by

$$\sqrt{\frac{2h}{\pi m\omega^2}}\ [\mathrm{m}/\sqrt{\mathrm{Hz}}]. \tag{2.33}$$

The sensitivity of the interferometer cannot exceed the SQL.

because of the Poisson photon-statistics of the incoming light. Here, e is an electron charge[13]. Shot noise is proportional to the square root of the incoming light power, P_0. On the other hand, the signal of the interferometer is proportional to it. As a result, the signal to noise ratio is proportional to the square root of the light power on the photo diode. In the case of Fabry-Perot cavity, the equivalent mirror displacement of the shot noise is given by

$$\delta x_{\mathrm{shot}} \sim \frac{1}{4\mathcal{F}} \left[\frac{h\lambda c}{2P_0} \left[1 + (\omega\tau)^2\right] \right]^{\frac{1}{2}} \quad [\mathrm{m}/\sqrt{\mathrm{Hz}}], \tag{2.35}$$

$$\tau = \frac{2L\mathcal{F}}{c\pi} \quad [\mathrm{s}] \tag{2.36}$$

with some approximations[14]. Here, $\mathcal{F}$ is the finesse of the cavity, h is the Planck's constant, λ is the wavelength of the light, L is the cavity length, and τ is the storage time of the cavity. Above the frequency given by $1/(2\pi\tau)$, that is called cutoff frequency, the shot noise starts to increase. Usually the cutoff frequency is designed to be at $\sim$1 kHz, so as not to degrade the sensitivity in the observation band.

Radiation pressure noise

The mirror position is buffeted by the back-action of the reflected photons, whose number is fluctuated by photon statistics. This is called radiation pressure noise. In the case of Fabry-Perot cavity[15], the radiation pressure induced displacement noise is

$$\delta x_{\mathrm{radi}} = \frac{4\mathcal{F}}{\pi m \omega^2} \left[\frac{2hP_0}{\lambda c[1 + (\omega\tau)^2]} \right]^{\frac{1}{2}} \quad [\mathrm{m}/\sqrt{\mathrm{Hz}}]. \tag{2.37}$$

The radiation pressure noise is related to the uncertainty of the position of the mirror in a macroscopic scale. It is concentrated in the low frequency region, and it is proportional to the square root of the light power P_0. In current gravitational wave detectors, the shot noise is a significant problem, and the radiation pressure noise will be relevant only in low frequency dedicated interferometers. Therefore, the light power is increased as high as possible in all detectors in construction or operation.

2.4.3 Noises in the laser source

The laser is the most suitable light source for the interferometer because of its high coherence. However, in reality, even a laser has fluctuations in its frequency and in its intensity. They appear as displacement noises in the interferometer.

---

[13] $e = 1.602 \times 10^{-19}$[C].

[14] Unity conversion ratio of photo detector, critical coupling cavity, high reflectivity with low loss, and so on.

[15] With the same approximations footnoted in the previous subsection about shot noise.

Laser frequency noise

In a single Fabry-Perot cavity, the frequency noise of the laser light, $\delta\nu$ [Hz/$\sqrt{\text{Hz}}$], directly couples to the displacement noise by a simple relationship of

$$\delta x_{\text{freq}} = \frac{L}{\nu}\delta\nu \ [\text{m}/\sqrt{\text{Hz}}]. \tag{2.38}$$

Here, L is the length of the cavity, and ν is the frequency of the light. By making the cavity length shorter, the effect is made less important.

In the Fabry-Perot Michelson interferometer, the frequency noise is subtracted optically at the interference of the detection port, and appears as a signal through the asymmetry of the two arms. Electrical subtraction is also possible, if two equivalent Fabry-Perot cavities resonate against one identical laser simultaneously.

Laser intensity noise

The displacement noise in the cavity is obtained as an intensity change at the photodetector. Thus, the fluctuation in intensity of the laser source can couple with the read-out displacement noise. The effect is represented by[16]

$$\delta x_{\text{int}} = \frac{\delta P}{P}\delta x_{\text{RMS}} \ [\text{m}/\sqrt{\text{Hz}}], \tag{2.39}$$

where $\delta P/P$ [1/$\sqrt{\text{Hz}}$] is the relative intensity noise of the laser and δx_{RMS} [m] is the residual motion RMS (root mean square) fluctuation of the mirror around the Fabry-Perot resonance. By suppressing the residual motion fluctuation of the mirrors, the effect of the intensity noise is effectively reduced.

2.4.4 Non-fundamental noises

There are other noise sources, which are not inherent in the interferometer but inevitable for its operation. We describe seismic noise, electric circuit noise, and residual gas noise in the following.

Seismic noise

Seismic motion is one of the inevitable noises for every ground-based experiment. In the gravitational wave interferometers, the mirror is suspended as a pendulum to be a free mass in the observation band. The pendulum also acts as an isolation system for the seismic noise, but its isolation level alone is not sufficient to fulfill the requirements. Usually, in addition to the pendulum, many stages of isolation system

[16] We assume that the cavity is locked to its resonance by a modulation method.

are installed to further suppress the seismic noise. Generally speaking, the ground motion has a typical spectrum of

$$\delta x_{\mathrm{gnd}} \sim 10^{-7}\frac{1}{f^2}\ [\mathrm{m}/\sqrt{\mathrm{Hz}}], \tag{2.40}$$

where the factor 10^{-7} is the typical value for Tokyo area. The total isolation system, whose transfer function is given by $H_{\mathrm{iso}}(f)$, suppresses the motion to

$$\delta x_{\mathrm{seis}} = |H_{\mathrm{iso}}(f)|\delta x_{\mathrm{gnd}}\ [\mathrm{m}/\sqrt{\mathrm{Hz}}], \tag{2.41}$$

at the mirror level. Typically $|H_{\mathrm{iso}}(f)|$ is $1/f^4$ to $1/f^6$ in the current typical gravitational wave detector. The seismic noise limits the sensibility below ∼100 Hz. To make the observation band wider and to perform stable operation, low frequency vibration isolation systems are going to be installed in the near future.

Electric circuit nose

Because the mirror position is fluctuated by the seismic motion, especially at the resonances of its isolation system, the mirror of the Fabry-Perot cavity length has to be controlled and kept at its resonance for a sensitive measurement. The servo circuit and actuator circuit for the cavity length control can disturb the mirror position.

Usually, the servo circuit is designed to have a sufficient gain for stable operation and for suppression of the other noises, for example the intensity noise, without introducing additional noises. Too high gain also can introduce noise. Thus, the balance between the high gain and the low noise determines the servo-loop design.

Similarly, the actuator should have enough dynamic range (sufficiently strong coupling) to suppress the residual motion. If the coupling is determined, the actuator-induced noise is also practically determined, because the actuator circuit noise cannot be lower than a certain value, typically order of a few nV/$\sqrt{\mathrm{Hz}}$. Therefore, in order to make the actuator noise smaller than the goal sensitivity, the uncontrolled motion of the mirror has to be sufficiently damped, and as well the actuator circuit has to have low noise.

Residual gas noise

The gas molecules along the optical path affect the sensitivity of the interferometer through their refraction index fluctuation. The effect is estimated to be [36]

$$\delta x_{\mathrm{gas}} = \left[\sqrt{8\pi L}\frac{(n_0-1)^2}{(A_0/V_0)u_0\sqrt{\lambda}}\left(\frac{p}{p_0}\right)\left(\frac{T_0}{T}\right)^{\frac{3}{2}}\right]^{\frac{1}{2}}\ [\mathrm{m}/\sqrt{\mathrm{Hz}}], \tag{2.42}$$

where n_0 is the refractive index of the gas, V_0 is the volume of one mole gas[17] at the standard temperature (T_0), A_0 is the Avogadoro's number[18], u and u_0 is the mean velocity of the gas molecule at temperature T and at the standard state, respectively. The typical required vacuum level for a kilometer class detector is calculated as $\sim 10^{-6}$ Pa from this equation. In reality, most of the pipe length is at a level of $\sim 10^{-8}$ Pa making a good safety margin.

2.4.5 Example of the detector sensitivity

Figure 2.5 shows the typical sensitivity curve of a first-generation gravitational wave detector. The curve was drawn based on the noise above mentioned noise evaluation[19]. Up to several tens of hertz, the seismic noise dominates the sensitivity, and over 1 kHz the shot noise start to increase. The best sensitivity is usually obtained at several hundred hertz region, which is designed as the observation band. In the observation band, the mirror thermal noise limits the detection sensitivity. Because the target of the ground-based interferometer has a typical amplitude of $h \sim 10^{-20}$ [m/$\sqrt{\text{Hz}}$], or smaller, in that frequency range, the existence of the mirror thermal noise is a critical problem. Therefore, the reduction of the mirror thermal noise is a significant theme for the direct gravitational wave detection.

2.5 Summary of this section

In this section, we have reviewed the theory of gravitational waves, some astronomical sources, the principles of the interferometric detectors, and their noise sources. The existence of gravitational waves is a sure fact, but they have not been detected directly. To open a new window for astrophysics using gravitational waves, large-scale interferometric detectors are under construction or operation. Most of their observation band is thought to be limited by the mirror thermal noise, which originates in thermal fluctuations of the mirror surface. This noise has to be fully studied for the direct detection of the gravitational waves.

In the following chapter, we describe the theories for the mirror thermal noise and the experiments on it that have been done in this thesis and elsewhere.

---

[17] $V_0 = 2.24 \times 10^{-2}$ [m^3/mol].

[18] $A_0 = 6.02 \times 10^{23}$.

[19] We have shown equations true for single mirror or single Fabry-Perot cavities. Otherwise some modifications of coefficient are required. The displacement sensitivity x [m/$\sqrt{\text{Hz}}$] is converted to the strain sensitivity h [1/$\sqrt{\text{Hz}}$] by $h = x/L$. Here L is the arm cavity length.

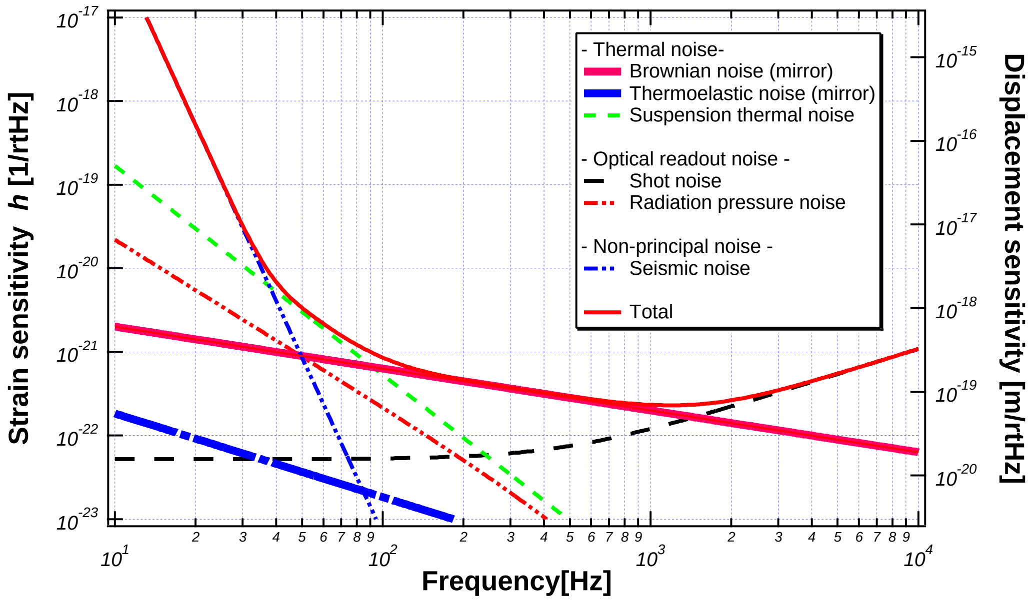

Figure 2.5: Typical sensitivity curve of a gravitational wave detector; We assumed a Fabry-Perot Michelson type interferometer similar to TAMA. Typical parameters are as follows. Arm length: L=300 [m], Laser power: P_0=10 [W], Power recycling gain: 10, Cavity finesse: $\mathcal{F}$=520, Mirror: fused silica (1 kg), Mirror loss: $\phi_{\rm sub} = 1/3 \times 10^6$, Coating loss: $\phi_{\rm coat} = 4 \times 10^{-4}$, Pendulum Q: 1×10^6, Isolation performance : $|H_{\rm iso}| = 1/f^5$. The Brownian thermal noise limits the bottom of the sensitivity curve. In this graph, the thermoelastic noise is negligible compared to the Brownian noise. This is because we considered a fused silica mirror, which has a small thermal expansion coefficient, as mirror substrates. In the case of other substrate materials, such as sapphire, the thermoelastic noise could overcome the Brownian noise.

Chapter 3

Mirror thermal noise

In this chapter, we discuss the calculation method of mirror thermal noise and past experiments.

Thermal noise is the microscopic fluctuations of a macroscopic system, which is in thermal equilibrium. The amplitude of the thermal noise is related to the mechanical loss in the system by the Fluctuation-Dissipation Theorem (FDT). In the case of the mirror in a gravitational wave detector, its thermal fluctuations are excited through the mechanical losses in the mirror. In this thesis, we treat two kinds of mirror thermal noises, which have been theoretically considered. Each one is associated with a specific dissipation mechanism.

- **Brownian noise**: noise associated with all forms of background dissipation that are homogeneously distributed impurities and dislocations within a material. The dissipation mechanism is not theoretically calculated, but it is usually treated as an intrinsic constant dissipation.

- **Thermoelastic noise**: noise associated with thermoelastic dissipation, which is caused by heat flow along the temperature gradients around the beam spot. The dissipation mechanism is theoretically calculated by the equation of motion and the thermal conductivity equation.

The total mirror thermal noise is treated as the summation of these two[1].

In the following, we first discuss the basis of the FDT, and the theoretical ways to calculate these two kinds of thermal noises. Then, we review the experiments that are performed for mirror thermal noise.

[1]Both of them are Brownian noise in usual sense. We follow the nomenclature by Braginsky et al. [12]. In reality, they should be called Brownian noise caused by background damping and Brownian noise caused by thermoelastic damping, respectively, or something like that.

3.1 Fluctuation-Dissipation Theorem (FDT)

The FDT, which was established by Callen et al.[7, 8, 9, 10], is the most important theorem in considering thermal fluctuations of mechanics. The FDT predicts the relationship between the spectrum of the thermal noise and the mechanical dissipation in the system. Usually, the thermal noise of the mechanics, including the mirror in the detector, is estimated using the theorem assuming a specific loss mechanism. In this section, we review the FDT, its different forms, and its validity.

3.1.1 Basic form of FDT

We consider a linear system in a heat bath with a finite temperature, T. The transfer function, from applied force $f(t)$ to displacement $x(t)$, of the system is defined as

$$H(\omega) \equiv \frac{X(\omega)}{F(\omega)}, \tag{3.1}$$

where $X(\omega)$ and $F(\omega)$ are the Fourier transforms of $x(t)$ and $f(t)$, respectively. ω is the angular frequency. The admittance $Y(\omega)$, the conductance $\sigma(\omega)$ and the resistance $R(\omega)$ of the system are defined as

$$Y(\omega) \equiv \frac{i\omega X(\omega)}{F(\omega)}, \tag{3.2}$$

$$\sigma(\omega) \equiv \mathrm{Re}[Y(\omega)], \tag{3.3}$$

and

$$R(\omega) \equiv \mathrm{Re}\left[\frac{1}{Y(\omega)}\right], \tag{3.4}$$

respectively. The power spectrum[2] of x at frequency f is given by,

$$G_x(f) = \frac{4k_\mathrm{B}T\sigma(\omega)}{\omega^2}, \tag{3.5}$$

where, k_B is the Bolzmann constant. This is called the first FDT. By using the transfer function, it is rewritten as

$$G_x(f) = -\frac{4k_\mathrm{B}T\mathrm{Im}[H(\omega)]}{\omega}. \tag{3.6}$$

Because the admittance $\sigma(\omega)$ or the imaginary part of the transfer function $H(\omega)$ represents the loss in the system, Eqs.(3.5) and (3.6) relate the fluctuation and the

[2] We adopt one-side power spectrum throughout this thesis.

dissipation (loss) in the system. From the viewpoint of the thermal noise estimation, Eq.(3.6) claims that if one wants to know the thermal noise of x (fluctuation of the observed point), what is needed is the knowledge of the transfer function obtained by applying a force f at the observed point[3].

Another standpoint of the thermal fluctuation is that the fluctuation is caused by the fluctuating force with a power spectrum of $G_f(f)$ applied on the system:

$$G_f(f) = 4k_\mathrm{B}TR(\omega). \tag{3.7}$$

This is called the second FDT. These two FDTs are equivalent.

3.1.2 Other forms of FDT

The basic forms of FDT can be applied for an ideal case. Usually, an observable physical quantity, $X(t)$, of the system is read out by a finite sized device. Using a weighting function $P(\mathbf{r})$, we write $X(t)$ as

$$X(t) = \int u(\mathbf{r}, t)P(\mathbf{r})dV, \tag{3.8}$$

where $u(\mathbf{r}, t)$ is the displacement of the system at the position $\mathbf{r}$.

Levin proposed a more useful form of FDT [13]:

$$G_X(f) = \frac{8k_\mathrm{B}T}{\omega^2}\frac{W_\mathrm{diss}(f)}{F_0^2}. \tag{3.9}$$

Here, $W_\mathrm{diss}(f)$ is an average dissipated energy when the oscillatory force

$$F_0 \cos(2\pi ft)P(\mathbf{r}) \tag{3.10}$$

is applied to the system. Since it is usually easier to calculate the dissipated energy than the transfer function, this formulation is widely used to calculate the mirror thermal noises; both the Brownian noise and the thermoelastic noise.

Nakagawa proposed another form of FDT using the Green's function [14]. In his formulation, the power spectrum of X is written by,

$$G_X(f) = \int P_i(\mathbf{r}_1)G_{u_iu_i}(\omega, \mathbf{r}_1, \mathbf{r}_2)P_i(\mathbf{r}_2)dV_1dV_2. \tag{3.11}$$

The $G_{u_iu_j}$ is the cross spectrum density between $u_i(\mathbf{r}_1)$ and $u_j(\mathbf{r}_2)$. It is related by the Green's function of the equation of motion of the elastic body, $\chi_{ij}(\omega, \mathbf{r}_1, \mathbf{r}_2)$:

$$G_{u_iu_j}(\omega, \mathbf{r}_1, \mathbf{r}_2) = -\frac{4k_\mathrm{B}T}{\omega}\mathrm{Im}[\chi_{ij}(\omega, \mathbf{r}_1, \mathbf{r}_2)], \tag{3.12}$$

$$\mathrm{Im}[\chi_{ij}(\omega, \mathbf{r}_1, \mathbf{r}_2)] = -\int \left[\frac{\partial \chi_{li}(\omega, \mathbf{r}, \mathbf{r}_1)}{\partial x_k}\right] c''_{klmn}(\omega, \mathbf{r}) \left[\frac{\partial \chi_{nj}(\omega, \mathbf{r}, \mathbf{r}_2)}{\partial x_m}\right]^* dV. \tag{3.13}$$

Here, c''_{klmn} is the imaginary part of the stiffness matrix.

[3]If the x is the generalized coordinate, f should be a generalized force which is conjugate to x.

3.1.3 Validity of FDT

The validity of the FDT has been demonstrated experimentally in simple systems. The most famous example is the voltage noise between the ends of a resistance [37], given by Eq.(3.7)[4]. The validity have been confirmed also in mechanics, by measuring the imaginary part of the transfer function and the corresponding thermal noise, [25, 27]. Even in a system, in which loss distribution is inhomogeneous within a system, the FDT gives an exact thermal noise [26]. For all of these reasons, the estimation of the thermal fluctuation in the interferometer mechanics usually relies on the FDT.

3.2 Brownian noise

In this section, we will discuss the presently used calculation (estimation) method of the Brownian noise of the mirror now proposed. Two approaches to calculate it have been tried.

- **Modal expansion**: The thermal noise is represented by the sum of normal modes using the FDT. This method is the traditional one to calculate the mirror Brownian noise and not always appropriate.
- **Direct approach**: The thermal noise is directly obtained from FDT. Only this method allows treatment of inhomogeneously distributed losses. This method was recently developed[5].

3.2.1 Modal expansion

Modal expansion is a traditional method to calculate thermal noise. We first discuss the general concept of this method and then discuss its application to the mirror.

Concept of the modal expansion

The basis of the method is the thermal noise of a one-dimensional oscillator. In a frequency domain, the equation of motion of a one-dimensional harmonic oscillator is written as

$$-m\omega^2 X(\omega) + m\omega_0^2 \left[1 + i\phi(\omega)\right] X(\omega) = F(\omega), \tag{3.14}$$

where m is the mass of the oscillator, and ω_0 is the angular resonant frequency of the oscillator. We introduced the mechanical loss as loss angle $\phi(\omega)$ here. $m\omega_0^2(1+i\phi(\omega))$ is called the complex spring constant. If $\phi(\omega)$ is constant versus frequency, it is called

[4] $R(\omega)$ corresponds to resistance R, and force f does to voltage V.

[5] This method is also effective to calculate the thermoelastic noise.

structural (damping). If $\phi(\omega)$ is proportional to the frequency, it is called viscous (damping). Usually, the background loss that is related to the Brownian noise is regarded as structural damping.

In this system, the transfer function is written as

$$H(\omega) = \frac{X(\omega)}{F(\omega)} = -\frac{1}{m}\frac{(\omega^2-\omega_0^2)+i\omega_0^2\phi(\omega)}{(\omega^2-\omega_0^2)^2+\omega_0^4\phi^2(\omega)}. \tag{3.15}$$

According to the FDT, Eq.(3.6), the thermal noise (fluctuation) of the mass is calculated as[6]

$$G_x(f) = \frac{4k_\mathrm{B}T}{m\omega}\frac{\omega_0^2\phi(\omega)}{(\omega^2-\omega_0^2)^2+\omega_0^4\phi^2(\omega)}. \tag{3.16}$$

Next, we consider a continuous elastic solid. Generally, the solution of the equation of motion in elastic solids is represented using an orthogonal basis of functions, $w_n(\mathbf{r})$, that represent the internal mode shapes. If the system is loss-less, the transfer function from the applied force to the displacement[7] has the form of

$$H(\omega) = -\sum_{n=1}^{\infty}\frac{1}{m_n}\frac{1}{\omega^2-\omega_n^2}, \tag{3.17}$$

where ω_n is the angular resonant frequency of the n-th internal mode. The m_n, called effective mass, is defined by

$$m_n = \frac{\int \rho w_n^2(\mathbf{r})dV}{(\int P(\mathbf{r})w_n(\mathbf{r})dV)^2} = \frac{2K_n}{\omega_n^2\bar{X}_n^2(t)}. \tag{3.18}$$

Here, $P(\mathbf{r})$ is the weighting function, K_n is the kinetic energy of the n-th internal mode, and $\bar{X}_n^2(t)$ is the RMS motion[8] of the n-th internal mode displacement $X_n(t)$.

By introducing the loss of each mode as $\phi_n(\omega)$ and by applying the FDT, the spectrum of thermal noise becomes

$$G_X(f) = \frac{4k_\mathrm{B}T}{\omega}\sum_{n=1}^{\infty}\frac{1}{m_n}\frac{\omega_n^2\phi_n(\omega)}{(\omega^2-\omega_n^2)^2+\omega_n^4\phi_n^2(\omega)}. \tag{3.19}$$

Therefore, the thermal noise of the continuous system is regarded as the sum of the thermal noise from each internal mode, which is idealized as a one-dimensional oscillator with its effective mass m_n. By assuming structural loss, $\phi_n(\omega) = \phi_n$, and

$$\omega \ll \omega_n, \tag{3.20}$$

Eq.(3.19) becomes,

$$G_X(f) \sim \frac{4k_\mathrm{B}T}{\omega}\sum_{n=1}^{\infty}\frac{\phi_n}{m_n\omega_n^2}. \tag{3.21}$$

[6] The suspension thermal noise, Eq.(2.32), is calculated from this equation, because it is regarded as a single-mode oscillator.

[7] These are defined by Eqs.(3.8) and (3.10).

[8] Time averaged $X_n^2(t) = (\int P(\mathbf{r})w_n(\mathbf{r})dV)^2$.

Application to the mirror

For the calculation of the mirror Brownian noise using this method, what should be calculated is effective mass m_n for each modal shape according to Eq.(3.18). In the interferometer, the mirror is illuminated by the TEM_{00} mode of Gaussian beam, which reads the weighted displacement of the mirror surface. Therefore, the beam weight function $P(\mathbf{r})$ has the form of

$$P(\mathbf{r}) = P(r, \theta) = \frac{2}{\pi w_0^2} \exp\left(-\frac{2r^2}{w_0^2}\right) \tag{3.22}$$

in cylindrical coordinates. The value w_0 is the beam radius. Another factor which should be calculated is each modal shape $w_n(\mathbf{r})$. If the mirror is cylindrical, a semi-analytical method, which was established by Hutchinson and McMahon [38, 39], is available. More generally, a numerical method, such as a finite element method, can be used for that purpose.

Using this modal expansion method, Gillespie [40] and Bondu [41] reported their results on mirror Brownian thermal noise in LIGO and VIRGO, respectively. In the detectors, the mechanical resonance of the mirror is of the order of 10 kHz. The mirror thermal noise limits the detectors sensitivity at several 100 Hz. Therefore, the approximation Eq.(3.20) is well satisfied. Also, conventionally, the measured quality factor at the n-th resonance Q_n is substituted into Eq.(3.21) as $\phi_n = 1/Q_n$.

Problems of modal expansion

Recently, a problem of the modal expansion method was clarified [42]. The mechanical loss is introduced *after* the system is divided into basis functions. The transfer function obtained without losses is not equivalent to the solution that is directly obtained from the equation of motion with the loss. The modal expansion fails, especially when the loss is inhomogeneously distributed in the system, $\phi(\mathbf{r}, \omega)$, because of a coupling between the internal modes. The mirror corresponds to this case, because it is made of several parts: mirror substrate, coating, magnet, and so on each with its own loss mechanism. Also, the summation of Eq.(3.21) has numerical difficulties. One has to sum up many normal modes until the solution converges to a specific value.

3.2.2 Direct approach

The other way to calculate thermal noise is to use the FDT directly. This approach is called direct approach. Several researchers calculated the mirror thermal noise without depending on the traditional modal expansion method. In the following, we review the Levin's approach, Nakagawa's approach and our approach named numerical dynamic approach.

Levin's approach

Levin theoretically calculated the Brownian thermal noise by using Eq.(3.9). In his paper [13], an infinite-half space is pressed by a cyclic force which has the weight function of Eq.(3.22). To treat the homogeneously distributed damping, a complex Young's modulus is assumed

$$E = E_0[1 + i\phi_{\mathrm{sub}}(f)]. \tag{3.23}$$

Here, $\phi_{\mathrm{sub}}(f)$ is the loss angle of the mirror substrate. The W_{diss} in Eq.(3.9) is expressed as

$$W_{\mathrm{diss}} = 2\pi f U_{\mathrm{max}} \phi_{\mathrm{sub}}(f), \tag{3.24}$$

where U_{max} is the energy of the elastic deformation integrated on the entire volume at a moment when the mirror (infinite-half space) is maximally contracted or extended under the action of the oscillatory pressure. To ease the calculation, he assumed a static force, since our interest is far below the mechanical internal modes, Eq.(3.20). Then the calculation of U_{max} is done only by the static theory of elasticity. The result was[9]

$$U_{\mathrm{max}} = \frac{1-\sigma^2}{2\sqrt{\pi} E_0 w_0} F_0^2. \tag{3.25}$$

Therefore, by assuming a constant $\phi_{\mathrm{sub}}(f) = \phi_{\mathrm{sub}}$, the thermal noise becomes

$$G_X(f) = \frac{4k_{\mathrm{B}}T}{\omega} \frac{1-\sigma^2}{\sqrt{\pi} E_0 w_0} \phi_{\mathrm{sub}}. \tag{3.26}$$

He confirmed that this result coincided with the results obtained by the modal expansion method [40] in this homogeneous and structural loss case. He also mentioned that, if the $\phi(f)$ is allowed to be inhomogeneous, $\phi(\mathbf{r}, f)$, the answer is different, and he qualitatively discussed the effects of the losses in the coating on the mirror.

For the homogeneous case, an identical result was reported also by Braginsky [12], calculating the transfer function (susceptibility) of the system and using the FDT in Eq.(3.6) form. Bondu [43] and Liu [15] solved the same Levin's problem in a cylindrical finite-sized mass. All of them are static and analytical analyses.

Nakagawa's approach

Nakagawa solved the same Levin's problem[10] in his formalism [44]. According to his expression, Eqs.(3.11) to (3.12), the power spectrum density of the mirror is represented by

$$G_X(f) = \frac{8k_{\mathrm{B}}T}{\pi^2} \frac{1}{\omega} \frac{1}{w_0^4} \int dS' \int dS'' e^{-\frac{2|\vec{r'}|^2}{w_0^2}} e^{-\frac{2|\vec{r''}|^2}{w_0^2}} \mathrm{Im}[\chi_{zz}^{\omega}(\vec{r'}, \vec{r''})]. \tag{3.27}$$

[9]Bound et al. corrected the factor error of the results by Levin [43]. We show the corrected result.

[10]Static, infinite-half space ($z < 0$).

Here, S' and S'' are the surface, $\vec{r'}$ and $\vec{r''}$ are the surface points. $\chi^{\omega}_{zz}(\vec{r'}, \vec{r''})$ is the elastic Green's function at the angular frequency ω. He proved that the imaginary part is proportional to the loss function and the static Green's function, $\chi^{st}_{zz}(\vec{r'}, \vec{r''})$, which is obtained by the static elastic theory, if the loss $\phi_{\rm sub}$ is constant and uniform:

$$\mathrm{Im}[\chi^{\omega}_{zz}(\vec{r'}, \vec{r''})] = \phi_{\rm sub}\chi^{st}_{zz}(\vec{r'}, \vec{r''}) = \phi_{\rm sub}\frac{1-\sigma^2}{\pi E}\frac{1}{|\vec{r'} - \vec{r''}|}. \tag{3.28}$$

By substituting this into Eq.(3.27), and performing an integral over the surface, he obtained a result identical to Eq.(3.26). Nakagawa also applied his method to calculate the effect of coating (depth d) on the mirror surface. By taking a linear superposition of the thermal noises from the coating and the bulk, which are calculated in a similar manner with Eq.(3.27), he obtained

$$G_X(f) = \frac{4k_{\rm B}T}{\omega}\frac{1-\sigma^2}{\sqrt{\pi}E_0 w_0}\phi_{\rm sub}\left(1 + \frac{2}{\sqrt{\pi}}\frac{1-2\sigma}{1-\sigma}\frac{\phi_{\rm coat}}{\phi_{\rm sub}}\frac{d}{w_0}\right). \tag{3.29}$$

Here, $\phi_{\rm coat}$ is the loss angle of the coating. He also showed that this result was also obtained by the Levin's approach, in which the dissipation energy is calculated.

Numerical dynamic approach

The calculations using the direct approach mentioned above were limited to the static approximation. Surely, the assumption might be effective to evaluate the thermal noise at frequency band that is lower than the resonances, but the assumption breaks down around the resonances of the mirror. All previous techniques required complicated theoretical calculations, not easily feasible for actual boundary conditions. Also, the solution for finite sized mass has a complicated form, which still has numerical difficulties.

These difficulties arose from *analytical* calculations. To overcome the difficulties, we solve the equation of motion *numerically*, using the finite element method and then we apply the FDT, Eq.(3.6) or (3.9). In this way, we can in principle treat all of the three-dimensional mechanics, loss distribution, and weighting function of displacements, in the entire frequency range. We have checked that our numerical results are consistent with the other analytical direct approaches away from resonances. In Appendix A, we give examples of this method.

3.3 Thermoelastic noise

In this section, we discuss the concept of the thermoelastic noise: thermoelastic damping and thermoelastic noise in the mirror. The thermoelastic noise is associated with thermoelastic dissipation, which is caused by heat flow along the temperature gradients.

3.3.1 Thermoelastic damping

Thermoelastic noise is interpreted as fluctuations due to thermoelastic damping. The mechanism of the damping in solids was found in 1930s by Zener [45]. When a non-uniform temperature distribution is applied onto an elastic body, it is deformed through its finite thermal expansion coefficient. On the other hand, when the deformation of the volume is applied by an external force, a non-uniform temperature distribution arises. The temperature distribution relaxes through thermal conductivity, accompanying a reactive deformation of the elastic body. The relaxation is done within a finite time determined by the thermal capacitance and the thermal conductivity of the material. If the applied force is cyclic, the phase of the deformation by the temperature gradient presents a delay against the phase of the applying deformation. The phase delay causes mechanical loss – this is called thermoelastic damping. The amount of the phase delay depends on the cyclic frequency and the relaxation time. Therefore, the thermoelastic damping has a frequency dependence.

In a simple single-mode oscillator, the thermoelastic loss is written as

$$\phi(\omega) = \Delta \frac{\omega\tau_0}{1 + (\omega\tau_0)^2}, \tag{3.30}$$

where $\phi(\omega)$ is the loss angle, Δ is the relaxation strength, and τ_0 is the relaxation time. Δ is expressed as a function of the temperature, T, the Young's modulus, E, and other thermal properties of the material:

$$\Delta = \frac{E\alpha^2 T}{\rho C}. \tag{3.31}$$

Here, α is the thermal linear expansion, ρ is the density, and C is the specific heat per unit mass. The relaxation time τ_0 is determined by the thermal diffusivity, D, and the scale of the thermal relaxation. If we consider the heat flow between two sides of a plate, whose thickness is d, the relaxation time τ_0 is given by

$$\tau_0 = \frac{d^2}{\pi^2 D}. \tag{3.32}$$

The thermal diffusivity D is related to the thermal conductivity, κ by $D = \kappa/\rho C$.

This damping mechanism was well studied experimentally in simple systems, such as bars, and ribbons by exciting a specific mode and measuring the quality factor of the mode. The theory agrees well with the experiment [46, 47].

3.3.2 Thermoelastic noise in the mirror

We now consider the thermal noise caused by thermoelastic damping in the mirror[11]. What should be solved is the elastic equation of motion and thermal conductivity

[11] Here, we consider just substrate thermoelastic noise for simpler arguments. Coating thermoelastic noise is evaluated to be small in our experiment, especially because of the small beam radius.

equation, while applying a force with a Gaussian beam profile.

The equation of motion is

$$\nabla(\nabla \cdot \mathbf{u}) + (1-2\sigma)\nabla^2 \mathbf{u} = -2\alpha(1+\sigma)\nabla\delta T. \tag{3.33}$$

Here, $\mathbf{u}(\mathbf{r}, t)$ is the displacement at the point $\mathbf{r}$, α is the thermal linear expansion, and δT is the temperature perturbation. The internal modes of the system are not taken into account, because this equation of motion is static. The δT evolves the thermal conductivity equation:

$$\frac{\partial \delta T}{\partial t} - D\nabla^2(\delta T) = -\frac{\alpha E T}{\rho C(1-2\sigma)} \frac{\partial(\nabla \cdot \mathbf{u})}{\partial t}. \tag{3.34}$$

Here, E is the Young's modulus. The first term, the second term, and the right part represent the temperature change, the thermal conduction, and the production of heat by deformation, respectively.

Adiabatic limit

Braginsky solved this coupled equation neglecting the second term and calculated the thermal noise using Eq.(3.6) in a infinite-half space [12]. A neglect of the thermal conduction term is called the adiabatic limit, which is true for higher frequencies. Liu solved the same problem more simply with the same assumptions but with Eq.(3.9) [15]. He calculated the dissipating energy, W_{diss}, using the relationship in thermodynamics [48]:

$$W_{\mathrm{diss}} = \left\langle T\frac{dS}{dt} \right\rangle = \left\langle \int \frac{\kappa}{T}(\nabla\delta T)^2 dV \right\rangle. \tag{3.35}$$

Here S is the entropy of the system. To solve perturbatively the equations at the first order of α, he first neglected the right part of Eq.(3.33), then solved it as a static stress-balance equation. The result, $\mathbf{u}$, was substituted into Eq.(3.34), and the resulting δT was put back Eq.(3.35). His calculation for the thermoelastic thermal noise was,

$$G_{\mathrm{adi}}(f) = \frac{16}{\sqrt{\pi}} \alpha^2 (1+\sigma)^2 \frac{k_{\mathrm{B}} T^2}{\rho^2 C^2} \frac{\kappa}{w_0^3} \frac{1}{\omega^2}. \tag{3.36}$$

Liu also solved the system within a finite cylindrical body applying different boundary conditions [15].

General form

Cerdonio solved the system in an infinite half space without neglecting the second term in Eq.(3.34), in other words, without using the adiabatic limit approximation

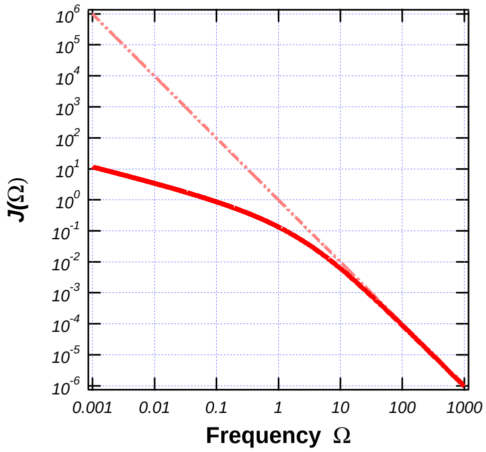

Figure 3.1: Frequency dependence of $J(\Omega)$; $J(\Omega)$ in Eq.(3.40) is plotted as a function of Ω. The dotted line represents $1/\Omega^2$, which corresponds to the adiabatic limit.

[16]. He solved the coupling equations essentially the same way as Liu. Obtained thermoelastic thermal noise was[12]

$$G_{\rm thermo}(f) = G_{\rm adi}(f)\Omega^2 J(\Omega), \tag{3.37}$$

$$\Omega \equiv \frac{\omega}{\omega_{\rm c}}, \tag{3.38}$$

$$\omega_{\rm c} = \frac{2\kappa}{\rho C w_0^2}, \tag{3.39}$$

$$J(\Omega) = \frac{\sqrt{2}}{\pi^{3/2}} \int_0^\infty du \int_{-\infty}^\infty dv \frac{u^3 e^{-u^2/2}}{(u^2+v^2)[(u^2+v^2)^2+\Omega^2]}. \tag{3.40}$$

Figure 3.1 shows the $J(\Omega)$ as a function of Ω. Because, $J(\Omega)$ becomes $1/\Omega^2$ at $\Omega \gg 1$, the thermoelastic noise coincides with the adiabatic limit, Eq.(3.36). The solutions involve temperature T, the elastic constants (E, σ, ρ), the thermal properties (α, C, κ), and the beam radius w_0. Therefore, if the material and the beam radius (and temperature) are determined, the thermoelastic noise can be exactly calculated.

Cutoff frequency

The $\omega_{\rm c}$, Eq.(3.39), is regarded as the cutoff frequency of the thermoelastic noise[13]. Above the cutoff frequency $\omega_{\rm c}$, the power spectrum density, G, of thermoelastic noise follows f^{-2}. Below the $\omega_{\rm c}$ it follows $\sim f^{-1/2}$. In usual cases, the cutoff frequency is

[12]The first proportional constant of $J(\Omega)$ in [16] is $\sqrt{2}/\pi^{1/2}$ instead of $\sqrt{2}/\pi^{3/2}$. We believe that our expression is correct.

[13]In reality, another cutoff frequency appears, when the frequency is sufficiently slow compared to the required time for the temperature gradients to relax within a scale of the mirror.

much lower than the observation band of the GW detectors. Assuming a sapphire at room temperature, the cutoff frequency becomes 40 mHz in f with a beam radius w_0 of 1 cm. At cryogenic temperature, or in an extremely small beam radius, the situation is different. For example, the cutoff frequency becomes 18 kHz (at 20K, in sapphire, with a beam radius of $w_0 = 1$ [cm]), and 40 kHz (at 300K, in sapphire, with a beam radius of $w_0 = 10$ [μm]).

3.4 Previous experimental researches

In this section, we review the experimental approaches that have been done for investigating the mirror thermal noises.

As we mentioned, the thermoelastic damping itself has for a long time been a well-known mechanism. However, the thermal noise caused by thermoelastic damping has not been measured as far as the authors know. The main focus of the experiments has been on Brownian noise[14]. The research can be divided into the following two items: 1) indirect investigation of thermal noise by measuring the intrinsic losses of the material and 2) direct measurement of thermal noise.

3.4.1 Measurement of intrinsic mechanical loss

According to the results of the direct approaches, the Brownian thermal noise in the observation band is determined mainly by the losses in the same frequency band and at around the beam spot, in other words, by the intrinsic loss of the substrate[15]. Many researches have tried to measure the intrinsic loss of the material, especially in extremely low loss material. Usually, the losses are evaluated by measuring the quality factor Q at the resonance. The Q is much easier to measure than the thermal noise of the sample, however, the measurement itself has a sticky problem.

The problem derives from the external loss that is introduced by a support system for the measurement. Many different quality factors have been measured for different modes by suspending the sample with wires [18, 19, 22]. In these measurements, the quality factor was limited by the loss introduced by the wire, resulting in inexplicable quality factors. Usually, the measured maximum quality factor was treated as the intrinsic loss of the material in the measurement. The situation is the same with other support systems, such as cantilever springs [20] and support systems used in resonant type GW detectors [49, 50, 51]. Measurements using small samples, especially wires,

[14] This is because the importance of the thermoelastic noise was realized recently (three years before this thesis).

[15] This fact was realized recently. For a long time, resultant quality factor at resonance in a pendulum has been considered important. The other factor, which determines the amplitude of the thermal noise at observation band, is the coating loss.

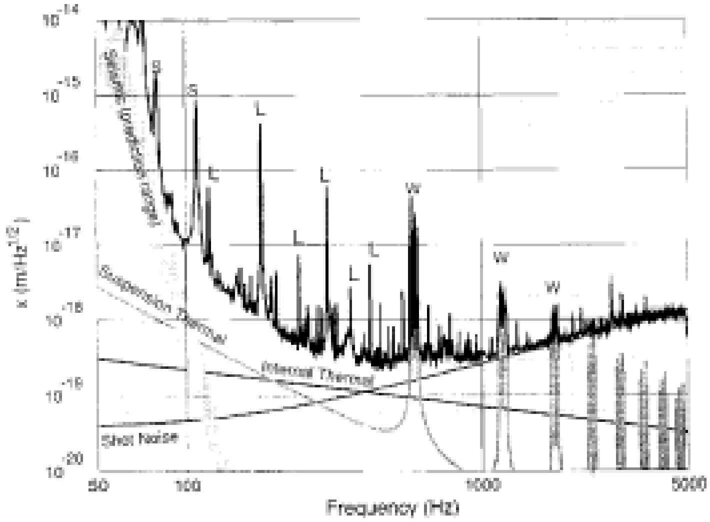

Figure 3.2: Sensitivity of the prototype interferometer developed for LIGO [61].

have also been tried [21, 52, 53, 54] . In this case also, the clamp for the support, the surface loss, or the thermoelastic damping limit the measured loss.

The most effective way to measure the intrinsic loss of the material was developed by the authors [23, 24, 55]. In the system, the samples are supported at the node of a subset of their vibration mode, using point contacts. This method enables us to measure the intrinsic material loss directly, excluding the loss due to the support system (Details are explained in Appendix B). We have measured the quality factors of low loss samples, fused silica, sapphire, silicon and so on. In many of the fused silica samples, we measured constant (or smoothly varying) quality factors as a function of frequency. This is a unique example that clearly showed the structural damping in the low loss bulk material, as far as the authors know.

3.4.2 Measurement of thermal noise

Another approach to investigate mirror thermal noise is to directly measure it.

There are running projects called TNI (Thermal Noise Interferometer) [56] and LFF (Low Frequency Facility) [57, 58][16] in the LIGO project and the VIRGO project, respectively. At this stage, they have not yet achieved wide-band high sensitivity to observe mirror thermal noise. At the California Institute of Technology, there was an interferometer called MarkII that achieved the world-highest displacement

[16]LFF mainly focuses on the suspension thermal noise. GEO is also performing an experiment that focuses on the suspension thermal noise [59]. Also, the researchers working for Glasgow 10-m prototype interferometer in GEO have reported that they observed silica thermal noise [60]. However, their analyses are weak arguments based on the measured quality factor at resonance.

sensitivity at 100 Hz region in 1990s [61]. The interferometer was not for the direct measurement of mirror thermal noise, but for the investigation of the interferometer itself. Although the bottom of the sensitivity between 250 Hz and 500 Hz, did not coincide with calculated internal thermal noise level (see Fig.3.2), some researchers have believed that this resulted from the mirror thermal noise, and some thought that it was thermal noise due to coatings. Because of the narrow bandwidth that could be analyzed, it is still disputable whether it was the mirror thermal noise or not.

The measurement of the thermal noise in simpler mechanics has been demonstrated. These experiments are regarded as the confirmation of the validity of the FDT (and direct approaches) as we mentioned in Section 3.1.3. However, their bandwidths were narrow, typically one octave at most. A wide-band and off-resonance thermal noise measurement has not yet been demonstrated even in the simple mechanics.

3.5 Summary of this section

We have reviewed the theoretical and experimental works on the mirror thermal noise.

Theoretically, the two kinds of mirror thermal noise, Brownian noise and thermoelastic noise, have been well researched. We also have developed a useful calculation method for Brownian noise, called numerical dynamic approach. For the indirect experimental research through the mechanical losses, we have already had established technique to directly measure the intrinsic loss. On the other hand, experimental work to directly measure the mirror thermal noise has not been achieved. Even in simple oscillators, only a few measurements, which concentrated on off-resonance thermal noise, have been reported.

We decided to perform an experiment to directly measure both kinds of mirror thermal noises over a wide frequency range, including on-resonance and off-resonance. This is, in our opinion, the most desirable and important experiment to be done. Only through the experiment we could conclude whether the existing theories, including FDT, were accurate or not, and, in a wider sense, whether the interferometer can really detect the gravitational wave or not.

In the following chapter, we will present our experiment to directly measure the mirror thermal noise.

Chapter 4

Experimental setup

In this chapter, we describe the experimental setup for the direct measurement of mirror thermal noise.

The objective of the experiment is to directly measure two kinds of mirror thermal noises in a realistic interferometer between wide frequency ranges. The two thermal noises are the Brownian noise and the thermoelastic noise. Figure 4.1 shows the displacement noises induced by the thermal noises that set our goal of sensitivity[1]. Typically, the displacement noise is 10^{-16} m/$\sqrt{\text{Hz}}$ at 100 Hz and 10^{-18} m/$\sqrt{\text{Hz}}$ at 100 kHz. Every component was specially designed to achieve the sensitivity to detect this level of displacement noise.

Figure 4.2 shows the conceptual design of the setup. The setup is made of two parts: test cavities and a frequency stabilized laser. The principle of the measurement is that a frequency-stabilized laser measures the thermal noise of test cavities. Two test cavities are locked to the same laser, producing two signals that are subtracted to make a differential signal. The differential signal, in which common mode noise is rejected, as well as the two signals from independent cavities, carries the information of the thermal noise.

Figure 4.3 shows the setup. We adopted the simplest design in every part of the setup to avoid useless complexities, keeping a safety margin without loosing the philosophy that the system should test the same conditions with what is occurring in realistic GW detectors.

Test cavity

The test cavity, which is the core of the experiment, is inside a vacuum tank (test cavity tank, see Fig.4.3). There are two equivalent Fabry-Perot cavities named "Test cavity A" and "Test cavity B". In order to measure both kinds of thermal noises,

[1]The parameters will be shown later.

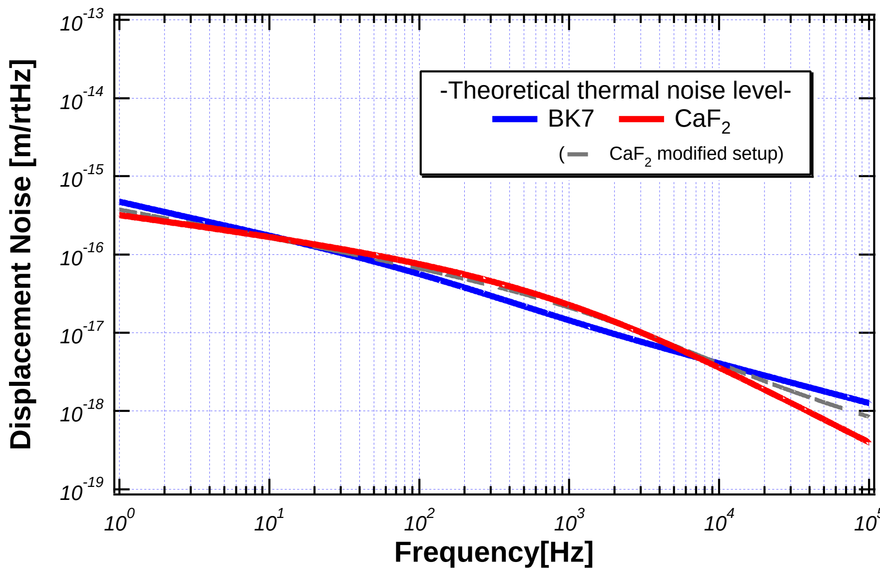

Figure 4.1: Mirror thermal noise levels; Thermal noise levels of our setup are shown assuming BK7 substrates for Brownian noise measurement or CaF_2 substrates for thermoelastic noise measurement. In reality, we combined CaF_2 mirror with BK7 mirror for the thermoelastic noise measurement (Details are explained in Chapter 5). In the setup, the thermal noise level is in between these two lines (thin line).

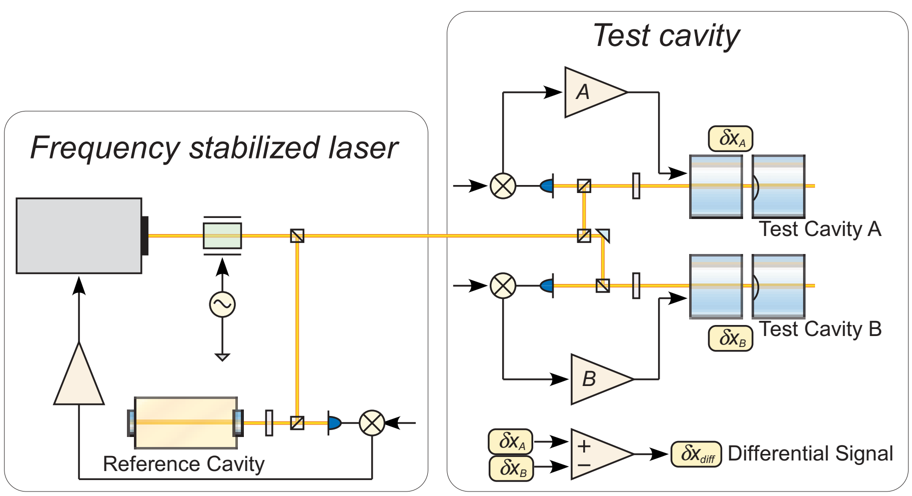

Figure 4.2: Conceptual design of the experimental setup; Two test cavities are locked to the same laser, whose frequency is stabilized by a reference rigid cavity. The thermal noise of the test cavities is measured. The two signals from the two test cavities are subtracted, producing a differential signal.

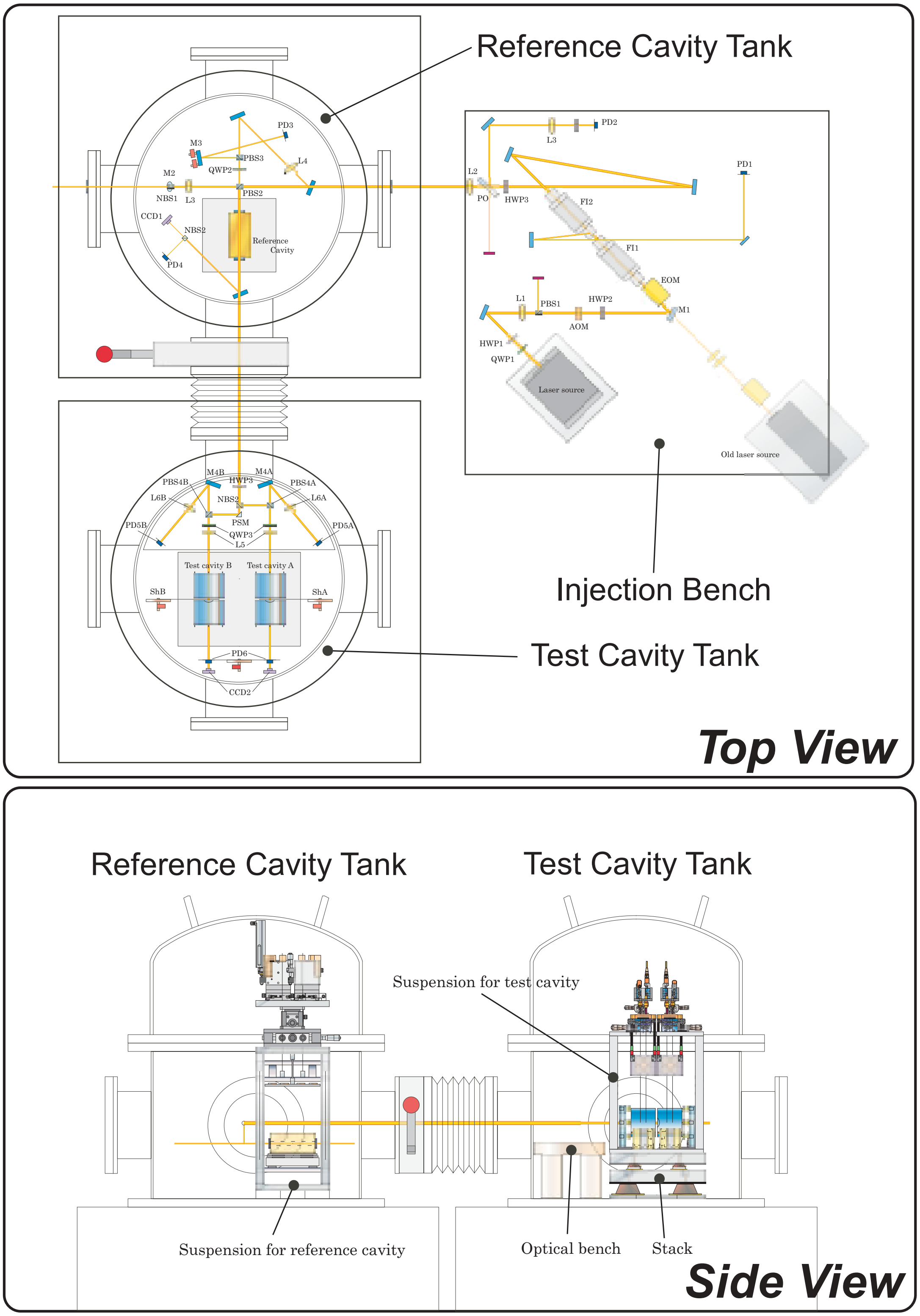

Figure 4.3: Experimental setup for the direct thermal noise measurement; the system is composed of three parts: 1) injection bench, 2) reference cavity tank, and 3) test cavity tank.

we chose carefully two kinds of substrates. To reduce the difficulty for the detection, the cavity was designed to have large thermal noises and to minimize other possible noises, such as the frequency noise. Also, in order to extend the observation band as low as possible, the test cavity was highly isolated from the seismic noise, using two stages of isolation system.

- **Test cavity mirrors.** The mirrors are monolithic like the main mirrors in GW detectors. We chose two kinds of substrate material to measure Brownian noise or thermoelastic noise: BK7 and Calcium Fluoride, respectively (Section 4.1.2). To enhance the displacement noise of these thermal noises, the path length of the cavity is designed to be short (1 cm). This also reduces the effect of frequency noise of the laser, which couples with the displacement noise proportionally to the path length (Section 4.1.3). Furthermore, the system was designed to be compatible with differential measurement using two equivalent cavities. The differential measurement is a very effective way to reject any noises, including the frequency noise, which commonly acts on the two cavities. Therefore, four mirrors were prepared for each substrate material. The shot noise, which is the principal noise in the measurement and not reduced by the differential measurement, has to be brought lower than the goal sensitivity by an appropriate choice of input power and finesse. In this experiment, the finesse was designed to be 500, which was enough to achieve our sensitivity and a realistic value for the current GW detectors (Section 4.1.4).

- **Vibration isolation system for the test cavity.** The test cavity mirrors are independently suspended as double pendulums for reduction of the seismic noise. The conceptual design of the pendulum is very similar to that of TAMA's. Each of the four mirrors is suspended from an intermediate mass with two loops of wires. The intermediate mass is also suspended from a control block. The special feature of ours is that the four control blocks are set on a common platform to provide a common mode rejection of the seismic noise. The suspension was carefully designed to extend the observation band to the lowest possible frequency (about 100 Hz). Its isolation ratio is estimated to be −100 dB at 100 Hz even without common mode rejection. This should be almost sufficient to observe the mirror thermal noises in Fig. 4.1. In order to guarantee an additional safety margin, we put the suspension on pre-isolation stack. The stack is also a double stage, providing −80 dB isolation ratio at 100 Hz (Section 4.1.5).

Frequency stabilized laser

A commercial laser was used as a light source of the test cavities. One of the most likely noise sources for the measurement is the frequency noise of the laser. Usually a commercial laser has a frequency noise of a few $\mathrm{Hz}/\sqrt{\mathrm{Hz}}$ at 1 kHz, which corresponds to a displacement noise of $\sim 10^{-16}\ \mathrm{m}/\sqrt{\mathrm{Hz}}$ in our setup. This value exceeds the required sensitivity in Fig.4.1. Thus, the frequency noise was stabilized to a negligible level compared to the design sensitivity. The stabilized laser is mainly composed of three parts: 1) the laser source on the injection bench, 2) the reference cavity in the reference cavity tank, and 3) the frequency-stabilization servo system.

- **Laser source.** The laser source is placed on an injection bench along with other optical components. A commercial LD-pumped Nd:YAG laser with a wavelength of 1064 nm is used as a laser source. Its output power is about 500 mW. A small fraction ($\sim 5\%$) of the output power is introduced into the reference cavity, and the remaining light is divided and sent to the two test cavities (Section 4.2.2).

- **Reference cavity.** A rigid Fabry-Perot cavity, with a spacer of low-expansion glass, is used for frequency stabilization. Its finesse is about 35000. The frequency of the laser is locked to the length of the reference cavity, and thus stabilized to a sufficient level to observe thermal noise of the test cavity mirrors. The reference cavity was also suspended as a double pendulum so as not to introduce seismic noise onto the frequency of the laser (Section 4.2.3).

- **Frequency-stabilization servo system.** The stabilization is done by feeding back an appropriate signal to the laser through a servo circuit. The required stabilization gain is about 10 across most of the frequency range. In this experiment, the stabilization system was designed to have much higher gain than required to make a sufficient safety margin. The signal is mainly fed back to the laser PZT tuning, and to the laser thermal tuning at low frequency for stable operation. The actual stability of the stabilized laser was estimated by the in-loop servo signal and by comparing with an external cavity (Section 4.2.4).

Detection system, control system and others

In addition to the main two components, the system is composed of the detection system, the control system, the other optics and so on.

- **Modulator.** The test cavities and the reference cavity are kept at their resonance by the Pound-Drever-Hall technique [62]. The output beam from the laser source is phase modulated by an EOM at 40 MHz on the injection bench (Section 4.3.1).

- **RF photo detector and demodulator.** The RF photo detectors detect the amplitude changes at the modulation frequency in the reflected light from the corresponding cavities. PD3 (in the reference cavity tank) is for reference cavity locking, and PD5-A and -B (in the test cavity tank) are for test cavity locking. The latter were designed to accept high-power incident beams. Their RF signal is demodulated at the modulation frequency by a Double Balanced Mixer (DBM), and then sent to the control servo system. The noise performance of the photo detector and of the demodulation system satisfies our demand to detect the thermal noise (Section 4.3.2).

- **Servo system for the test cavity.** Test cavity is kept at its resonance by the Pound-Drever-Hall technique. Demodulated signal by the DBM is sent to the test cavity servo circuit. The servo was designed to have high gain at low frequency and low noise. The unity gain frequency of the servo system is about 1 kHz. The control signal is sent to a coil driving circuit for the test cavity mirror. The efficiency of the coil is measured by a Michelson interferometer formed by two front mirrors. The displacement noise in each cavity is extracted from the error signal of the servo loop. To reject the common mode noise, such as the laser frequency noise, the two error signals are subtracted, producing a differential signal (Section 4.3.3).

- **Other optics for monitoring and measurement.** In order to accurately align those cavities to the incident beam, the transmitted lights were monitored by AF photo detectors (PD4, PD6). Mode-matching lenses (L1∼L5) were placed on appropriate positions to match the mode of the laser beam with those of each cavity (Section 4.3.4).

- **Vacuum system.** In order to avoid noise caused by air motion on the interferometer's sensitivity, the test cavities, the reference cavity and their related optics are housed in a vacuum system, made of two tanks: a test cavity tank and a reference cavity one. The system is evacuated with a rotary pump (Section 4.3.5).

4.1 Test cavity

In this section, we discuss the test cavity mirrors, whose thermal noise is measured, and the vibration isolation system for them. Figure 4.4 shows the schematic drawing of the mirrors for the test cavity. Table 4.1 summarizes the mirror specifications.

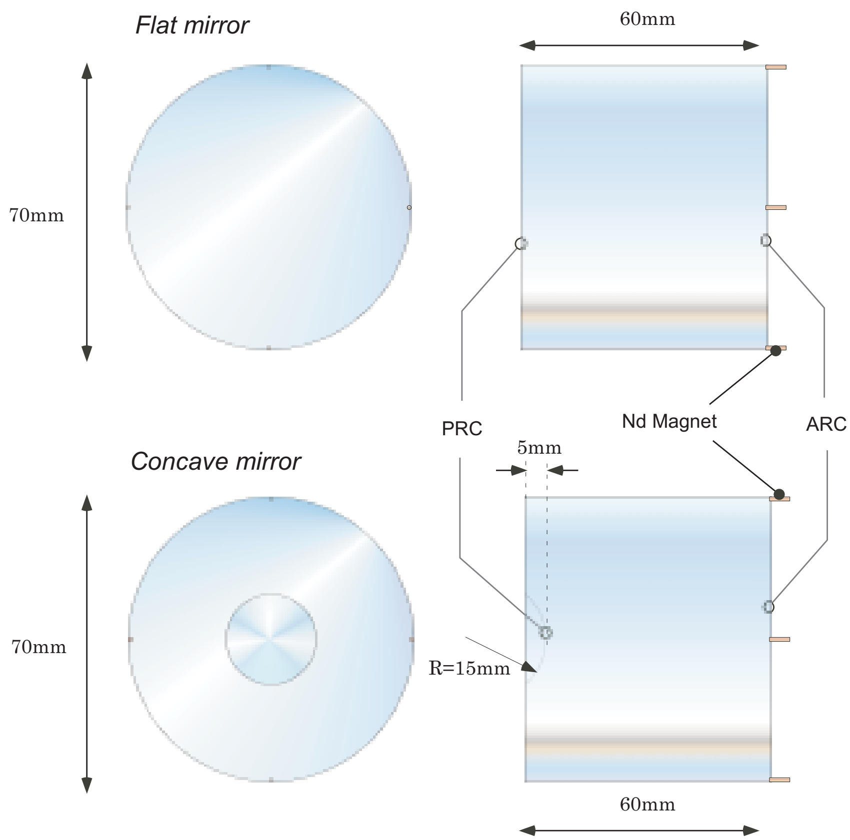

Figure 4.4: Mirrors for the test cavity; They are cylindrical mirrors, with diameter of 70 mm and height of 60 mm. The concave mirrors have a depression in their front surface forming a concave surface with a radius of 15 mm, and a depth of 5 mm. PRC: partial reflection coating, ARC: anti-reflection coating.

Table 4.1: Properties of the test cavity. *: Further discussed in Table 4.3.

Property	Value
Cavity length L	10 mm
FSR	15 GHz
Substrate	BK7/CaF_2
Dimension	70 mm(ϕ)$\times$60 mm(H)
Curvature R	∞(flat), 15 mm(concave)
Beam size on flat mirror	48.9 μm
Beam size on concave mirror	84.8 μm
Design finesse*	500
Seismic isolation system	double pendulum and stack

4.1.1 Requirement for the test cavity mirrors

Our choice was BK7 and Calcium Fluoride (CaF_2) as the substrates to imitate fused silica and sapphire, respectively. These are the most commonly selected substrates for GW detectors. We set the cavity parameters (g and finesse) virtually identical with TAMA's, except for our short cavity length (1 cm).

We chose the substrate materials and cavity parameters according to the following criteria: First of all, our target is the direct measurement on the Brownian and the thermoelastic noise. Then, at least two kinds of substrate material are required depending on which is the target. At the same time, the result should be able to be extrapolated to real GW detectors. Any special substrate for optics, special coatings, and special cavity parameters are avoided. Also, the experiment has to be done within a reasonable cost[2]. By making the cavity length shorter, the effect of the thermal noise can be enhanced and the other noises can be reduced. Of course, the other principal noise — shot noise — has to be lowered by adopting an appropriate finesse and laser power.

4.1.2 Substrate material

Table 4.2 summarizes the specifications of the thermal and mechanical properties of BK7 and CaF_2 as well as those of comparable materials (fused silica and sapphire, respectively). Their intrinsic mechanical losses were measured by the nodal support system (see Appendix B).

- **BK7**: This substrate material was chosen for Brownian noise measurement. BK7 is a well-known optical glass, which is widely used in the field of optics. The exact trade name of our substrates is S-BSL7 from OHARA Inc [63]. The mechanical loss is virtually constant versus frequency like most kinds of fused silica. Just their absolute values differ – the averaged intrinsic quality factor of BK7 is 3600. The main composition ($\sim$70%) of BK7 is fused silica (SiO_2), which is actually adopted for mirrors in every large-scale GW detector. Therefore, BK7 is thought to be sufficiently close to fused silica in our experiment. However, unfortunately, the thermal expansion coefficient is not so small – 13 times larger than that of fused silica. Therefore, the thermoelastic noise can significantly contribute to the overall thermal noise due to the small beam radius of our setup.

- **Calcium Fluoride (CaF_2)**: This substrate material was chosen for thermoelastic noise measurement. CaF_2 is a cubic crystal, which is also used in optics,

[2] Our mirrors cost about one tenth of the real mirror in a GW detectors.

Table 4.2: Mechanical and thermal properties of substrate materials. E: Young's modulus, σ: Poisson ratio, ρ: density, Q: mechanical quality factor, α: thermal expansion coefficient, κ: thermal conductivity, C: heat capacity. *: Frequency independent.

Property	BK7(S-BSL7)	Fused silica	CaF_2	Sapphire
E (Pa)	8.0×10^{10}	7.2×10^{10}	7.6×10^{10}	3.6×10^{11}
σ	0.21	0.17	0.28	0.29
ρ (kg/m^3)	2.52×10^3	2.20×10^3	3.18×10^3	3.98×10^3
Q	$3.6 \times 10^{3*}$	$10^5 \sim 10^7$	$\sim 3 \times 10^6$	$10^6 \sim 10^8$
α (1/K)	7.2×10^{-6}	5.5×10^{-7}	1.8×10^{-5}	5.0×10^{-6}
κ (J/m/s/K)	1.13	1.4	9.71	40
C (J/kg/K)	858	670	895	790

mainly as an apocromat, because of its low dispersion. CaF_2 itself is one of the candidate materials for the mirror substrates in future GW detector. It has a large thermal expansion coefficient – 33 times larger than that of fused silica – that enhances the thermoelastic noise. If it is compared to sapphire[3], the thermal expansion of CaF_2 is four times larger. As for thermal conductivity, the factor is one quarter – thus, both parameters, which mainly determine the thermoelastic noise properties, are of the same order of magnitude. Also, its intrinsic Q is relatively high ($\sim 3 \times 10^6$) such as for sapphire, resulting in smaller Brownian noise. Therefore, CaF_2 is appropriate to imitate the thermoelastic noise in a sapphire substrate. Our substrate is supposed to be from Oyou-Koken Co.Ltd [66]. Unfortunately, the crystal axis in the substrate is not certain.

4.1.3 Dimension and spot size

We designed the cavity to have short length with reasonable g parameters. The beam spot size, calculated by the length and the g parameter, and the properties of the substrate material give a prediction of the mirror thermal noise levels.

Dimension of the test cavity mirrors

The mirrors are monolithic cylinders, with height of 6 cm and diameter of 7 cm, that are about one half in volume of the real mirror in TAMA (Fig.4.4). Four mirrors were

[3]Sapphire is the candidate material for future gravitational wave detectors [64, 65].

prepared for each substrate material. Every surface, including the circumferential surfaces, was polished to a commercial grade.

Determination of cavity length

By designing the path length as short as possible, the frequency noise of the laser is depressed, and the thermal noise is enhanced. We set the cavity length as short as possible, 1 cm, from the viewpoint of an independent isolation system for all mirrors and for easy handling. As in TAMA, we adopted a flat-concave Fabry-Perot cavity with the cavity's g parameter of 1/3 to determine the mirror shape[4]. Therefore, two of the four mirrors are flat, and the other two are concave with a curvature of 15 mm, and a depth[5] of 5 mm. The flat and the concave mirrors face each other, forming two equivalent cavities for the differential measurement.

Beam spot size

The beam radii on the flat mirror and on the concave mirror as determined by the cavity parameters, are 48.9 μm and 84.8 μm, respectively. The beam spots are much smaller than the beam radius in GW detectors, enhancing the displacement noise caused by the mirror thermal noises. According to the theoretical formula, the Brownian noise of the flat mirror is 1.3 times larger than that of the concave mirror. In the case of thermoelastic noise, the factor[6] is 2.3.

Designed thermal noise level

Based on the choices of the substrates and of the beam spot sizes, the theoretical thermal noise levels are calculated for both of the test cavity substrates. They are the goal sensitivities of this experiment. The displacement noise caused by the two kinds of substrates are plotted on Fig.4.1.

Magnets

Four Nd magnets (1-mm diameter, 5-mm height, TAMA spec.) were glued on the mirror rear surface for control of the mirror position and for excitation of their internal modes (see also Section 4.1.5).

---

[4] This g ensures that the higher-order transverse modes rarely resonate simultaneously with the TEM_{00} mode.

[5] Therefore, the flat surface of the flat and the concave mirror face have a separation of 5 mm.

[6] At the adiabatic limit. Comparison of $\sqrt{G}$, not G.

4.1.4 Coating and finesse

Determination of finesse

The design finesse of the test cavity was determined to be 500, matching that of TAMA (520).

The choice of the finesse is important from the viewpoint of shot noise. According to Eq.(2.35), the shot noise is reduced by increasing the finesse and by increasing the laser power. According to the equation, a finesse of 500 was evaluated to be sufficient to achieve our goal sensitivity given our available laser power injected into the test cavity. Therefore, we did not need to adopt extremely high finesse. The relatively low finesse makes it easy to acquire lock of the cavity and ease handling.

Coating specifications

The front surfaces of all four substrates of each set of mirrors are coated with a partial reflection coating deposited in a single coating process to make identical cavities and to achieve critical coupling cavities. Anti-reflection coatings are deposited on their rear surfaces. Unfortunately, detailed specifications of the coatings, such as thickness and material or method of deposition were not disclosed to us. Also, the actual coating specifications were determined by the available coating that can be performed by the coating manufacturer, and the actual finesse was determined by the delivered reflectances.

Table 4.3 shows the specifications of the mirror reflectances. The BK7 substrate was coated by Showa Optronics [67]. The CaF_2 was coated by Sigma-Koki [68]. Unfortunately, because the coating on CaF_2 mirror was not to specs and had very small transmittance ($\sim 0.1\%$), it could not be used for the front (input) mirrors of the test cavities. The CaF_2 mirror was used only for the end mirror, coupling it with the BK7 mirrors as front mirrors of the test cavities (Details will be explained in Chapter 5).

Finesse measurement

The actual finesse was measured experimentally by shaking one of the mirrors of the cavity around its own internal resonance. The transmitted light was monitored during this test by PD6 in the test cavity tank, and then Finesse was calculated by the transmitted-light curve. The results are indicated on Table 4.3. The measured finesse was larger than the design value and different between two test cavities[7].

[7]We estimate at least 10% measurement error. The excess finesse introduced virtually no problem in performing the direct measurement, including the differential measurement between the two cavities.

Table 4.3: Reflectance and Finesse of the test cavity (mirrors). *: Measured coupling to a BK7 mirror used as front mirror.

Parameter	BK7 mirror	CaF_2 mirror
Mirror reflectance R (specification)	99.4±0.1%	>99.5%
Cavity transmittance (specification)	$> (1-R)/2$	NA
Calculated Finesse	520	>625
Measured Finesse (Cavity A, B)	630, 610	740, 810*

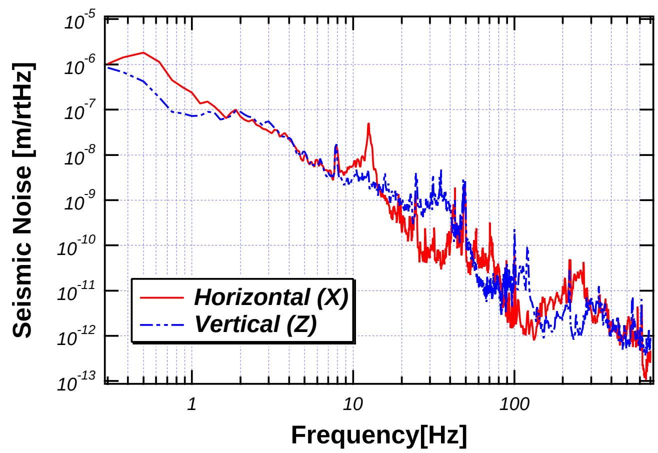

Figure 4.5: Measured seismic noise level on the test cavity tank; Horizontal and vertical motions are shown. The main trend of the seismic noise follows $\sim f^{-2}$. Several peaks, for example the 13 Hz and 43 Hz in the horizontal motion, were identified as resonances of the legs of the vacuum tank.

4.1.5 Vibration isolation system

Seismic noise is the most serious problem in the low frequency region. In this section, the vibration isolation system for the test cavity is described in detail. The isolation system is made of two parts: double pendulums and a stack.

Requirement for the isolation system

The measured seismic noise level on the test cavity tank is shown in Fig.4.5. While the goal sensitivity of this experiment is of the order of 10^{-16} m/$\sqrt{\text{Hz}}$ at 100 Hz, the seismic noise level is $\sim 10^{-11}$ m/$\sqrt{\text{Hz}}$ at this frequency. Therefore, an isolation performance of ~ -100 dB is required for the beam axis direction. The other degrees of freedom of the seismic motion leak into the direction of the beam axis through asymmetries of the isolation system. Therefore, a sufficient level of attenuations for all degrees of freedom has to be achieved as well. A double pendulum suspension and a stack were prepared to satisfy this requirement.

Conceptual design of the double pendulum

The four main mirrors are individually suspended as double pendulums. Figure 4.6 shows the suspension system designed for this experiment. Its conceptual design is similar to the suspensions used for the main optics in TAMA. Each of the four mirrors is independently suspended from an intermediate mass with two loops of tungsten wire. The intermediate mass is also suspended from a control block with four tungsten wires and vertical coil springs. The top plate, from which everything is suspended, is called the suspension platform. Common mode rejection of seismic noise is expected, by using a common platform for all four double pendulums. For damping purpose, the intermediate mass is located inside of a steel frame covered with strong magnets. The steel frame is hung from a control block positioned on the suspension platform. In order to avoid re-injection of seismic noise from the damping magnet, the frame is isolated from seismic motion by square-shaped blade springs (vertically), and by a stainless rod spring (horizontally).

Simulated and measured isolation performance of the double pendulum

The isolation performance was simulated using a semi three-dimensional analytic model. The parameters of the suspension were carefully determined by the simulation. As for coupling, the vertical motion was the limiting factor because it has the worst isolation ratio. The actual isolation performance was also measured experimentally by shaking the suspension with a vibration exciter. The simulated and measured isolation performance[8] is plotted on Fig.4.7. Above 50Hz, the measurement was limited by the sensor noise that obscures small vibration. We estimated that, according to the simulation with possible couplings, the translation isolation ratio is reaching $-100\,\mathrm{dB}$ at $100\,\mathrm{Hz}$, which satisfies our requirements.

Actuators

In order to align the mirrors to the incident beam, picomotors are attached on stages on the top of the control block. These motors can move the four mirrors independently in the required directions (pitch and yaw). The motors are controlled thorough a GPIB interface.

[8]We modified the suspension after the measurement to achieve higher isolation ratio. Peak frequency of the simulated result around 30 Hz does not agree with that of the measurement because the simulation was done using the new parameters.

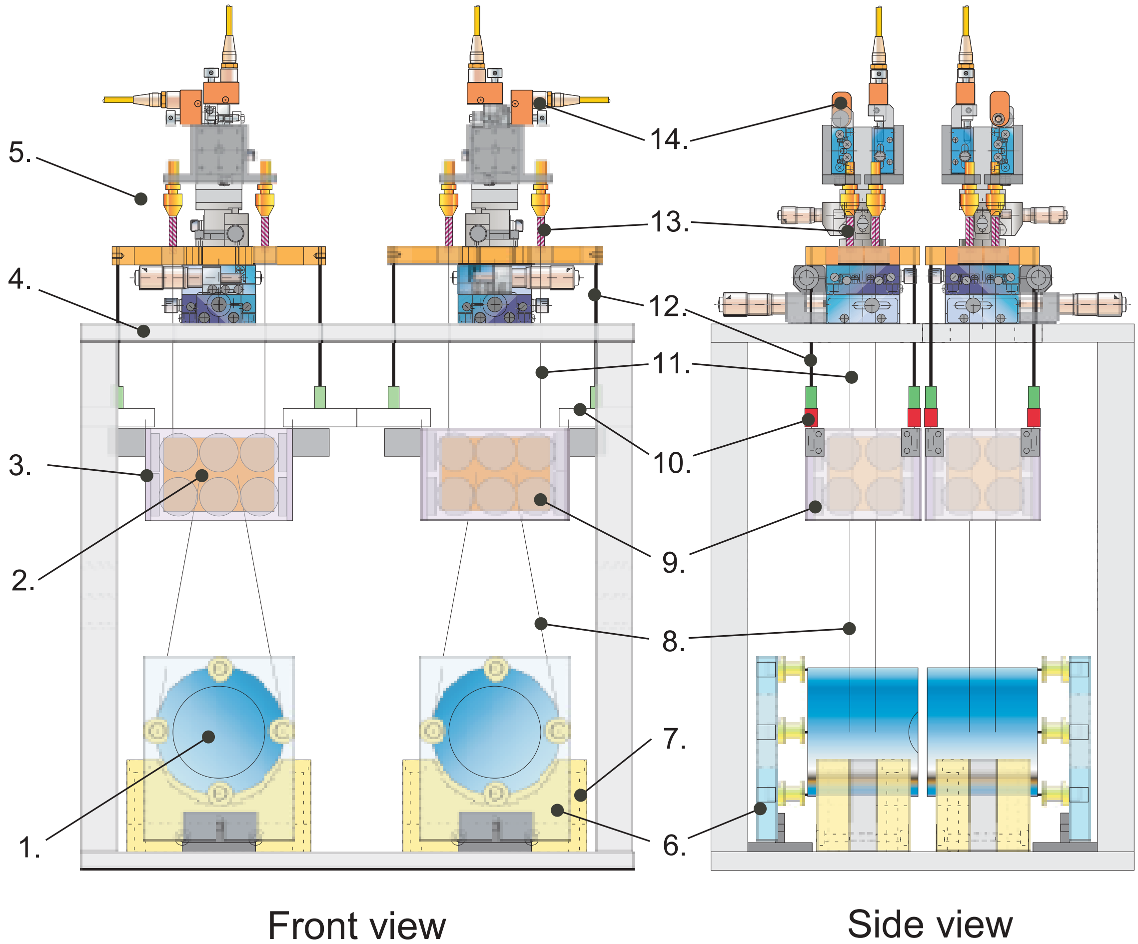

No.	Name	Material	Dimension or property
1.	Main mirror	BK7 or CaF_2	70 mm(D)×60 mm(H)
2.	Intermediate mass	copper	60 mm(L)×40 mm(W)×40 mm(H)
3.	Magnet support	magnetic stainless steel	80mm(L)×56 mm(W)×51 mm(H)
4.	Platform	aluminum	300 mm(L)×230 mm(W)×10 mm(H)
5.	Control block	(five stages)	
6.	Coil support	acrylic resin	100 mm(L)×82 mm(W)×10 mm(H)
7.	Safety (adjuster)	acrylic resin	
8.	Lower wire	tungsten	0.1 mm(ϕ)×136 mm(L)
9.	Magnet	Nd-Fe-B(N45)	21 mm(D)×4.6 mm(L)
10.	Blade spring	phosphor bronze	0.2 mm(t)×33 mm(L)×6 mm(W)
11.	Upper wire	tungsten	0.2 mm(ϕ)×120 mm(L)
12.	Rod spring	stainless steel	1.5 mm(ϕ)×80 mm(L)
13.	Vertical coil spring	steel	315 kg/sec^2
14.	Picomotor		Newfocus Model 8351

Figure 4.6: Suspension for test cavities.

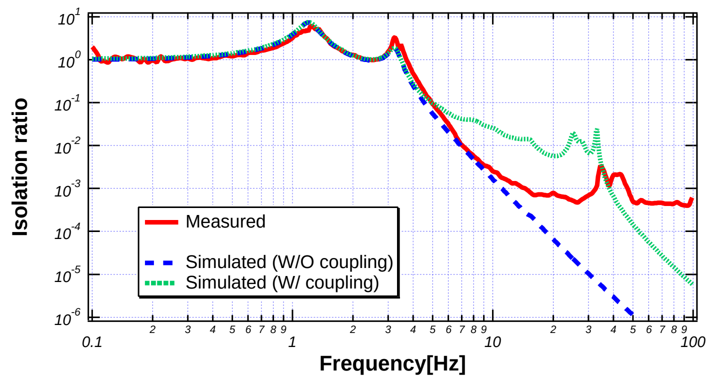

Figure 4.7: Measured and simulated isolation ratio of the suspension for test cavity (optical-axis direction).

Four coils are mounted close to the magnets at the back of each mirror. The four coil drivers of each mirror drive the coils commonly in the beam axis direction. They are made of copper wire with a diameter of 0.2 mm, coiled around a Macor bobbin. The number of turns is about 40, and the resulting resistance is about 5 Ω. For simplicity, DC offsets or active alignment controls are not installed. The coils on the two front mirrors are used for cavity length control and for excitation of internal modes. Those on the two end mirrors are used just for the excitation of internal modes.

Stack

A stack, which can provide further isolation for all degrees of freedoms, is installed beneath the suspensions support plate to provide a safety margin. The stack is composed of two stainless steel blocks, separated by isolation rubbers. Figure 4.8 shows the schematic view of the stack. The isolation performance of this stack was also measured by using the vibration exciter. It was better than −70 dB for vertical, and −80 dB for horizontal at 100 Hz. Figure 4.9 shows the result of the measurement.

Total isolation performance

The total performance of this suspension and stack system is estimated by multiplying the simulated isolation ratio of the suspension and the measured isolation ratio of the stack. Figure 4.10 shows the estimated seismic noise on the main mirror with these two components. Here, we assumed a coupling factor from vertical to horizontal motion of 1%. The calculated level of the seismic noise is of the order of 10^{-20} m/$\sqrt{\text{Hz}}$ at 100 Hz. The required level of displacement noise (10^{-16} m/$\sqrt{\text{Hz}}$ at 100 Hz) was very likely achieved because of the sufficient safety margin.

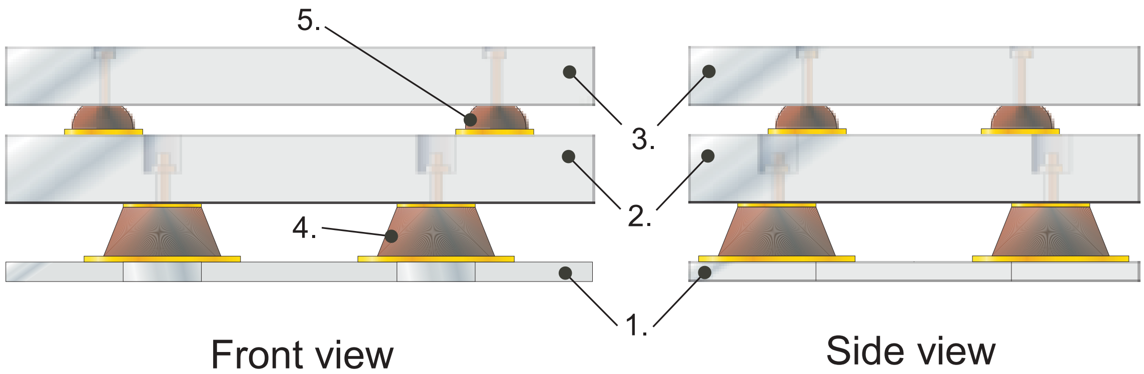

No.	Name	Material
1.	Bottom plate	aluminum
2.	Intermediate stage	stainless steel
3.	Top stage	stainless steel
4.	Bottom spring	rubber (45 kgf/cm)
5.	Top spring	rubber (32 kgf/cm)

Figure 4.8: Stack.

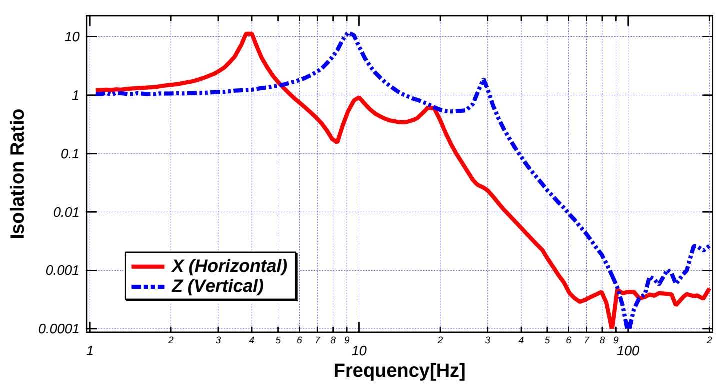

Figure 4.9: Measured isolation ratio of the stack; Over 100 Hz, the measurement is limited by the measurement system noise, which is mainly sound coupling directly onto the vibration sensor.

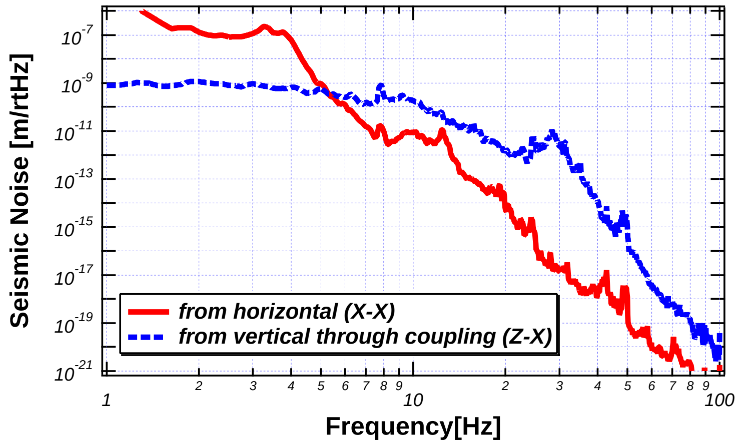

Figure 4.10: Estimated seismic noise level on the mirror; Horizontal ground motion to horizontal mirror motion (XX), and vertical ground motion to horizontal mirror motion (ZX) are shown, A coupling factor of 1% is assumed. The overall performance would be a convolution of these two lines.

4.2 Frequency stabilized laser

One of the main noise sources for the thermal noise measurement is the frequency noise of the laser. By making a test cavity shorter, and by performing a differential measurement between two cavities, the noise contribution becomes less important. However, it is still not negligible when only one of the two test cavities is under operation. Frequency stabilization is performed on a commercial laser slaving it to the reference rigid cavity.

In this section, the frequency stabilized laser, composed of the laser source, the reference cavity, and the stabilization servo system will be explained.

4.2.1 Requirement for the frequency stability

Figure 4.11 shows the free-run frequency noise of the laser that we used. Our goal sensitivities, converted into a frequency noise, are also shown. Our observation band is 100 Hz to 100 kHz. In that frequency region, the frequency noise is a few to ten times larger than the goal sensitivity. Therefore, stabilization gain must be larger than 10 over the frequency range.

In this experiment, the servo loop was designed to have sufficiently high gain to satisfy the requirements and run with as much gain as possible for reduction of noise for future upgrades. The requirements are relatively easy to achieve, especially at the lower frequency range of our observation band. However, at a higher frequency region, it is not sufficient – the remaining frequency noise is entrusted to the differential

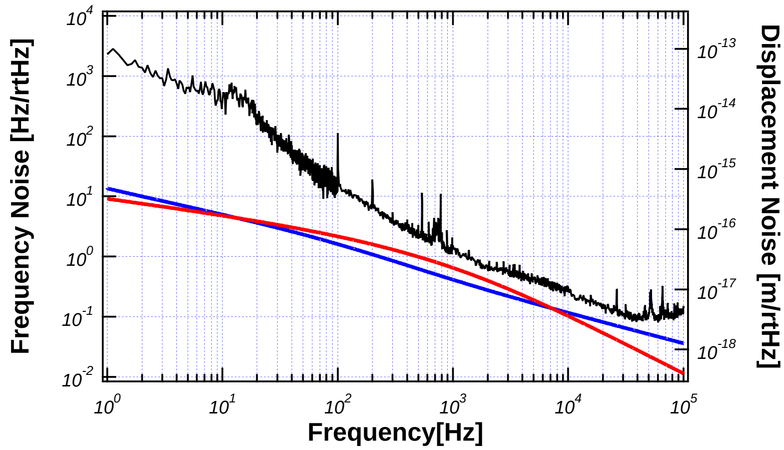

Figure 4.11: Frequency noise of the free-running laser; Our goal sensitivities are also shown. The left axis represents the frequency noise (unit: [Hz/$\sqrt{\text{Hz}}$]), and the right axis represents corresponding displacement noise in our setup (unit: [m/$\sqrt{\text{Hz}}$]).

measurement, which also makes a further safety margin at lower frequencies.

4.2.2 Laser source

Wavelength and power

As a laser source we used a LD-pumped Nd:YAG laser with a wavelength λ of 1064 nm (Innolihgt Mephisto 500NE). This was the most powerful available laser[9]. The wavelength is the most common choice in the current GW detectors. The crystal itself is used as ring cavity[10] in the laser head. This is believed to give the best performance as a continuous wave laser.

In order to sufficiently reduce the shot noise, the light power should be high enough. Therefore, we operated the laser at its maximum power (about 500 mW). Most of the light power has to be sent to the test cavities, to reduce the shot noise. At the same time, the required frequency stability is achieved by keeping a sufficient power to reduce shot noise in the reference cavity. We decided to use about 20 mW of the laser power for the frequency stabilization and the remaining for the test cavities ($\sim$ 220 mW for each) – this was the optimum for both of the cavities. The adjustment of the power distribution is done by rotating a half-wave plate (HWP3) and polarized

[9]Initially we had another laser source, which emits lower power ($\sim$30 mW), on the injection bench (Lightwave electronics, model 124-1064-050-F) for the first stage of the experiment. In order to reduce the shot noise, the laser source was switched to the higher power laser by a mirror with a beam flipper (M1) on the injection bench.

[10]It is called NPRO (Non-Planer Ring Oscillator), or MISER (Monolithic Isolated Single-mode End-pumped Ring).

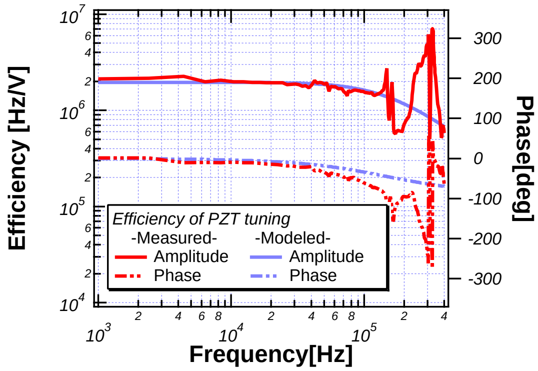

Figure 4.12: PZT tuning efficiency.

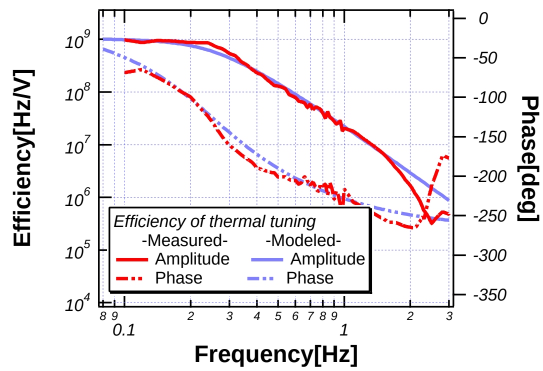

Figure 4.13: Thermal tuning efficiency.

beam splitter (PBS2).

Frequency tuning actuators

The laser frequency can be modulated by applying a voltage signal to its PZT length actuator and thermal controller. Our frequency stabilization was done by using these two actuators. The tuning efficiency was measured before its installation into the injection bench of our setup. Figure 4.12 shows the initially measured transfer function, from the applied voltage on the tuning PZT to the laser-frequency-change, as a function of the control signal frequency. The PZT has several resonances above 148 kHz, with the biggest one at about 320 kHz. They are the factor limiting the bandwidth of the stabilization loop. Within our observation band, the efficiency was measured to be 1.96 MHz/V. The thermal control efficiency was also measured (Fig.4.13). It had much larger tuning efficiency (~ 1 MHz/V), but slower response.

Intensity noise eater

The laser is equipped with an integrated intensity noise reduction system called "intensity noise eater". The intensity noise of the laser source is suppressed to some extent by switching on this servo system. Figure 4.14 shows the intensity noise spectrum of the laser measured at PD2 with the noise eater on and off[11]. In stable conditions, the intensity noise is suppressed by the noise eater to a negligible level compared to the goal sensitivity. If required, external intensity stabilization using AOM is also available.

[11] A fraction of the main beam is picked off by PO on the injection bench.

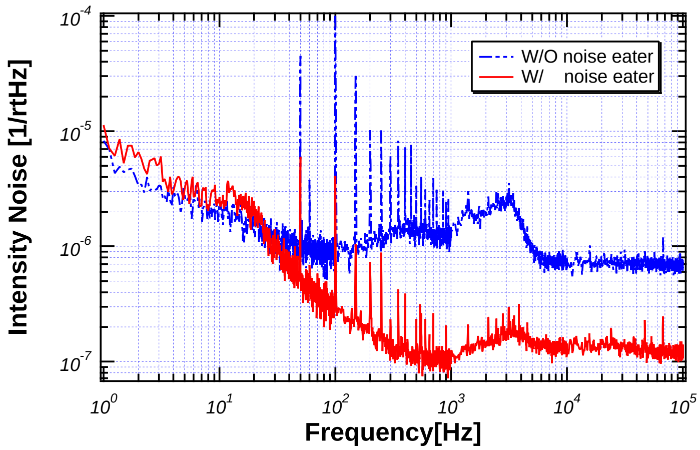

Figure 4.14: Intensity noise of the laser with and without the noise eater; These data were taken at PD2 for intensity monitoring.

Table 4.4: Properties of the reference cavity.

Property	Value
Cavity length	110 mm
FSR	1.36 GHz
Spacer	Clearceram Z
Mirror diameter	1 inch
Curvature (front, end)	∞, 500 mm
Reflectance (spec)	99.997%
Finesse (spec)	10^5
Finesse (measured)	35000

4.2.3 Reference cavity

In this section, we describe in detail the reference cavity. Reflectance, curvature, and the other parameters of the reference cavity are summarized in Table 4.4.

Spacer

Figure 4.15 shows the schematic view of the reference cavity. The material of the spacer of the mirrors is Clearceram Z from OHARA Inc. [69]. Its thermal expansion coefficient is $+0.8 \times 10^{-7}$/K at room temperature, according to the datasheet. The length of the spacer, in other words the length of the cavity, is 110 mm. A 10-mm diameter channel is machined through the central axis of the spacer for the optical path. There is smaller channel for airflow and for vacuum compatibility.

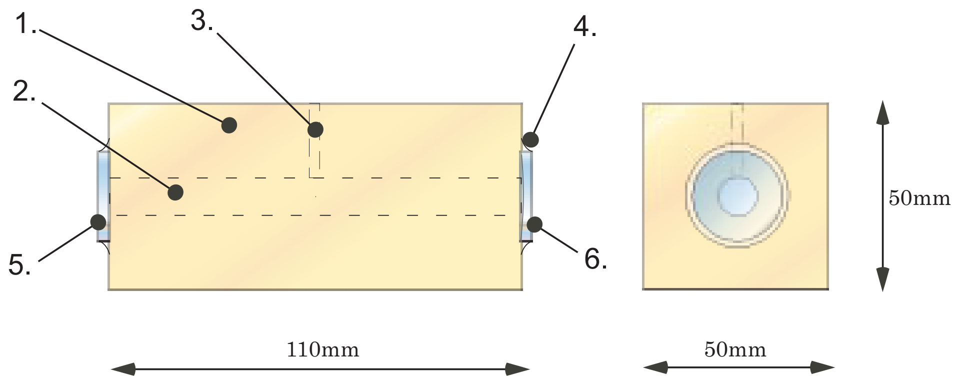

Figure 4.15: Reference cavity; 1: spacer (Clearceram Z), 2: hole for optical path, 3: hole for air flow, 4: adhesive, 5: flat (front) mirror, 6: concave (end) mirror.

Coating and finesse

The finesse of the reference cavity determines the shot noise limit of the frequency stability. It should be high as high as possible – we set the finesse at 10^5.

The fused-silica mirrors with a diameter of 1 inch were coated by REO with the same high reflectance (spec: 99.997%). The front mirror is flat. The end mirror has a curvature of 500 mm. They were glued onto the two ends of the spacer.

The finesse was measured experimentally by measuring the cavity transfer function within the stabilization loop[12]. Figure 4.16 shows the measured cavity transfer function. The cutoff frequency of the cavity was fitted to 19.3 kHz, which corresponds to the finesse of 35000. The measured finesse was lower than the design value – we believe that the mirror had been contaminated during the gluing procedure or during the installation.

Vibration isolation system for the reference cavity.

The reference cavity is also suspended as a double pendulum in a vacuum chamber in order not to couple seismic noise onto the frequency stability. Figure 4.17 shows the view of the suspension. This is essentially the same configuration as the suspension of the test cavity – a double pendulum with magnetic damping on its intermediate mass. The cavity is on an aluminum plate that is hung from an intermediate mass using four tungsten wires. Vertical isolation is provided by copper blade springs. The alignment to the incident beam is done by driving the electric motors attached on stages at the top of the suspension.

[12]The finesse was also measured by sweeping the frequency of the laser and monitoring its transmitted light by PD4. The result was consistent.

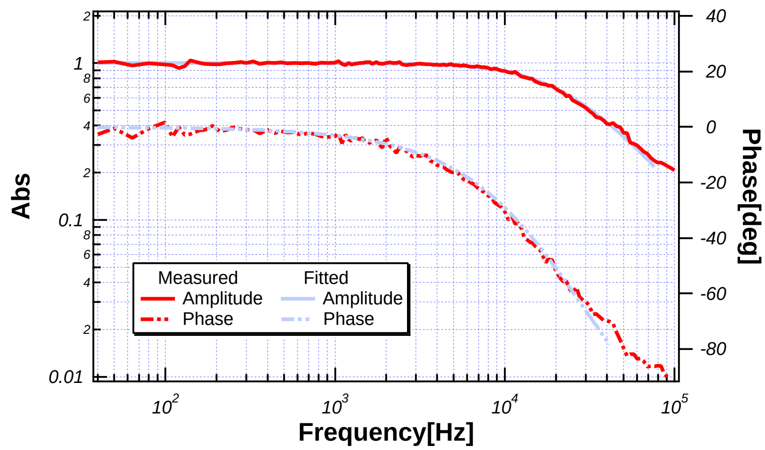

Figure 4.16: Reference-cavity transfer function.

4.2.4 Servo system

We designed the servo system to have sufficiently high gain to achieve the goal sensitivity.

The control signal is fed back to a PZT actuator (fast signal) and a thermal actuators (slow signal) of the laser head. Figure 4.18 shows the measured and design open-loop transfer function of the stabilization loop. The unity gain frequency was 76 kHz, and phase margin was 41 deg. The stabilization gain was over 80 dB at 100 Hz, which is much larger than the required gain (20 dB). Typical crossover frequency between PZT loop and thermal loop was 0.01 Hz. The total loop was stable at least an overnight without any adjustment after locking. This means that not only the servo, but also the suspension for the reference cavity, and the reference cavity itself are stable.

4.2.5 Achieved stability

The actual stability of the stabilized laser was estimated by the error signal of the stabilization loop and by an external cavity. According to the estimation, the stability satisfies our requirement below 30 kHz.

Stability evaluated by the error signal

The stabilized level was estimated from the error signal of the stabilization loop[13]. Figure 4.19 ("Estimated from error signal" in the legend) shows the estimated frequency noise of the error signal. In this evaluation, there is a possibility that the

[13]Free-run frequency noise is estimated from the feedback signal of the stabilization loop.

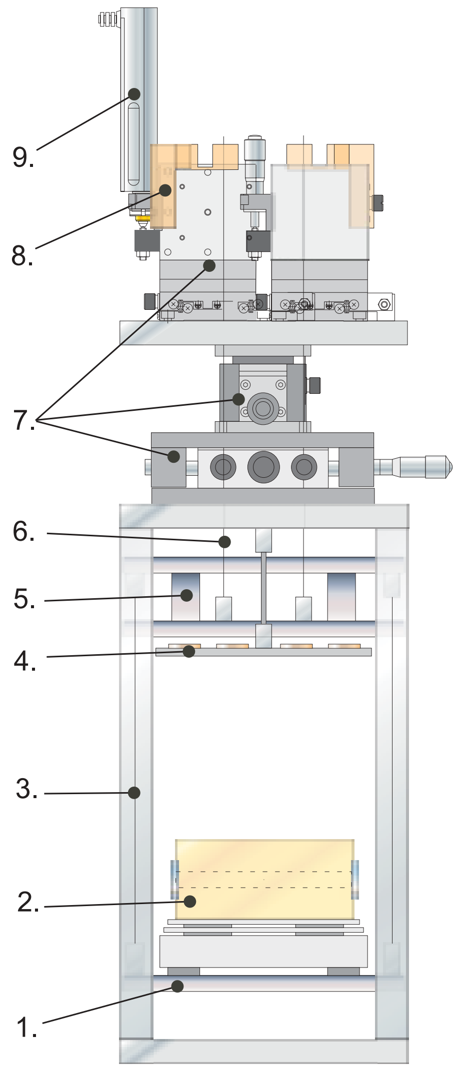

No.	Name	Material
1.	Bottom stage	aluminum
2.	Reference cavity	Clearceram Z
3.	Lower wire	tungsten
4.	Damping magnet support	magnetic stainless steel
5.	Bottom plate	aluminum
6.	Upper wire	tungsten
7.	Stages	
8.	Blade spring	copper
9.	Electric motors	

Figure 4.17: Suspension for the reference cavity.

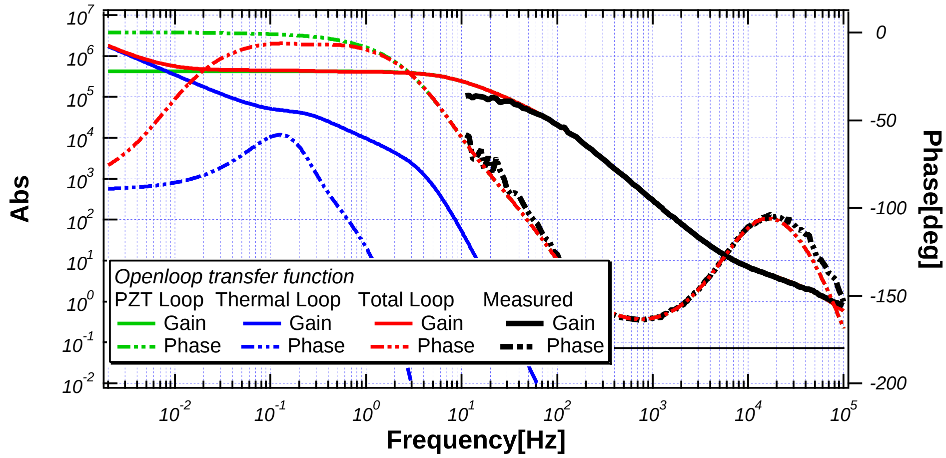

Figure 4.18: Open-loop transfer function of the reference cavity servo.

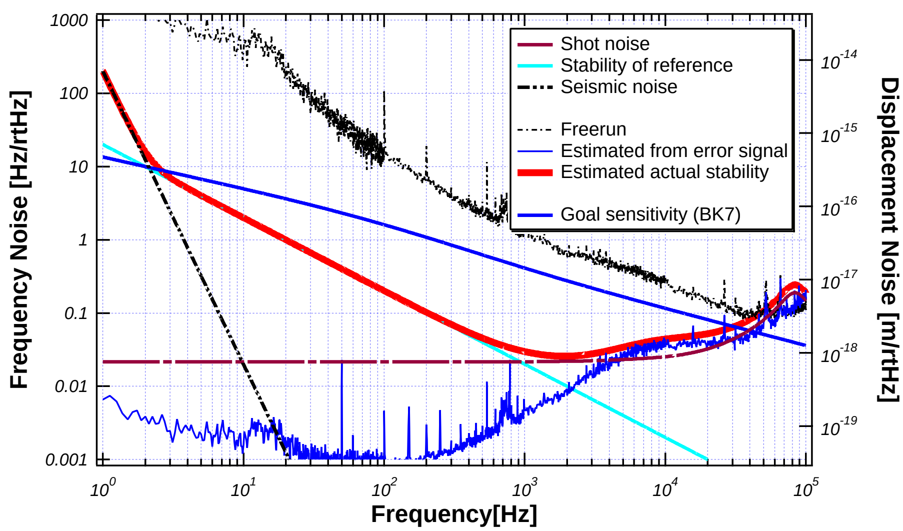

Figure 4.19: Estimated frequency noise of the stabilized laser; Thick line shows the estimated actual stability.

noise within the control loop limits the actual stability. In this stabilization system, the possible noise sources were the following two:

- **Shot noise.** Shot noise, produced in the photo detector and fed back to the tuning actuators through the feedback servo system, limits the frequency stability. According to the measurement of the DC photo current during the operation, the shot-noise-limited frequency stability is thought to be 2.16×10^{-2} Hz/$\sqrt{\text{Hz}}$ below the unity gain frequency and below the cavity pole frequency. Over those frequencies, the shot noise reaches (and exceeds at a certain frequency range) the free-running frequency noise. Detailed calculations show that the shot noise is a limiting factor of the stability between ∼1 kHz and ∼3 kHz and over ∼30 kHz.

- **Stability of the reference.** The actual stability cannot be better than the stability of the reference-cavity length, which is usually difficult to evaluate. The resultant frequency noise of a stabilized laser, which used a similar setup to ours, has been reported as $\sim 20/f$ Hz/$\sqrt{\text{Hz}}$ at frequency f [70]. We adopt this value as a rough estimation of the stability of reference. The reference stability is estimated to limit the actual frequency stability up to about 1 kHz.

Other noise sources, such as Doppler shift, the servo circuit noise, the seismic noise, and the phase noise caused by non-isolated mirrors, are thought to be negligible in our observation band. As a result, the actual frequency stability is estimated to be the thick curve in Fig.4.19. Between 100 Hz and 30 kHz the stability is believed to satisfy our required goal sensitivity, even if the shot noise or the reference stability noise limits the frequency stability. Over 30 kHz, because of the insufficient open-loop gain, the frequency stability did not satisfy our requirement. The remaining frequency noise was entrusted to the differential measurement.

Stability evaluated by an external cavity

The actual stability was evaluated by comparison with an external longer cavity[14]. The 3-m cavity, which uses the same laser source, is connected to the reference cavity tank. Figure 4.20 shows the setup for the measurement. The cavity is made of two independently suspended mirrors, which are highly isolated from the seismic motion using low-frequency vibration isolation system (Seismic Attenuation System, SAS) developed for future implementation in TAMA [71]. Figure 4.21 shows the sensitivity of the 3-m cavity with and without the frequency stabilization.

The sensitivity was improved by a factor of 10 between about 10 Hz and 500 Hz by the frequency stabilization. The sensitivity is still limited by seismic noise below

[14] Joint work with Akiteru Takamori. The details of the cavity, and its low-frequency vibration isolation systems are explained in his PhD thesis [72].

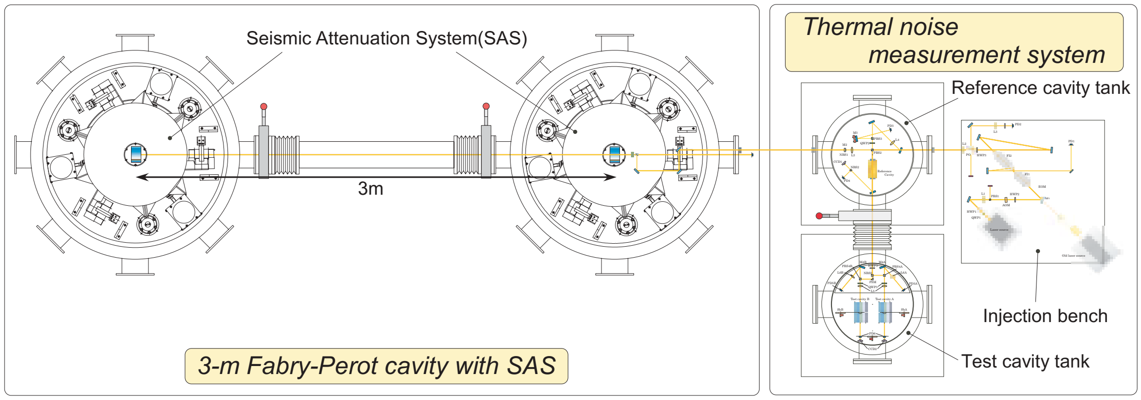

Figure 4.20: 3-m Fabry-Perot cavity connected to the thermal noise measurement system.

4 Hz, and by the electric circuit noises, such as the filter noise and the detector noise, above that frequency range. However, from this result, we confirmed that the system actually suppressed the frequency noise of the laser, and that its gain was sufficient for the thermal noise measurement.

4.3 Detection system, control system and others

In this section, the signal detection system, control system for the test cavity, other optics components and the vacuum system are described. The signal detection system is composed of modulator, RF photo detector, and demodulator.

4.3.1 Modulator

We used the Pound-Drever-Hall technique to control all of three Fabry-Perot cavities [62]. The laser beam is phase-modulated by an EOM (New Focus Inc., model 4003) on the injection bench. The EOM is made up of a $LiNbO_3$ crystal and a tank circuit tuned at 40 MHz. In order to reduce the amplitude modulation at the modulation frequency, the polarization of the beam is adjusted to match the EOM's crystal axis by rotating a half wave plate (HWP2). The EOM is driven by a commercial oscillator (SONY Techtronics, AFG2020) at 40.000 MHz through a band pass filter tuned at that frequency. We set the output voltage of the oscillator on its maximum, because we found in our case that deeper modulation was better for reducing shot noise in the test cavity. The resultant modulation index was 0.59 rad.

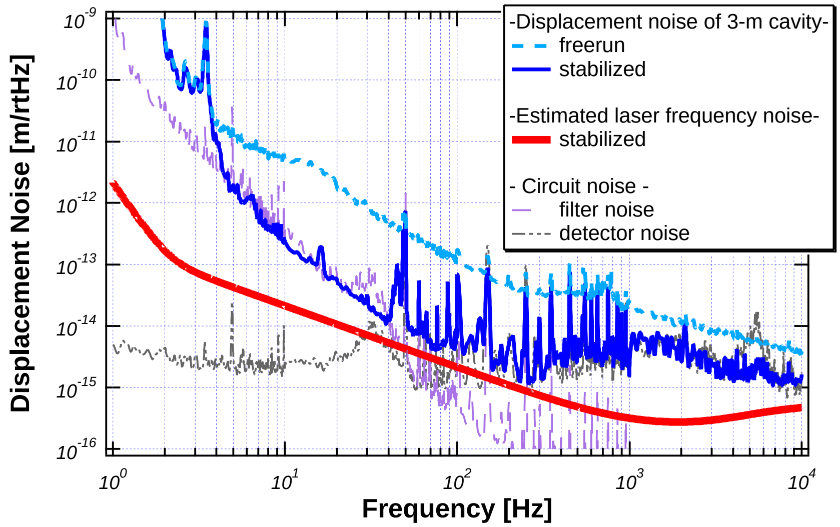

Figure 4.21: Sensitivity of the 3-m interferometer with and without the frequency stabilization [72]; Thick curve shows the stability estimated only by the reference cavity servo loop. It corresponds to a thick curve in Fig.4.19.

4.3.2 RF photo detector and demodulator

RF photo detector

The PDH error signal is extracted at PD3 for the reference cavity, and at PD5-A, and -B for the test cavities. These are RF photo detectors that detect the intensity changes at the modulation frequency (40 MHz) in the reflected light from their corresponding cavities. The response speed of the photo detector must be high, and at the same time, they have to be low noise. In addition, PD5-A and -B must be compatible with high power.

The PD3 is a In-Ga-As photodiode with a diameter of 1mm (EG&G optoelectronics Inc., C30641), followed by a tank circuit that converts its photocurrent to voltage with high efficiency, and pre-amplifiers. The Q of the tank circuit of PD3 was measured to be 11.

The conceptual design of PD5-A and -B is very similar to that of the photo detectors currently used in TAMA [73]. Their photodiodes are also In-Ga-As type with a diameter of 1mm (HAMAMATSU photonics, G3476-10). Additional capacitance was attached in parallel to the photodiode to mask the change in resonant frequency caused by the capacitance change due to incident power variation. The tank circuit (measured Q: 17) follows the photodiode-capacitor set. Figure 4.22 shows the frequency response of PD5. The photodiode is directly connected for cooling to a copper heat sink, which is also directly in contact with the housing of the photo

Table 4.5: Properties of the photo detectors.

	PD3	PD5
Used for	reference cavity	test cavity
Photodiode	C30641(EG&G)	G3476-10(HAMAMATSU)
Quantum efficiency η (A/W)	0.75	0.75
Capacitance	NA	30 pF
Q of tank circuit	11	17
Noise equivalent current $I_{\rm det}$(mA)	0.402	0.304
Equivalent resistor $R_{\rm det}$ (kΩ)	262	2.61
Typical light power on PD (mW)	20	220

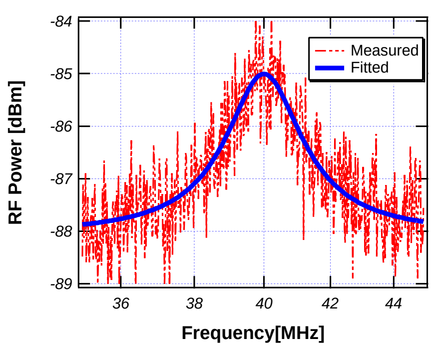

Figure 4.22: Frequency response of PD5.

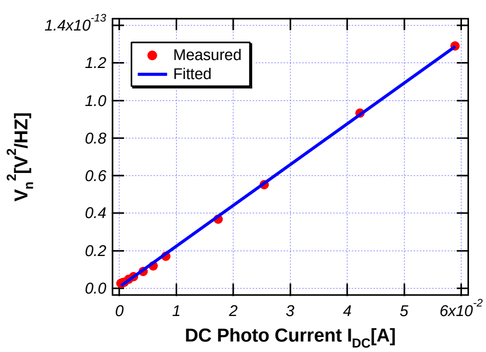

Figure 4.23: PD5 output noise at the modulation frequency.

detector.

Demodulator and noise performance

The detected RF signal is demodulated and down-converted to AF signal by a Double Balanced Mixer (DBM). We used a commercial diplexer M-1 from R&K Corporation as the demodulator. Their local oscillators, which are phase-shifted to lock in-phase, are provided by an RF distributor that drives the EOM. The demodulated signal is filtered by a low pass filter.

The output voltage noise from the demodulator, $V_{\rm n}$, represents the sum of the shot noise and of the detector noise in general [74]. The equivalent photo current noise, $I_{\rm det}$, is defined by,

$$V_{\rm n}^2 = 2eR_{\rm det}^2(I_{\rm DC} + I_{\rm det}). \tag{4.1}$$

Here, $R_{\rm det}$ is the equivalent resistance for the current-to-voltage conversion, and $I_{\rm DC}$ is the DC photocurrent. To make the noise of the detection system negligible compared to the shot noise, $I_{\rm det}$ has to be smaller than $I_{\rm DC}$. Figure 4.23 shows the measured demodulated output voltage of PD5 as a function of the DC photocurrent. The response is fitted by Eq.(4.1), and the results are summarized in Table 4.5. The noise equivalent photocurrents, $I_{\rm det}$, were calculated to be 402 μA in PD3 and 304 μA in PD5. Typical photocurrents under operation are 2 mA (PD3) and 20 mA (PD5), which are larger than the noise equivalent photocurrents. Therefore, the photo detectors and the demodulation system satisfy our demands of fast low-noise, and high-power compatibility (in PD5).

4.3.3 Servo system for the test cavity

The detected signal at PD5 is demodulated by DBM, and then sent to the control servo circuit for the test cavity. The displacement noise in each cavity is extracted from the error signal of the servo loop. Two error signals are subtracted that multiply a DC gain, producing a differential displacement noise.

In the following, we describe the open-loop transfer function of the test cavity loop, calibration of the displacement noise, and the differential measurement between the two cavities.

Open-loop transfer function of the test cavity servo

Figure 4.24 shows the block diagram of the test cavity servo system. The displacement noise δx is filtered by the cavity transfer function, $C_{\rm T}$. The displacement is converted by the PDH method into a voltage thorough a displacement-to-voltage conversion

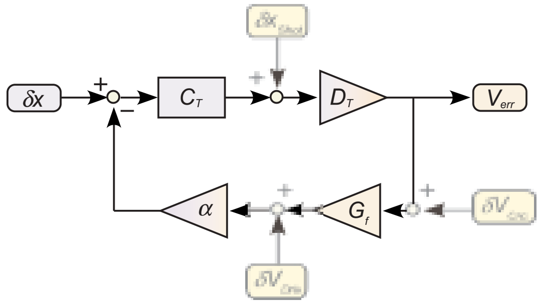

Figure 4.24: Block diagram of the test cavity servo; δx: displacement noise, C_{T}: cavity transfer function, D_{T}: displacement-to-voltage conversion factor, G_{f}: servo circuit transfer function, α: actuation efficiency. The following are mentioned in Chapter 5; δx_{shot}: shot noise, δV_{Circ}: input equivalent servo circuit noise, δV_{Driv}: coil driving circuit noise.

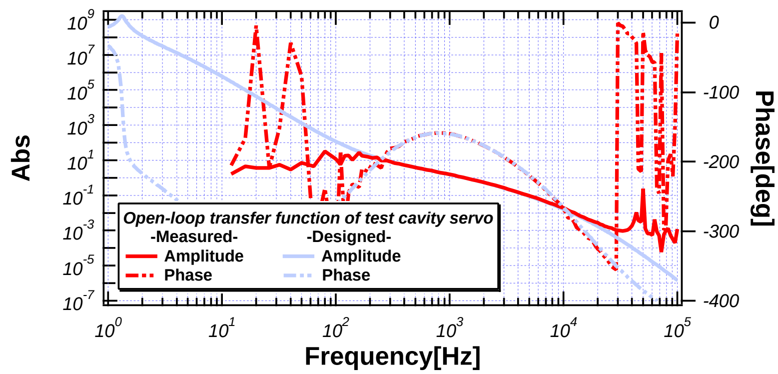

Figure 4.25: Typical open-loop transfer function of the test cavity servo.

factor, D_{T}, producing error signal, V_{err}. It is filtered by an electric servo circuit G_{f}, producing the feedback signal. The feedback signal pushes the coil with an efficiency of α. Here, an open-loop transfer function of the test cavity loop, G_{OL}, is,

$$G_{\mathrm{OL}} = C_{\mathrm{T}} D_{\mathrm{T}} G_{\mathrm{f}} \alpha \sim D_{\mathrm{T}} G_{\mathrm{f}} \alpha. \tag{4.2}$$

We designed a servo loop with transfer function, G_{f}, considering simple realization as a circuit. It has high gain at low frequency, low gain at mirror resonance, and low-noise performance. Figure 4.25 shows the typical open-loop transfer function G_{OL}. The measured result in one of the test cavities and the DC-gain fitted model are shown[15]. The unity gain frequency was about 1 kHz. Two equivalent circuits were made for the two test cavities. In actual operation, the two differed only in their DC gains.

[15]This servo has not been completely optimized; for example, the typical phase margin is relatively small – about 20 deg. However, we got successful results with this servo system, and we used it throughout the following experiment commonly.

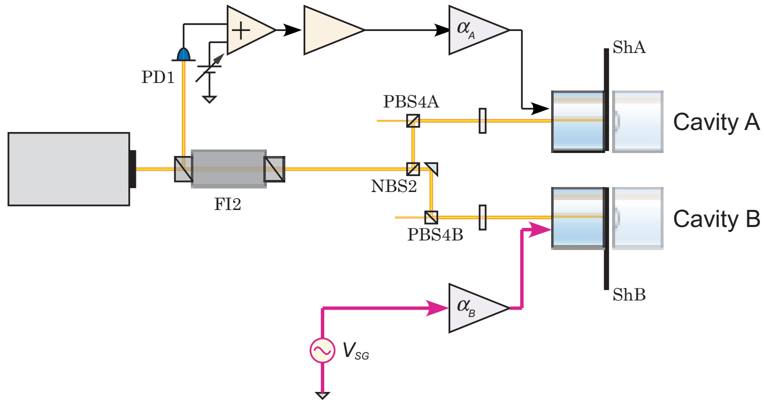

Figure 4.26: Experimental method to determine the efficiencies of the actuators by Michelson interferometer.

Calibration of the displacement noise

In order to calibrate the displacement noise spectrum δx from the voltage signal, we measured the actuator efficiency α and determined the displacement-to-voltage conversion factor, D_{T}. For the measurement, Michelson interferometer formed by the two front mirrors was used[16].

Figure 4.26 shows the configuration to measure the actuation efficiencies α. At first, the two shutters (Sh-A and -B) are inserted to prevent the incident beam from resonating inside the cavity. The beams reflect back on the inner surfaces of the front mirrors. Small fractions of the beams interfere on the photo detector (PD1), which makes a Michelson fringe, through PBS4-A or -B, NBS2, and the Faraday isolator (FI2). We locked the Michelson interferometer using an appropriate servo circuit and the actuators on one of the front mirrors. By measuring the open-loop transfer function and by shaking the other uncontrolled mirror, we experimentally determined[17] two actuation efficiencies in cavity A and B.

After the conversion factor D_{T} is calculated from Eq.(4.2) based on the measured actuation efficiency α, the open-loop transfer function G_{OL} and the servo transfer function G_{f}, the displacement noise spectrum is calibrated from the spectrum of the error signal[18]. We estimate that the measurement error of the displacement spectrum,

[16]This procedure is popular for the prototype interferometer and the interferometric detectors under construction. For example, we can find its detail in Ref.[75].

[17]In order to confirm the measurement, we exchanged the locking mirror and the shaking mirror, keeping the gain of the circuit, and repeated the procedure. Also, the measurement was further confirmed by observing an error signal of the Michelson interferometer while a sinusoidal signal is applied on the PZT of the laser frequency tuning, whose efficiency was already known.

[18]In general, because of the existence of the electronics noise, which adds after the error signal, this conversion method is not appropriate within the bandwidth. In our case, since we designed a

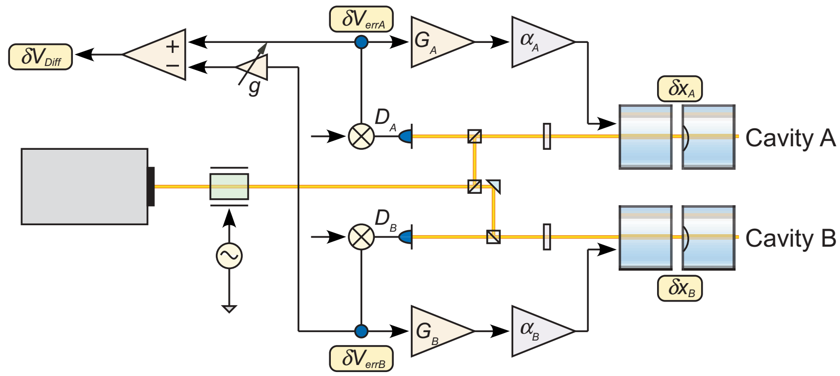

Figure 4.27: Scheme of the differential measurement; The two error signals from the two cavities are subtracted with an appropriate weight g.

which originates in D_{T} is 10% at most, by the measurement procedure of the actuation efficiency α.

Differential measurement between two cavities

To reduce the common mode noise, especially the laser frequency noise, the two error signals from the two equivalent cavities are subtracted, producing a differential signal.

Figure 4.27 shows the scheme of the differential measurement. Two test cavities produce two PDH signals with two slightly different displacement-to-voltage conversion factors. The displacements in each cavity, δx_{A} and δx_{B}, appear in the error signal, δV_{errA} and δV_{errB}, after suppression by their open-loop transfer functions. Before subtraction of the two error signals, we electrically multiplied one of the error signals by an adjustable gain g. By setting g as the ratio of the two displacement-to-voltage conversion factors, and adjusting two open-loop transfer functions to be equal, the subtracted voltage, δV_{diff}, can be converted to a differential displacement, $\delta x_{\mathrm{A}} - \delta x_{\mathrm{B}}$, using one of the test cavity parameters.

Figure 4.28 shows the typical Common Mode Rejection Ratio (CMRR) for the frequency noise. Typical CMRR was 1/100 above 10 kHz. The limiting factor of CMRR at this frequency region was the accuracy of the subtraction gain g. In this region below 1 kHz, the CMRR is limited by the difference of the two open-loop gains.

4.3.4 Other optics

In this section, we describe the optics components for the monitors and the measurements; AF photo detectors and mode matching lenses.

---

low noise circuit, we could simply extract a displacement spectrum only from the error signal at entire frequency range.

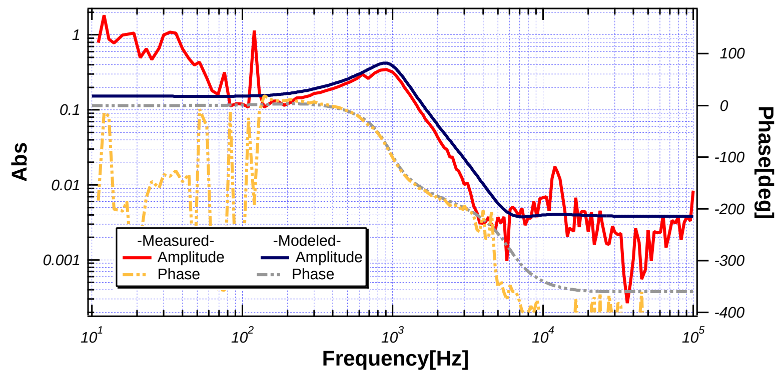

Figure 4.28: Typical CMRR for frequency noise; This is a transfer function from one of the error signal to the differential error signal ($V_{\rm diff}/V_{\rm errA}$ in Fig.4.27). Its amplitude corresponds to the CMRR. This CMRR measurement was done by comparing the differential error signal and the single error signal, while a sinusoidal signal was applied on the PZT for the laser frequency tuning.

AF photo detectors

PD1, PD2, PD4, and PD6 are the AF photo detectors. They are silicon photodiodes coupled to transimpedance amplifiers. PD1 is mainly for monitoring the reflected beam from the cavities. The beams from the cavities are interfered on the PD1, making Michelson fringes. PD2 is for monitoring the intensity change of the injected beam to the cavities. PD4 and PD6 are for monitoring the transmitted light of the cavities. PD6 is mounted on a motorized shutter, which is used for switching the beam between the PD and a CCD (CCD2) for mode monitoring. The photo detectors are mainly used during the adjustment process of aligning the cavities.

Mode matching lenses

In order to match the mode of the laser beam with those of each cavity, mode-matching lenses (L1∼L5) are used. Most of the lenses are mounted on translation stages to allow the adjustment of their positions by observing matching ratio. We used normal plano-convex lenses for mode matching. The main higher-order mode that can resonate in the cavities was TEM_{20}[19].

[19]This is because of the elliptic beam of the laser source. We did not reshape it into a circular beam using cylindrical lenses to avoid increasing the degrees of freedoms.

4.3.5 Vacuum system

Except for the input optics on the injection bench, every component of the system is housed in a vacuum system in order to reduce the effect of sound, air motion, changes in refraction index along the optical path, and so on. Figure 4.29 shows the vacuum system used in this experiment. Two almost identical vacuum tanks are used for the reference cavity and for the test cavity. The system is relatively compact – their inner diameter is about 50 cm. Every component was designed to fit inside. The system is evacuated with a rotary pump connected to the test cavity tank. The typical vacuum level is a few Pascal. No effect of sound on the interferometer's sensitivity has been observed at this level[20]. The rotary pump is switched off during operation to avoid excess vibration. The leakage speed is sufficiently slow (order of a week) to perform the experiment.

[20] An oil diffusion pump had been attached to the test cavity tank at the beginning. It was removed to avoid complexity and problems, like oil contamination and inclination of the vacuum tank caused by its weight.

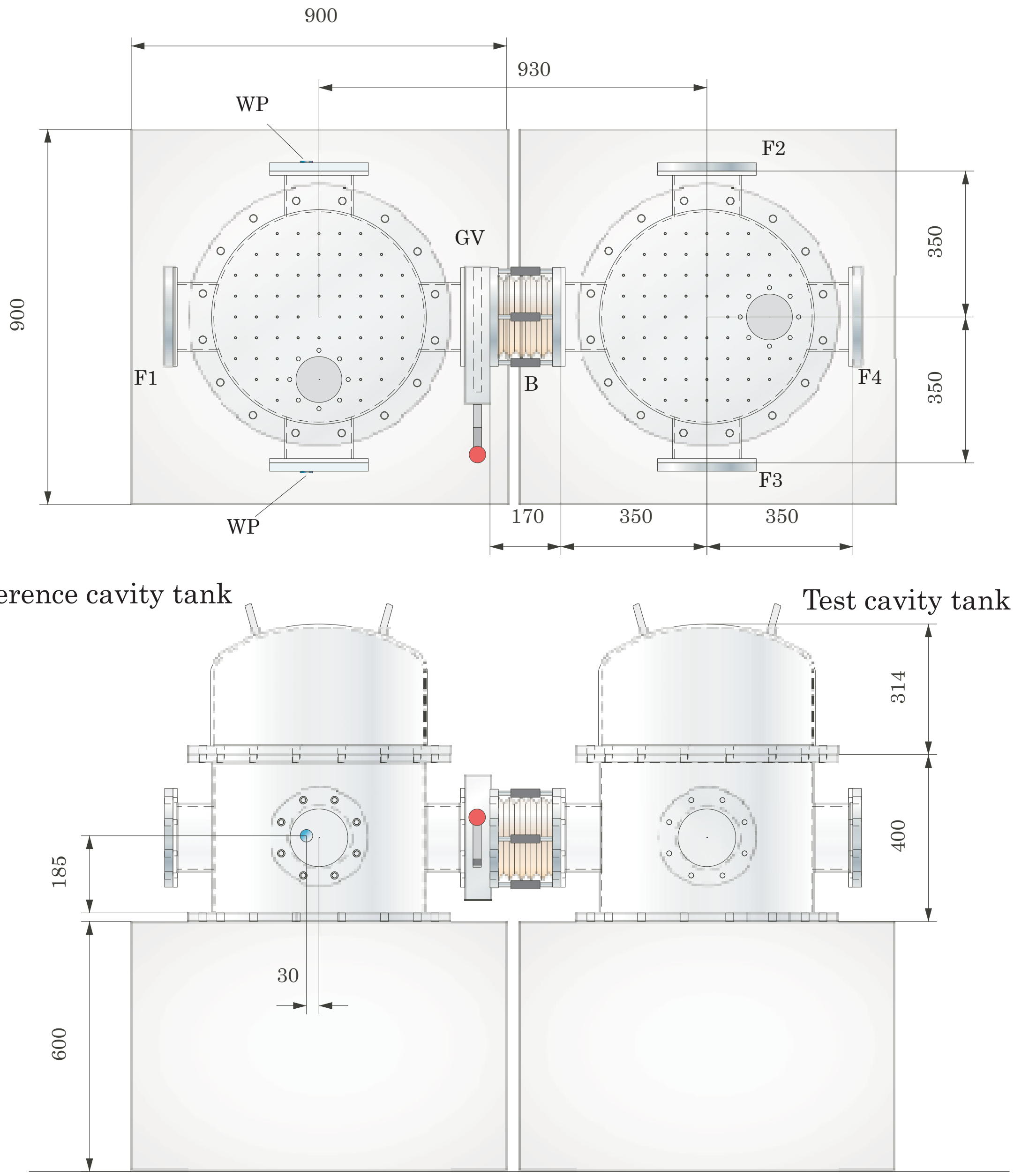

Figure 4.29: Vacuum system; Twin vacuum tanks were used for the experiment. One of them (left) is for the reference cavity and the other (right) is for test cavities and their optics. They are made of stainless steel. WP: window plate, GV: gate valve, B: bellows, F1$\sim$F4: steel flanges. A rotary vacuum pump is attached on F4. The other flanges are used for feed-through cabling.

Chapter 5

Experimental result

In this chapter, we will describe experimental results of the direct measurement of mirror thermal noise in the test cavity.

We could achieve high sensitivity to observe mirror thermal noises over a wide frequency range (100 Hz to 100 kHz) as we designed. In both of the configurations, that is, BK7 cavity for the Brownian noise measurement and CaF_2 cavity for the thermoelastic noise measurement, the measured results agreed very well with the theoretical calculations. The displacement noise floor around the mechanical resonances of mirror was directly observed.

We first show the measured noise spectrum in BK7 cavity and its comparison with the theoretical Brownian noise. Second, we show the measured noise spectrum in CaF_2 cavity and its comparison with the theoretical thermoelastic noise. Finally, we evaluate other noise sources of the interferometer.

5.1 Result on BK7 cavity

In this section, the measured results on BK7 cavity will be shown. First we show the measured results obtained with and without the frequency stabilization. We measured three displacement noises in each configuration: cavity-A, cavity-B, and their differential signal. We then compare minutely the measured spectrum with the theoretical mirror thermal noise level.

5.1.1 Measured displacement noise

With the frequency stabilization

Figure 5.1 shows the measured displacement noise in the test cavity formed by BK7 mirrors with the frequency stabilization. Two independent noises in the cavity A and in the cavity B, and the differential noises are plotted on the figure. All these three

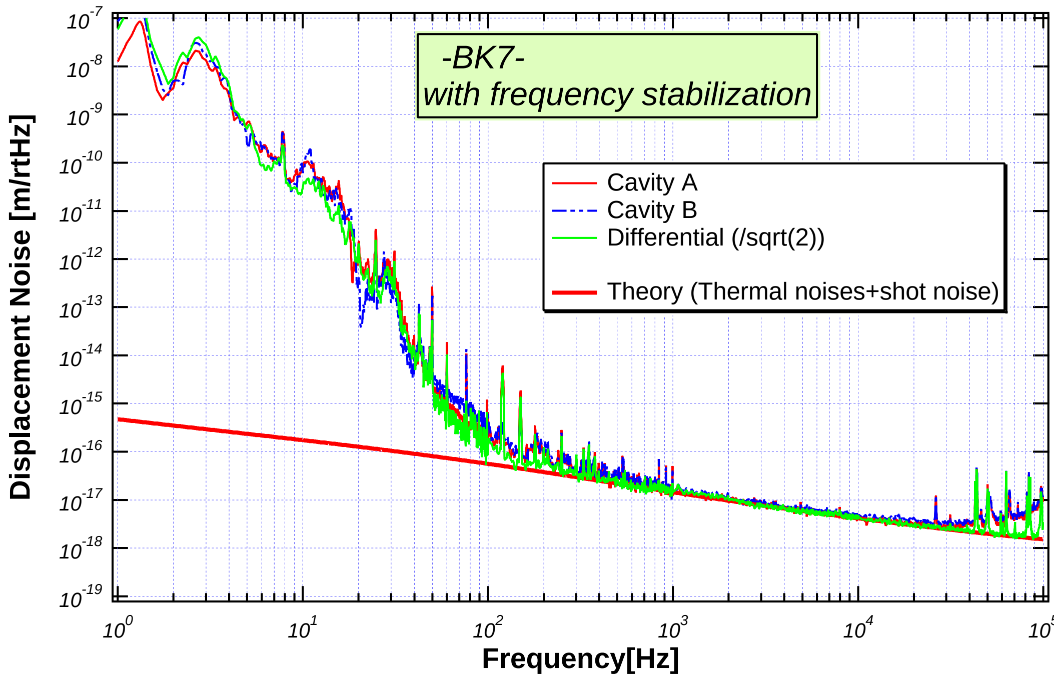

Figure 5.1: Displacement spectrum of BK7 cavity with the frequency stabilization; Three measured displacement noises are shown. Theoretical line represents sum of the calculated thermal noise level and of shot noise.

spectra were obtained from their corresponding error signals. The plotted differential spectrum was multiplied by $1/\sqrt{2}$. The theoretical line indicates the calculated thermal noise level (plus shot noise) in our setup. Figure 5.2 shows in detail each contribution to the theoretical line with the measured spectrum.

Without the differential measurement, the two single cavities showed equivalent noises in our observation band. The displacement noises in a single cavity agreed well with the theoretical thermal noise level except below 300 Hz, and above 20 kHz. By the differential measurement, the displacement noise was reduced above 20 kHz. This was because the frequency noise was subtracted. It was also effective between about 100 Hz and 300 Hz, reducing beam jitter or amplitude modulation caused by EOM[1].

Without the frequency stabilization

Figure 5.3 shows the displacement noise when the frequency stabilization was not activated. As in Fig.5.1, the three displacement noises and theoretical thermal noise are plotted on the graph.

In this case, the two single cavities showed almost identical results, which were

[1]We observed the noise increased at this frequency range when the modulation index was large.

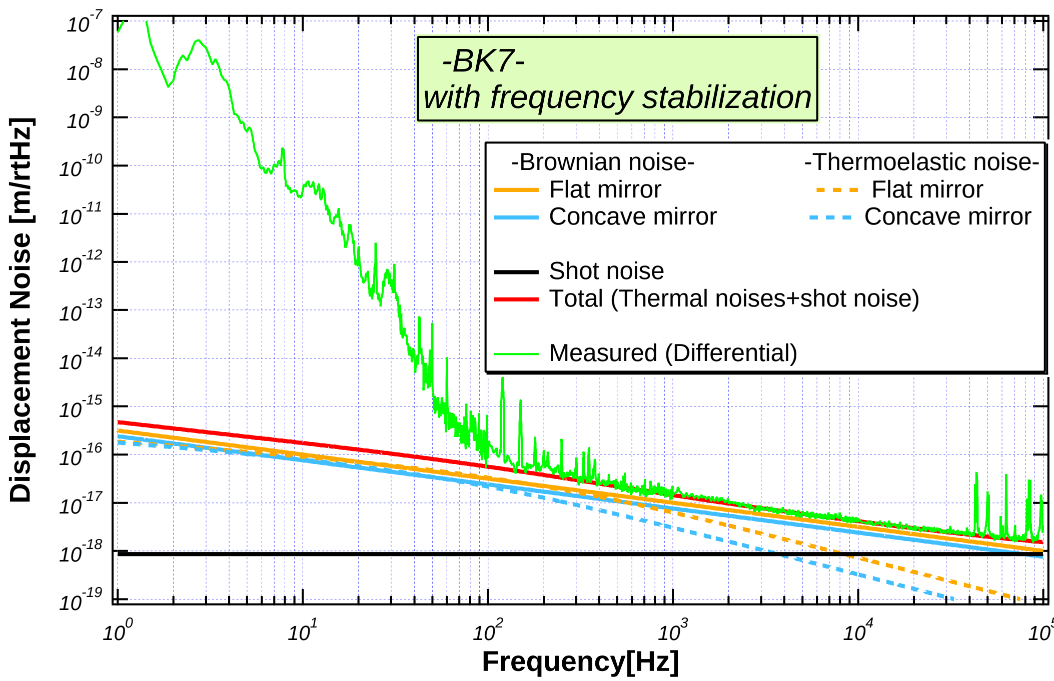

Figure 5.2: Measured displacement spectrum in BK7 cavity and theoretical thermal noises; Measured result is shown with every theoretical thermal noise. For the calculation of Brownian noise, we used the direct approach with the intrinsic quality factor.

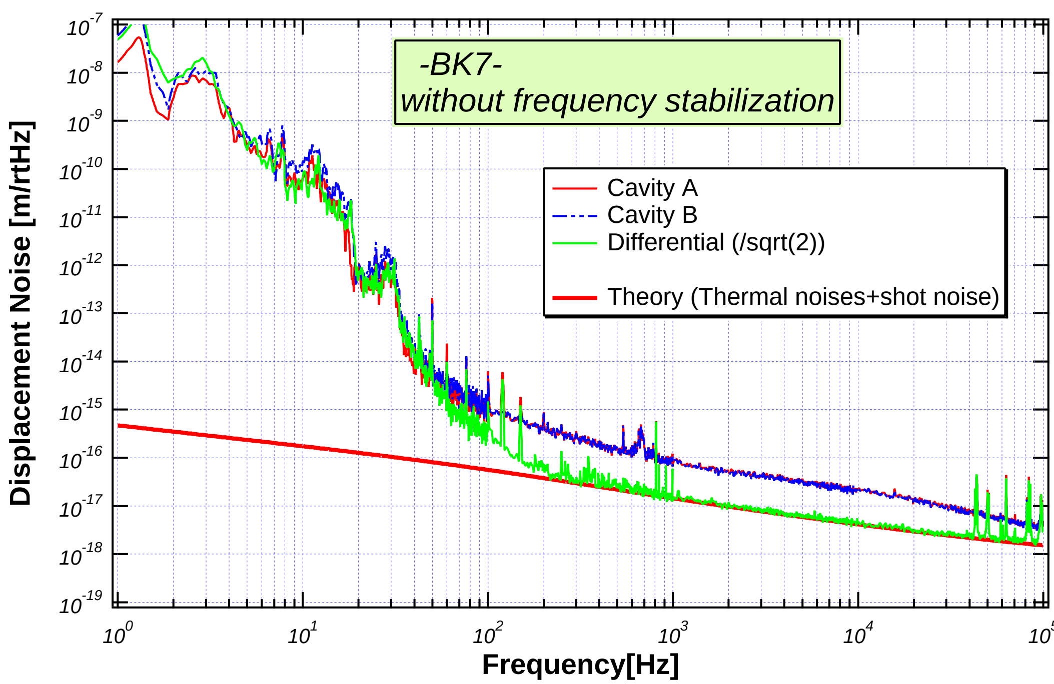

Figure 5.3: Displacement spectrum of BK7 cavity without the frequency stabilization.

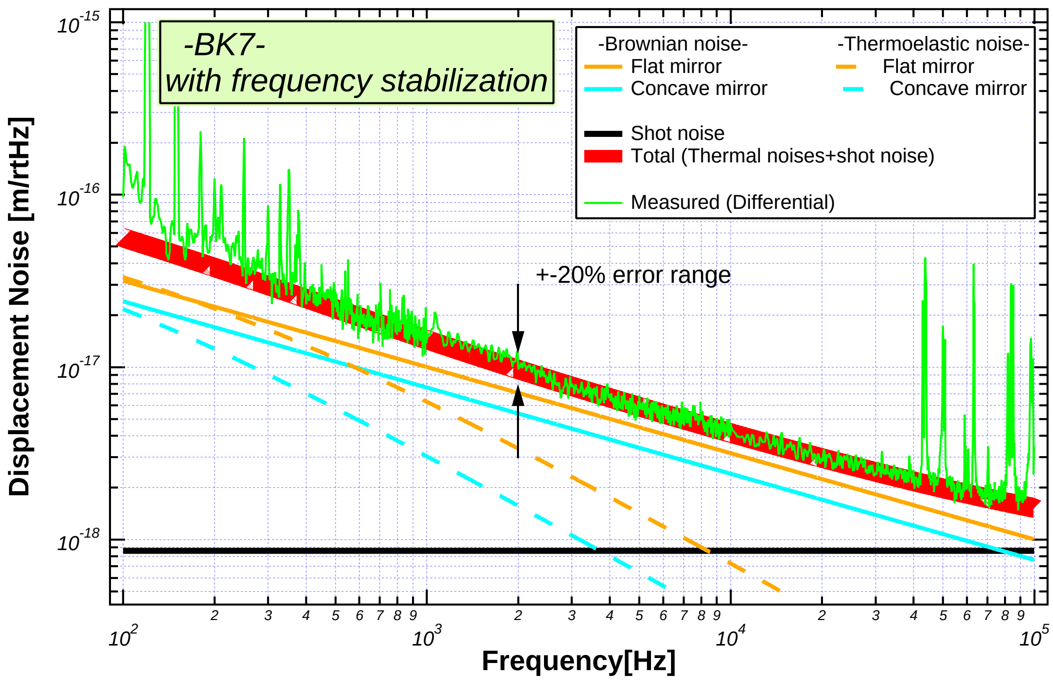

Figure 5.4: Comparison with the theoretical thermal noise level in BK7 cavity.

larger than the theoretical thermal noise level by a factor of 10 at most. By subtracting the two signals, the sensitivity was improved in the measurement band, reaching the thermal noise level over a wide frequency range. The differential noise agreed well also with the three spectra, along with the frequency stabilization.

5.1.2 Comparison with the theory

Closer view of the measured displacement noise

Figure 5.4 magnifies Fig.5.2 between 100 Hz and 100 kHz. As discussed later in detail, there is no noise source other than the mirror thermal noise in this frequency range. The measured displacement noise agreed with the theoretical thermal noise level, in which the Brownian noises from the two mirrors dominated, within the calculation error of 20% (discussed below). Therefore, the measured displacement noise cannot be other than the mirror thermal noise. The noise has no correlation between the two cavities. This is another corroboration for the fact that the measured noise is the mirror thermal noise. The measured thermal noise has $1/f^{1/2}$ frequency dependence, which does not contradict the fact that the BK7 substrate has structural loss.

Calculation error evaluation

We estimate that the calculation error is ~20% in $\sqrt{G}$ because of the following evaluation. The Brownian noise floor is calculated by Eq.(3.26), which is a static limit by direct approach[2], substituting $\phi_{\rm sub}$ of 1/3600. This value is the measured intrinsic loss by the nodal support system (see Appendix B). One of the most probable source of calculation error is the mechanical loss of substrate, $\phi_{\rm sub}$. The test substrate that we used for the quality factor measurement using the nodal support system was not an actual mirror. There is a possibility that the intrinsic loss of the mirror was smaller than that of the test substrate[3]. This could cause a calculation error of −11%. The other possible factor is the coating. The coating effect is theoretically predicted from Eq.(3.29)[4]. By substituting the coating factor, $\phi_{\rm coat}d$, of 10^{-8} [m], which is believed to be the upper limit, the total thermal noise becomes larger by +21%.

Other parameters do not affect the total calculation very much. We have confirmed that the error caused by the infinite-half space approximation was less than 0.3% (see Appendix A). The error from Young's modulus error is estimated to be less than 2%[5]. Cavity length error, which leads to a beam radius w_0 error, causes less than 1% error in our case[6].

5.2 Result on CaF_2 cavity

In this section, we describe the results obtained with the CaF_2 cavity. We first modified the original arrangement of the test cavities, and then repeated essentially the same measurements as BK7's case. Except for the modification, we obtained the following result just by replacing the mirror in the suspension.

5.2.1 Setup modification

We found that the CaF_2 mirror that we got had unfortunately low quality coating. Since its transmissivity was quite low (~0.1%), it could not be used as front mirrors. Also, we found that one of the concave mirrors had very low reflectance. So it could

[2]Estimation by the modal expansion will be discussed in Chapter 6.

[3]Maximum quality factor of the mirror was 4400.

[4]This equation assumes that the loss of coating is much larger than that of substrate. This assumption is not so suitable for this case. The following argument gives a rough upper limit of the calculation error.

[5]Our calculation using finite element method showed that the Young's modulus should be shifted by 3% from the datasheet value.

[6]The beam radius depends on the cavity length, which has 10% error (±1 mm). By considering the fact that the beam radius of the front mirror and that of the end mirror have opposite dependence on cavity length, the length error causes small error on the thermal noise.

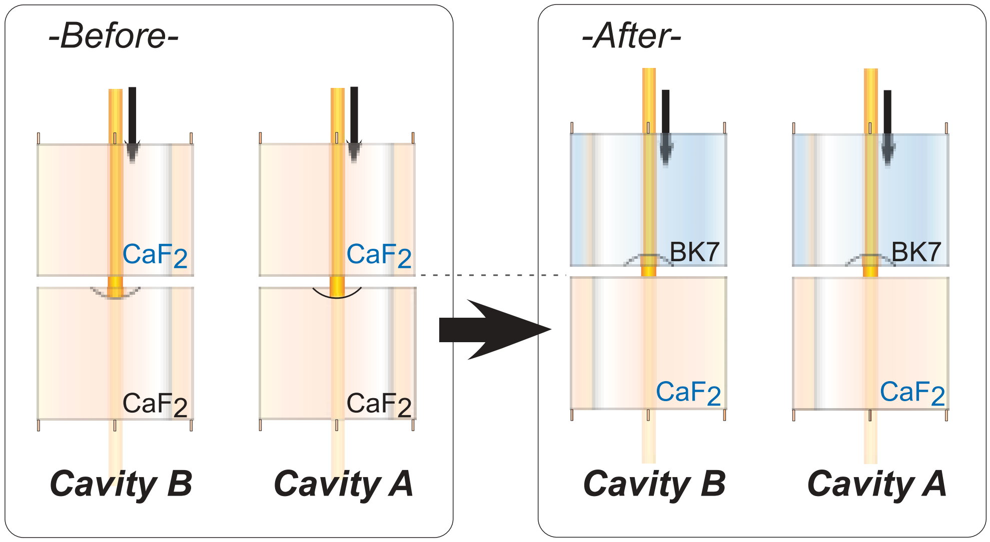

Figure 5.5: Modification of the setup; In order to overcome the low transmissivity of the coating on our CaF_2 mirror, we used flat CaF_2 mirrors as end mirrors of Fabry-Perot cavities combining with concave BK7 mirrors.

not be used as an end mirror. On that account, we decided to change our original setup, while maintaining as much as possible the dominant thermoelastic noise caused by CaF_2 mirror. What we did was to use the two flat mirrors made of CaF_2 as end mirrors of the Fabry-Perot cavities, combining them with the concave mirrors made of BK7. Figure 5.5 shows this modification to overcome the low quality coating on the CaF_2 mirror. Even if we cannot evaluate the thermoelastic noise from the concave CaF_2 mirror in the modified configuration, the thermoelastic noise of the flat CaF_2 mirror should be larger than the Brownian noise from the concave BK7 mirror below 20 kHz according to the theories, because of the smaller beam radius on the flat mirror.

5.2.2 Measured displacement noise

With the frequency stabilization

Figure 5.6 shows the measured spectrum in the setup with the frequency stabilization. As in Fig.5.1, the three sensitivities are plotted together – cavity-A , -B, and their differential motion divided by $\sqrt{2}$. Theoretical thermal noise level (plus shot noise) is also plotted on the graph. Figure 5.7 shows the different components of the thermal noise separately as well as the measured displacement noise[7].

[7]The theoretical line differs from the original goal sensitivity in which only CaF_2 mirrors were assumed. Along with the alternation of the setup, the theoretical line has the contribution from thermal noise in concave BK7 mirror that is not included in concave CaF_2 mirror (see Fig.4.1).

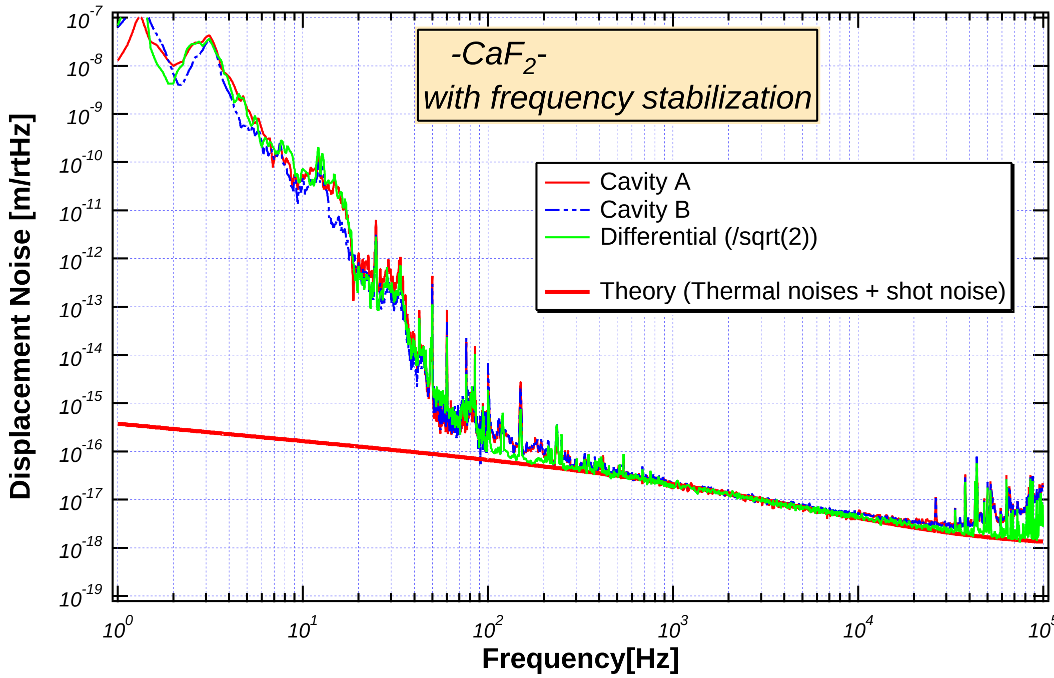

Figure 5.6: Displacement spectrum of CaF_2-BK7 cavity with the frequency stabilization.

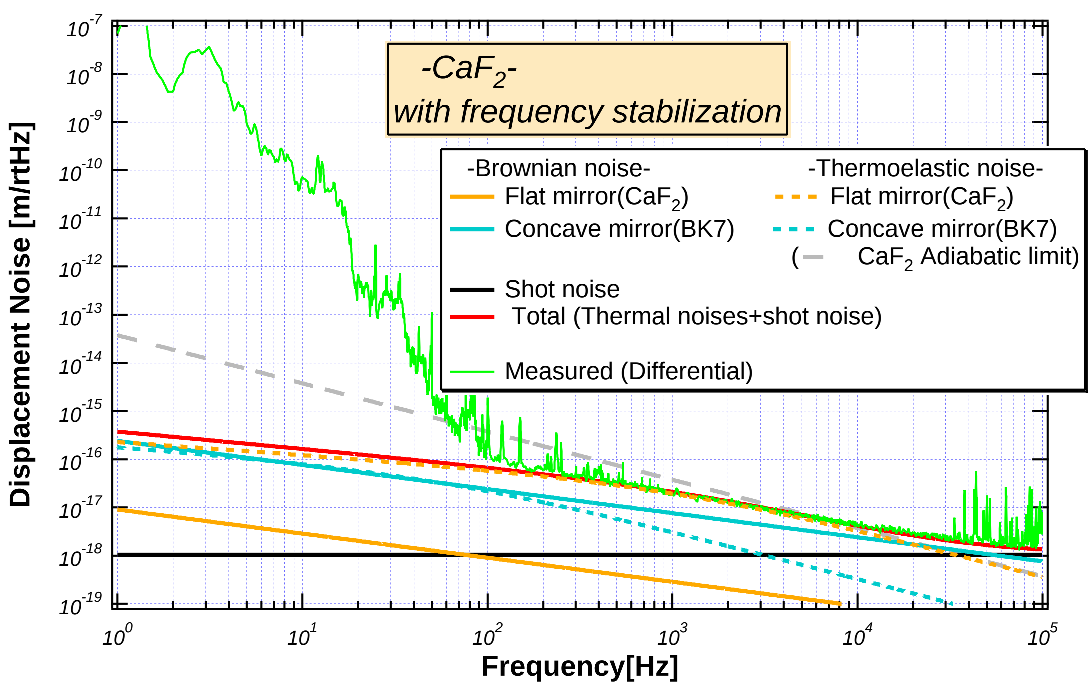

Figure 5.7: Measured displacement spectrum in CaF_2-BK7 cavity and theoretical thermal noises; Measured result by differential measurement is shown with every theoretical thermal noise.

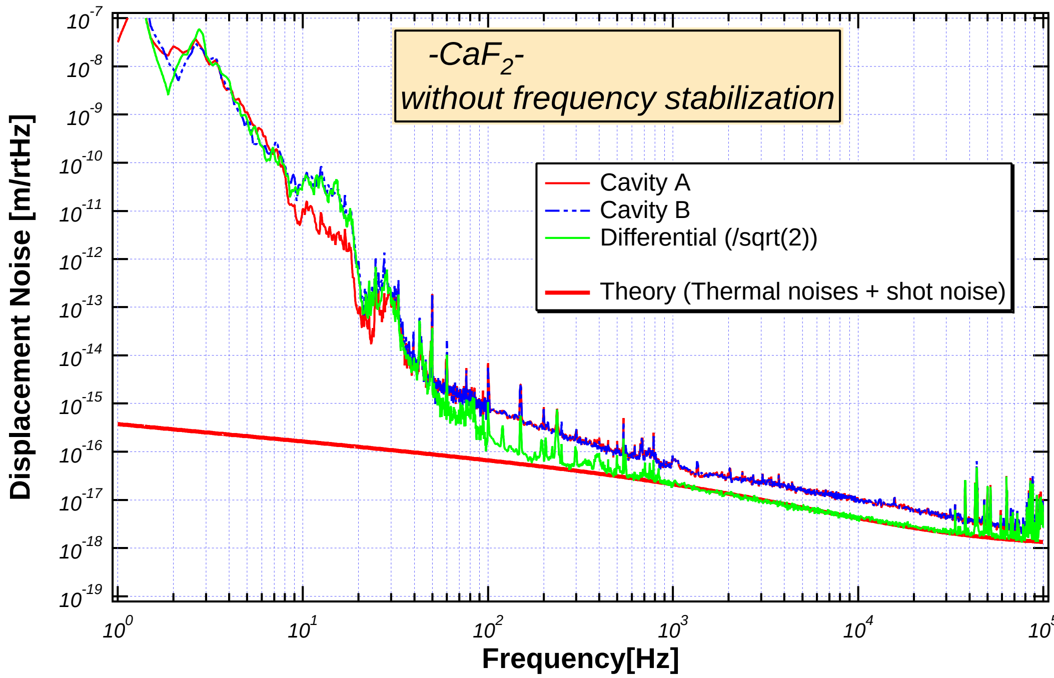

Figure 5.8: Displacement spectrum of CaF_2-BK7 cavity without the frequency stabilization.

The three measured displacement noises are mostly equivalent below 20 kHz. At that frequency region, their level agreed very well with the theoretical curve of thermal noise. Above 20 kHz, only the differential signal agreed with the theoretical level[8].

Without the frequency stabilization

We also performed the measurement on CaF_2 (and BK7) mirrors without using our frequency stabilization system.

Figure 5.8 shows the result. The sensitivities obtained using the single cavities were worse than the sensitivity with the frequency stabilization. By subtracting these two signals, the sensitivity was improved by about 2 times in almost all of the frequency range, attaining the theoretical thermal noise level.

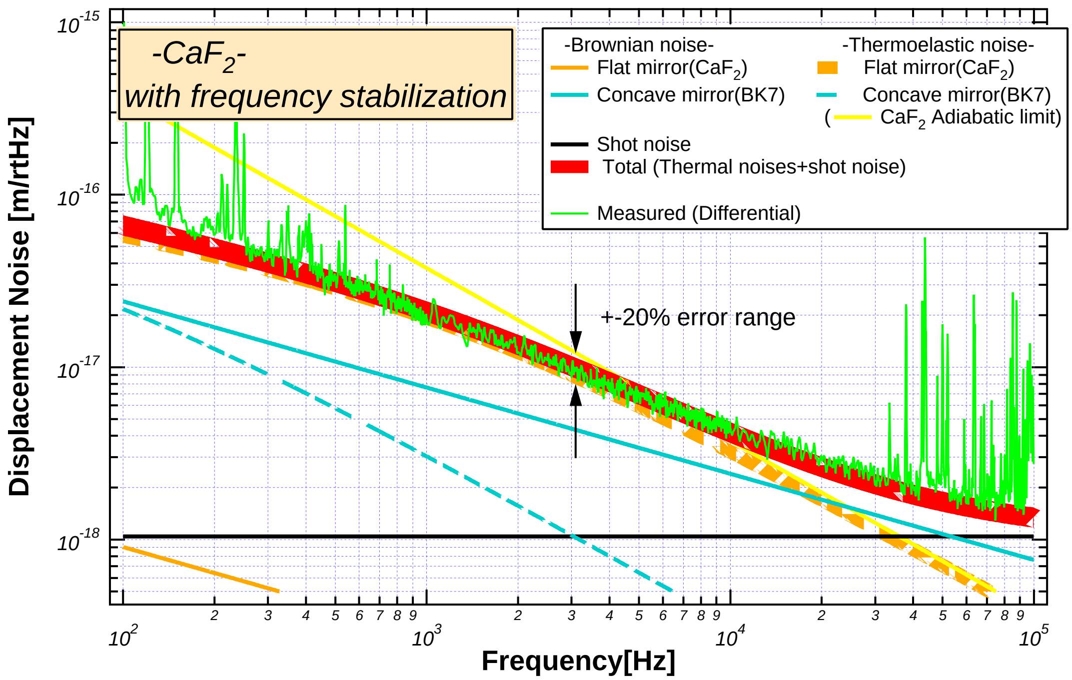

Figure 5.9: Comparison with the theoretical thermal noise level in CaF_2-BK7 cavity.

5.2.3 Comparison with the theory

Closer view of the measured displacement noise

Figure 5.9 magnifies Fig.5.7 between 100 Hz and 100 kHz. Our results coincide with the Eq.(3.37) within the calculation error of 20% (discussed below) above 900 Hz. Although the spectrum was disturbed by the electric noises[9] below that frequency, we can see that the measured spectrum does not agree with the adiabatic approximation of thermoelastic noise calculated by Eq.(3.36).

Calculation error evaluation

We evaluate the calculation error of the thermoelastic noise as about 20% according to the following considerations. Thermoelastic noise is calculated from Eq.(3.37), which is for infinite half space. The use of a solution for infinite half space is reasonable

[8]At first sight, the measured displacement noise is not so different from the BK7's case. When Fig.5.6 is closely looked at, however, one notices that there is a point of inflection at around 30 kHz, at which the thermoelastic noise becomes negligible, and that the displacement-noise curve is convex through a wide frequency range (100 Hz $\sim$ 30 kHz), which is the specific feature of thermoelastic noise.

[9]Other possible explanation was thermal absorption on the mirror, which had low transmittance. We observed that the noise increased when the beam was on a specific point on the mirror.

in our case because of the extremely small beam radius[10]. The most dominant error here is the thermal linear expansion coefficient, α, which varies by $\pm 10\%$ depending on references[11] and linearly couples to the displacement spectrum $\sqrt{G}$. Another cause of error is the beam radius w_0, which has 3/2 power behavior. In our case, the effect appears as 5% error in the calculation result with the cavity length error of 10%. The other thermal parameters of the material are estimated to result in few percent errors. By considering these errors, we estimate the calculation error in CaF_2 thermoelastic noise as $\sim$20%.

5.3 Noise analysis

In this section, we consider possible noise sources of the interferometer. Any noises, other than mirror thermal noises, are estimated to be not responsible for the measured displacement noise.

5.3.1 Frequency noise

The frequency noise is one of the fundamental noise sources for this measurement. In this experiment, the effect was brought to be negligible by the differential measurement and by the frequency stabilization. In the following we evaluate the contribution of the frequency noise in detail.

With frequency stabilization

Figure 5.10 shows the estimated frequency noises on the sensitivity plot, when the stabilization system was activated. The frequency noises are calculated from Fig. 4.19 and the simple relationship between frequency noise and displacement noise, $\delta L = L\delta\nu/\nu$.

In a single measurement, the frequency noise becomes dominant above about 30 kHz, resulting in an increasing displacement noise. This is because of the insufficient gain of the frequency stabilization loop. By the differential measurement between the two cavities the noise decreases by a factor of 1/100 in that frequency range, becoming completely negligible and enabling us even to observe its noise floor at around mirror resonance (above 30 kHz)[12]. Also, the CMRR made a further safety margin below 1 kHz.

[10] According to Liu's theoretical calculation, the error should be much less than 1% in our case [15].

[11] We believe that the thermal linear expansion is dependent on the direction of the expansion in the crystal.

[12] Here, the subtracted frequency noise is estimated by multiplying estimated frequency stability, length conversion factor (L/ν), CMRR, and $1/\sqrt{2}$.

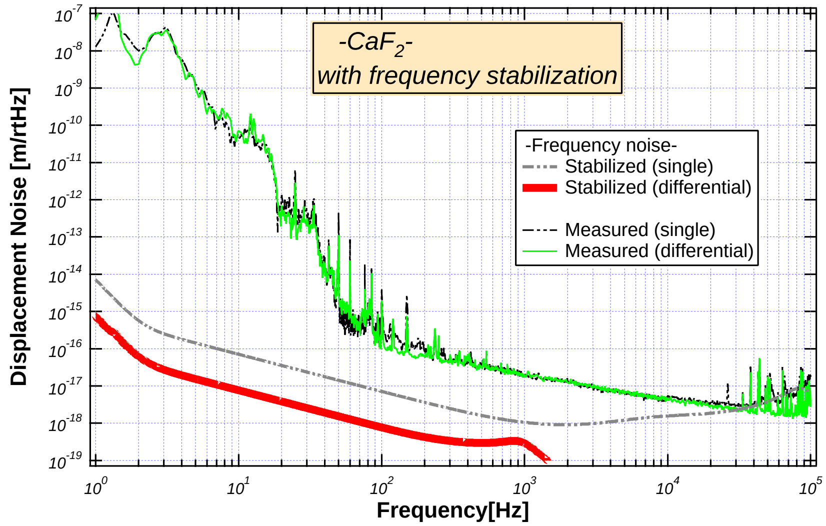

Figure 5.10: Effect of the frequency noise (with frequency stabilization); Stabilized frequency noise is the estimated from thick line in Fig.4.19). In the single measurement, the frequency noise limits the sensitivity in the high frequency range. By the differential measurement, the stabilized level is suppressed by CMRR and brought to a completely negligible level.

Therefore, at every frequency range, the frequency noise is definitely not the limiting factor of the measured displacement noise with the frequency stabilization and with the differential measurement.

Without frequency stabilization

Figure 5.11 shows estimated frequency noise on the sensitivity plot, when the stabilization system is not activated.

The freerun frequency noise mostly agreed with the sensitivity of a single cavity between 50 Hz and 100 kHz. It is obvious that the frequency noise is the noise source of the measurement[13]. By the differential measurement, the noise is reduced by the CMRR. Estimated frequency noise after the subtraction is also plotted on Fig.5.11. Over 1 kHz, the contribution becomes negligible compared to the measured displacement noise level. Below 1 kHz, because the CMRR was not so effective (typically 1/10), frequency noise can be found close below the measured noise[14].

[13]The frequency noise levels differed between the two experiments (Figs.5.3 and 5.8). This was because the frequency noise of the laser was actually changed.

[14]The CMRR would be easily improved by more precisely adjusting the two open-loop transfer functions. We did not emphasize the performance of the differential measurement at that frequency range because of successful operation with the frequency stabilization.

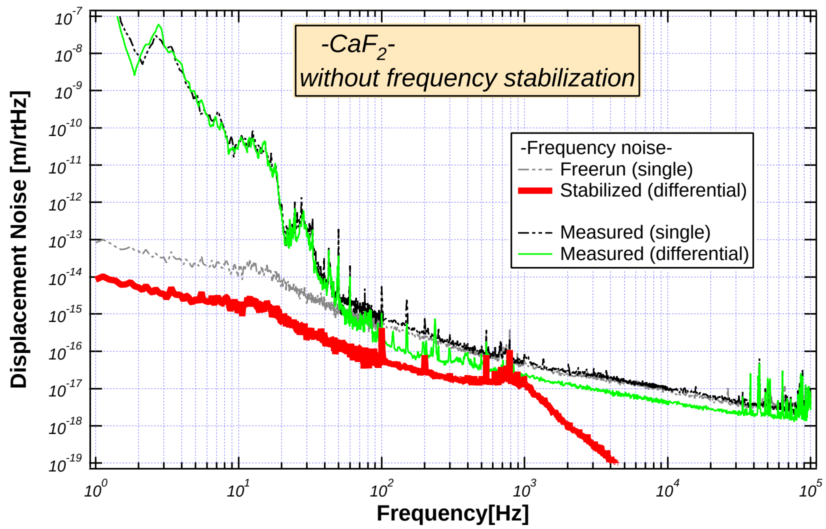

Figure 5.11: Effect of the frequency noise (without frequency stabilization); Freerun frequency noise is estimated by feedback signal of the stabilization loop. Without the subtraction, the frequency noise is the dominant noise source on the sensitivity above about 50 Hz. In the differential measurement, it is brought to be smaller than the measured displacement noise.

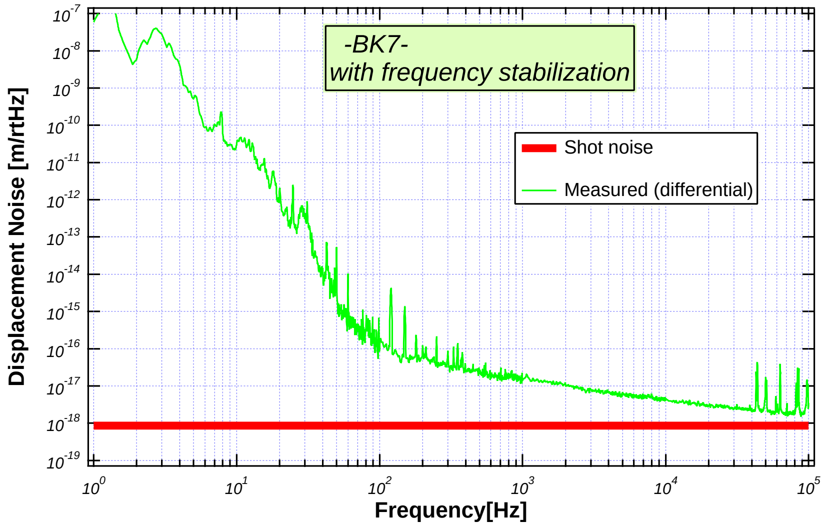

Figure 5.12: Effect of the shot noise.

Table 5.1: Shot noise level of each measurement (Unit: $[\mathrm{m}/\sqrt{\mathrm{Hz}}]$); differential shot noise is multiplied by $1/\sqrt{2}$ after summing up two cavities' noises.

Cavity material	Cavity A	Cavity B	Differential
BK7-BK7	8.71×10^{-19}	8.46×10^{-19}	8.58×10^{-19}
CaF_2-BK7	9.95×10^{-19}	1.08×10^{-18}	1.04×10^{-18}

5.3.2 Shot noise

Shot noise is one of the principal noises for the measurement using photo detection. In this experiment, the shot noise contributes a little on the measured displacement noise at high frequency range. Figure 5.12 shows the shot noise level on the sensitivity plot.

The shot noise was estimated as follows. As in Fig.4.24, we can regard the shot noise as the white displacement noise added before the photo-detector's conversion. The shot noise, δx_{shot}, is calculated from the DC photocurrent, I_{DC}, of the photo detector under operation, the properties of the photo detector[15], and the displacement-to-voltage conversion factor, D_{T}. Table 5.1 shows the calculated shot noise level in each cavity and each measurement. The typical shot noise level was 1×10^{-18} $\mathrm{m}/\sqrt{\mathrm{Hz}}$. It became close to the measured displacement noise above 40 kHz.

[15] Including the detector noise.

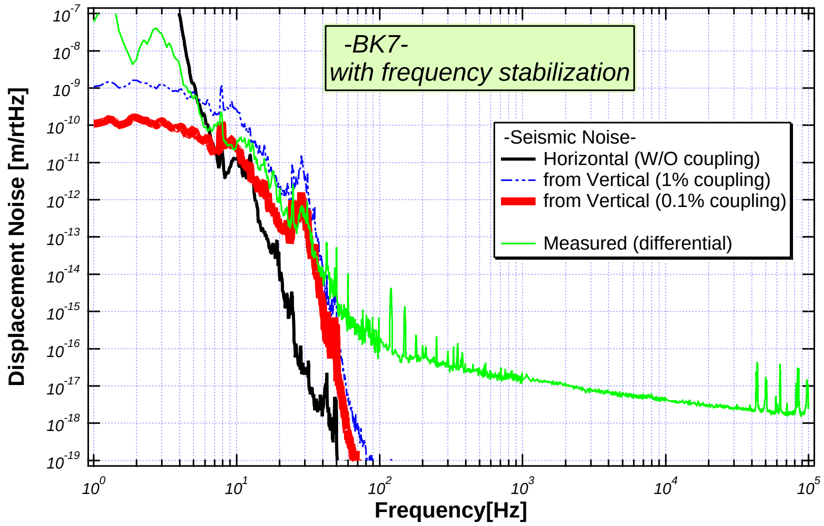

Figure 5.13: Effect of the seismic noise; The estimated seismic noises on Fig.4.10 were multiplied by $\sqrt{2}$ on this graph. We assumed two vertical-to-horizontal coupling factors, 0.1% and 1%.

5.3.3 Seismic noise

The seismic noise is one of the non-fundamental noises for the ground-based measurement. In this experiment also, the effect of seismic motion limits the displacement noise in a low frequency range.

On Fig.5.13, the estimated seismic noise level is shown with the sensitivity of the interferometer. The estimation is based on Fig.4.10. The estimated level was multiplied by $\sqrt{2}$ considering the possible incoherence of the seismic motion between the two mirrors in a cavity[16]. Between 5 Hz and 50 Hz, the estimated seismic noise spectrum with coupling[17] and the measured spectrum have essentially the same structure and noise level. The absolute levels are mostly overlapped, by assuming a coupling factor of 0.1%. Around 30 Hz, a peak appears – this is caused by a combination of vertical resonance of the stack and one of the suspensions (see also Figs. 4.7 and 4.9). Above 50 Hz, the seismic noise falls rapidly well below the measured displacement noise.

Below 5 Hz, the measured noise is smaller than the estimated level. We believe that in this frequency region the common mode rejection of the seismic noise is effectively working. Above about 5 Hz, the contribution from the vertical seismic motion, to which common mode rejection for seismic noise is not effective, starts to dominate.

[16] We are considering the worst case in which CMR of seismic motion is not working.

[17] From vertical to horizontal.

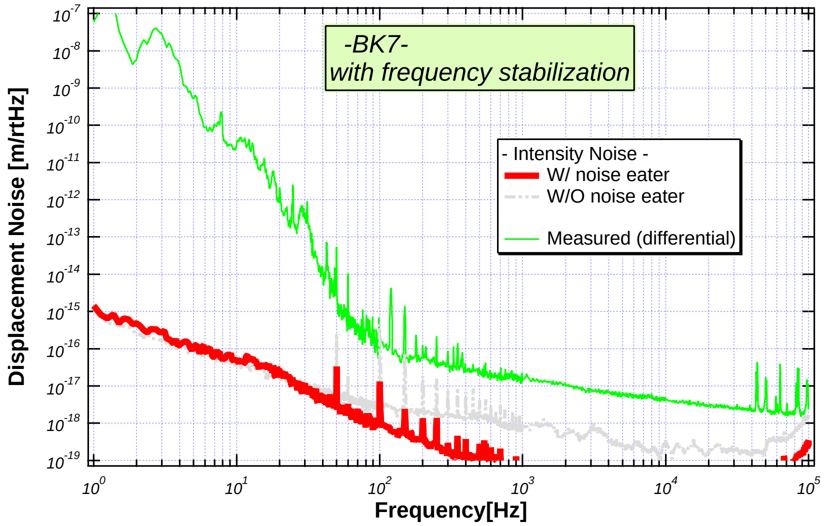

Figure 5.14: Effect of the intensity noise.

5.3.4 Intensity noise

The intensity noise of the laser source couples with the displacement noise though a residual RMS motion of mirror and an offset of the servo loop[18]. The effect is written as,

$$\delta x_{\rm int}(f) = \beta \frac{\delta P(f)}{P}, \tag{5.1}$$

where β is the coupling factor.

We measured the coupling factor β experimentally. A sinusoidal signal is applied on AOM to modulate the laser intensity, monitoring the sensitivity and the output of the photo-detector for intensity monitoring (PD2). The β was measured to be 4×10^{-13}[m] over most of the frequency range. By multiplying the relative intensity noise measured at PD2, Fig.4.14, and measured β, we estimate the effect of the intensity noise. Figure 5.14 shows the result[19]. The effect of intensity noise is smaller than the measured displacement noise by 1/10 to 1/100.

The open-loop gain at DC was of the order of 10^8, and the RMS motion of the mirror was roughly estimated to be of the order of $10^{-5} \sim 10^{-6}$ m without control[20]. Roughly speaking, the residual RMS under control could be of the order of $10^{-13} \sim 10^{-14}$ m, which could be of the same order as the measured β. Therefore, the intensity noise coupling is believed to be mainly from the residual RMS motion in our case.

[18] Possible other effect is the photo-thermal effect.

[19] For a simpler argument, we are showing the effect of the intensity noise for a single measurement. In reality, by the differential measurement, the effect is brought to a still smaller level.

[20] The uncontrolled cavity is observed to pass occasionally through its resonance.

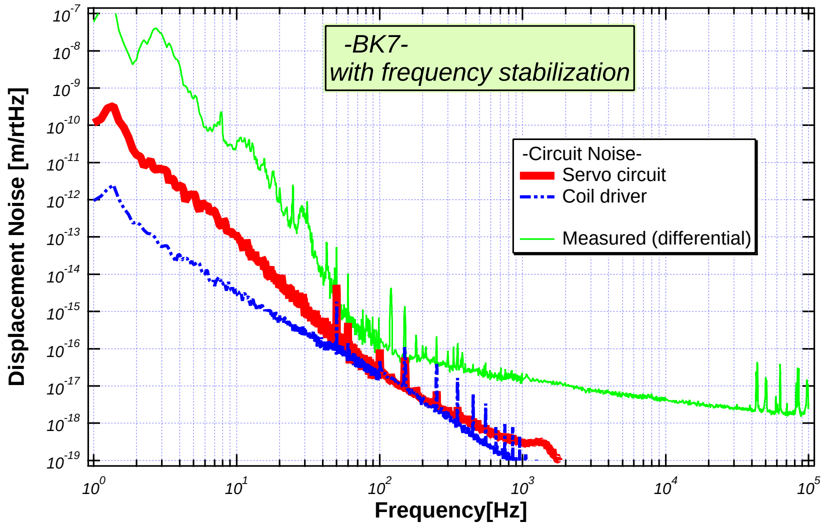

Figure 5.15: Effect of the circuit noise.

5.3.5 Electronics circuit noise

The electronics circuits within the control loop can contribute to the sensitivity of the interferometer. By measuring the circuit noises out of the loop, we confirmed that the circuit noises are negligible compared to the measured displacement noise except below about 100 Hz.

We consider two circuit noises[21]: the servo circuit noise (input equivalent noise: $\delta V_{\rm Circ}$ in Fig.4.24), and the coil-driver circuit noise ($\delta V_{\rm Driv}$).

The servo circuit noise appears in the displacement noise with a level of $\sim |G_{\rm OL}|\delta V_{\rm Circ}/D_{\rm T}$ within the bandwidth in the error signal conversion. Based on the measurement of the servo circuit noise, the thick solid line in Fig.5.15 was plotted. The circuit noise is still below the measured displacement noise. This was confirmed by the fact that the displacement noise converted from the feedback signal mostly agreed with the noise from the error signal.

The driver noise in the displacement noise spectrum is simply expressed as $|\alpha|\delta V_{\rm Driv}$. By measuring the output current noise of the driver, the input equivalent voltage noise $\delta V_{\rm Driv}$ was calculated and converted into displacement noise, considering the incoherence of the noises in the four coils[22]. The dotted line in Fig.5.15 is the result – the driver noise is also below the measured displacement noise over 100 Hz.

[21]In reality, these two can be measured and evaluated simultaneously by a single measurement.

[22]The four coils commonly push the mirror by four independent drivers. In that case, the measured noise $\delta V_{\rm Driv}$ in one of the coils is converted to the displacement noise by $|\alpha|\delta V_{\rm Driv}/2$.

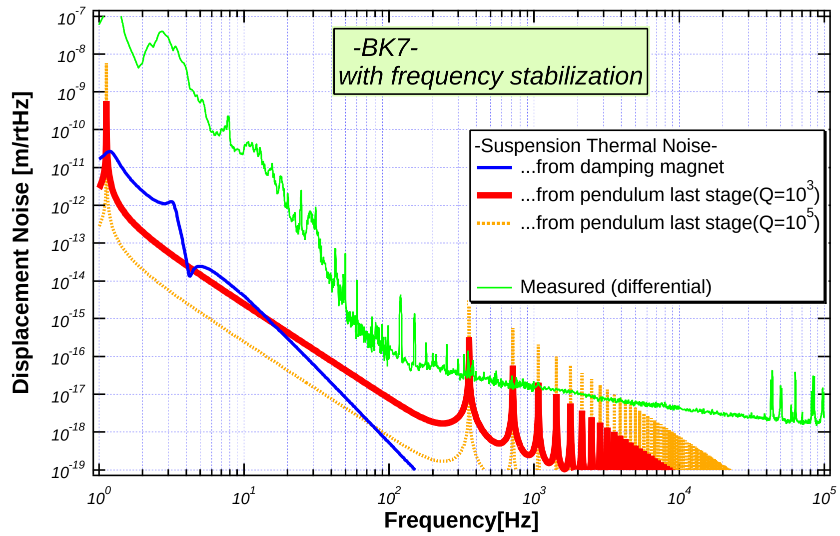

Figure 5.16: Effect of the suspension thermal noise; Two kinds of loss source in the suspension were considered: 1) loss due to damping magnet, and 2) loss due to the last stage of pendulum. For the latter, we assumed two pendulum quality factors, 10^3 and 10^5.

5.3.6 Suspension thermal noise

Suspension thermal noise is estimated not to contribute to the measured displacement spectrum.

Figure 5.16 shows the estimated thermal noise level of the suspension system. Two kinds of loss sources were considered. The first is the loss introduced by the damping magnet on the intermediate mass. It was estimated by calculating the imaginary part of the transfer function in the simulation model used for the design of the suspension[23]. Since the loss is viscous damping, the thermal noise decreases steeply with increasing frequency, and becomes negligible in our observation band.

The second is the loss in the last stage of the pendulum. It originates from the intrinsic loss of the wire and from the loss in its clamping points. The thermal noise level is drawn also on Fig.5.16, assuming a pendulum Q of 10^3 and 10^5 and by using a modal expansion[24]. The floor level is much smaller than measured displacement noise; therefore, it is not observable in this system. The peaks of the violin modes have not been observed clearly. This might be because of the low line-width resolution used to

[23]The dip at 4 Hz is caused by the translation mode of the damping magnet. At that frequency, the relative motion between the damping magnet and the intermediate mass nulls, resulting in a dip of thermal noise.

[24]We believe that these Qs are the lower and upper limits of the actual Q, based on our experience on similar setups for measuring the pendulum Q. Also, we assumed that violin mode Q is one half of the pendulum Q.

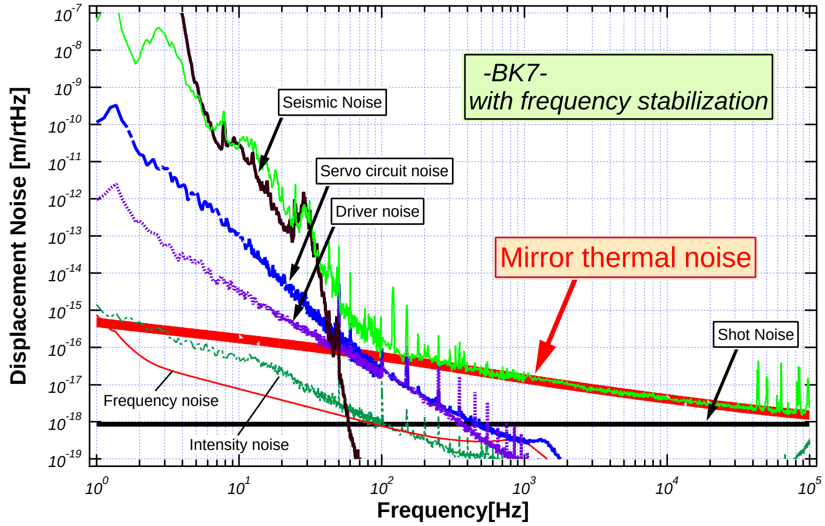

Figure 5.17: Summary of the noise sources (BK7-BK7 cavity); Mirror thermal noise is the unique explanation for the measured displacement noise at the most of the frequency range.

measure the spectrum.

5.3.7 Noise sources summary

Here, we summarize the evaluated noise sources of the interferometer. The noise sources were as follows (see Fig.5.17):

- 1 Hz to ∼50 Hz: The seismic noise dominates the sensitivity. The coupling from the vertical seismic noise is the limiting factor above 5 Hz.
- 50 Hz to ∼100 Hz: The circuit noises contribute to the displacement noise.
- 100 Hz to ∼50 kHz: Mirror thermal noises dominate the displacement sensitivity. Only when the frequency stabilization is not activated, does the frequency noise dominate. The effect is brought to a completely negligible level by its stabilization and by the differential measurement.
- 50 kHz to 100 kHz: While the shot noise contributes a little to the measured displacement noise, the mirror thermal noise is still greater. This noise floor was uncovered by the differential measurement that suppressed by a factor of about 100 additional frequency noise caused by insufficient gain of the servo loop.

5.4 Summary of this section

We performed the experiment to measure two kinds of mirror thermal noises, the Brownian noise and the thermoelastic noise, using BK7 and CaF_2, respectively. The system worked as designed. Best sensitivity was $\sim 2\times10^{-18}$ m/$\sqrt{\text{Hz}}$ at the edge of the observation band ($\sim$ 100 kHz)[25]. The high sensitivity enabled us to observe displacement noise off resonance and also around the mirror resonance[26]. With the frequency stabilization, the differential signal was mostly equivalent to the non-differential signal. Even without the frequency stabilization, the differential measurement gave the same results. These ensure that what we measured was non-correlated displacement noise between the two cavities. The measured results were dependent on the mirror substrates. Also, the possible noise sources, except for the mirror thermal noise, were evaluated to be smaller than the measured displacement noise. Furthermore, the measured results agreed well with the corresponding theories on the mirror thermal noise in a wide frequency range within a calculation error of 20%. Therefore, considering collectively these facts, the measured displacement noises are regarded as mirror thermal noises.

The measured noises had the following features:

- BK7 cavity: In this measurement, the most dominant thermal noise was the Brownian noise from the BK7 substrate. The measured off-resonance displacement noise agreed with the calculation by the direct approach. It showed the typical Brownian thermal noise envelope, $f^{-1/2}$. This does not contradict with the fact that the measured intrinsic loss of BK7 was structural.

- CaF_2 cavity: In this measurement, the most dominant thermal noise was the thermoelastic noise from the CaF_2 substrate. Measured noise followed the exact solution of the thermoelastic noise with the cutoff frequency, which has $f^{-1/4}$ to f^{-1} frequency dependence. The adiabatic limit approximation did not agree with the measurement.

This is the first experiment that clearly observed the mirror thermal noise over wide frequency range. The theories used here include the Fluctuation-Dissipation Theorem (FDT). The validity of the FDT in mechanical systems had been checked only in simple mechanics typically within one octave. Therefore, this experiment confirmed the validity of the FDT in mechanical system at the widest frequency range in some sense.

[25] As far as the author knows, few other interferometers had achieved this sensitivity at the frequency region (from 10 kHz to 100 kHz).

[26] Details are shown in the next chapter.

In the following chapter, we discuss the thermal noise around the resonance and the developed interferometer itself.

Chapter 6

Discussion

In this chapter, we discuss the thermal noise around the mirror resonances and the developed interferometer.

First, we will show that the measured result in the BK7 cavity around resonances agreed well with the theories including thermal noise peaks, as long as the measured quality factors were not degraded by the external loss. Second, we will identify the many peaks in the CaF_2 cavity around the resonances.

Then, we discuss the developed interferometer as a test bench for the gravitational wave detector and the way to reduce possible noise further. Calculating the thermal noise of the other substrates, we will show the possible experiments using this system.

6.1 On-resonance thermal noise

In this section, we discuss the on-resonance (40 kHz to 100 kHz) thermal noise in each cavity including the measured peaks. In both of the cavities, the dominant thermal noise was Brownian noise, whose floor was disclosed by the differential measurement between two cavities.

6.1.1 On-resonance thermal noise in BK7 cavity

We discuss the thermal noise at around the mirror resonance in the BK7 cavity. We could treat the thermal noise near resonances with the same way as in the thermal noise of cantilevers [26] or that of resonant-type detectors. Our results also support that the modal expansion with the measured quality factor is invalid with presence of the inhomogeneous loss, as demonstrated in that types of mechanics.

Table 6.1: Measured quality factors of BK7 cavity mirrors; The data were taken without touching and reloading the mirrors after the measurement of the displacement noise. Calc.: calculated resonant frequency by the finite element method. Cav.A Q: quality factor of cavity-A mirror, Cav.B Q: quality factor of cavity-B mirror.

Mode		Flat mirror			Concave mirror		
No.	Parity	Calc.[Hz]	Cav.A Q	Cav.B Q	Calc.[Hz]	Cav.A Q	CavB. Q
1st	even	43525	4100	3600	42976	2500	3200
2nd	odd	44207	3100	3900	43866	4400	4400
3rd	even	50757	2800	2800	50174	1900	150
4th	even	59416	4400	4200	59220	4400	4300
5th	odd	62996	4000	4100	63568	2500	3800
6th	odd	81719	1200	1200	81829	630	2800
7th	even	83575	1400	2600	85361	2100	3300
8th	even	97225	2600	600	97332	930	1000
9th	odd	98483	2000	2100	98646	960	1400

Table 6.2: Effective mass m_n of each longitudinal mode (unit: [kg]).

Mode No.	Flat mirror	Concave mirror
1st	0.196	0.430
2nd	0.355	0.154
3rd	0.403	0.359
4th	8.222	6.201
5th	0.103	0.158
6th	0.204	0.589
7th	0.0396	0.0559
8th	0.0899	0.0914
9th	0.304	0.252

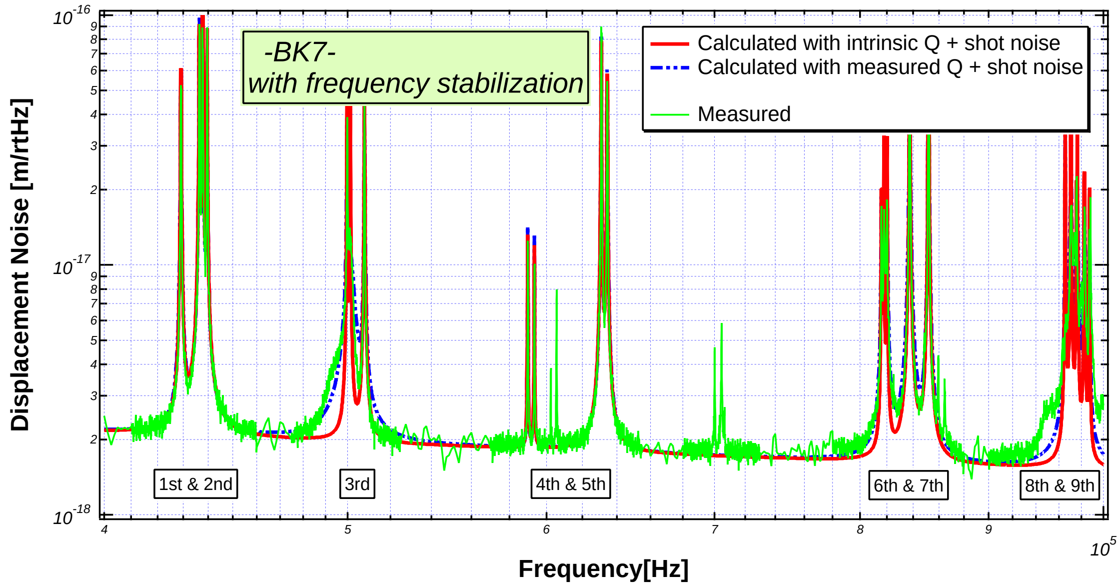

Figure 6.1: Displacement spectrum of BK7 cavity at high frequency range; This graph is magnifying Figure 5.1 at the edge of the observation band (40 kHz∼100 kHz).

Agreement with the theory

Figure 6.1 shows the measured results in BK7 cavity between 40 kHz and 100 kHz with the theoretical levels. Two theoretical thermal noise levels are shown in Fig.6.1: calculation by intrinsic quality factor and calculation by measured quality factors. We used the modal expansion to calculate the thermal noise contribution from the resonances[1]. We calculated the noise floor level using static limits[2]. Table 6.1 shows the measured quality factor in the four mirrors. There are nine longitudinal modes for each mirror (Each modal shape is shown in Fig.A.4). As long as the measured quality factors are high (typically over 2500), the two theoretical lines and the measured results agree well.

Invalidity of the modal expansion

Around the resonances with low quality factors, which were limited by the external loss, we can see that the modal expansion with the measured Qs (dotted line) does not give accurate thermal noise estimation[3]. Figures 6.2 and 6.3 show the measured

[1]The modal expansion with intrinsic quality factor is equivalent to the direct approach in our case. See also Fig.A.6.

[2]We have numerically confirmed that their use is also relevant for our small beam radius case even around the resonance. This discussion is shown in Appendix A.

[3]Intrinsic Q determines the lower limit of the thermal noise. On the other hand, measured Qs determine the peak value of the thermal noise.

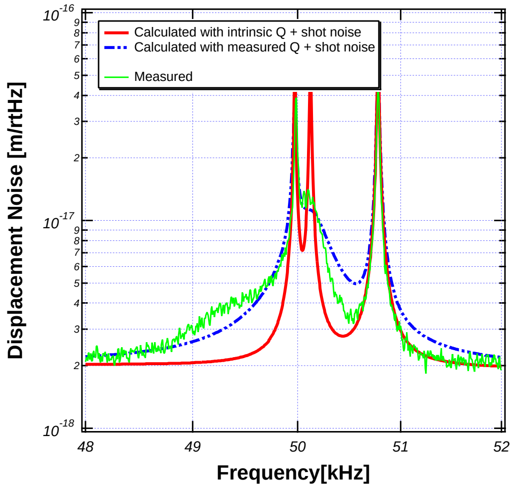

Figure 6.2: Displacement spectrum around 3rd resonances.

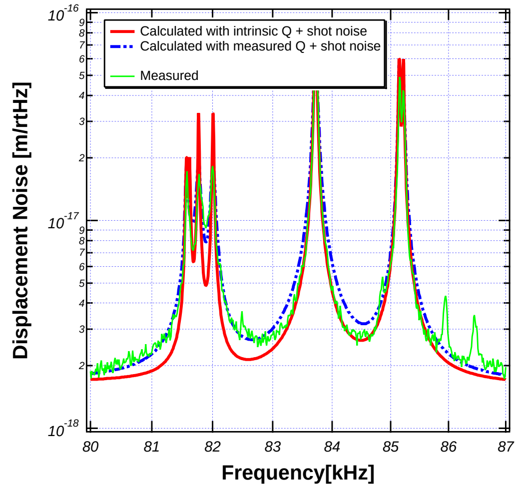

Figure 6.3: Displacement spectrum around 6th and 7th resonances.

displacement noise and the corresponding two theoretical lines around 3rd resonances, and 6th-7th resonances, respectively. We can see a different structure between the modal expansion and the measured results. Similar effects have been observed in a blade spring or drum, proving invalidity of the modal expansion with the measured quality factor [42]. Our result using the real mirror also shows that the traditional mode expansion does not work in presence of external inhomogeneous loss.

The probable source of inhomogeneous additional loss, which resulted in the discrepancy from the calculations, is believed to be from the wires rounding around the mirrors in this case. Further direct measurements and analysis using our numerical method (shown in Appendix A) may reveal the origin and the mechanism of the additional losses. By using smaller loss mirrors and by reducing the loss due to wires, we will be able to observe the noise floor dominated by the coating loss, even around the resonance (discussed later in this chapter). In that case, typical structure of thermal noise due to the coupling of the modes caused by the coating could be directly observed. It will be possible to investigate very minutely the coating-induced thermal noise, which is a serious problem for future detectors, at every frequency range, by using our system and our calculation method.

Resonance contribution at low frequency range

Figure 6.4 shows the possible contribution from the first 9 modes at all frequency ranges. Two theoretical contributions (calculation by intrinsic quality factor and calculation by measured quality factors) differ by 44% off-resonance. At off resonance, the direct approach with intrinsic loss should agree with the former theoretical line if

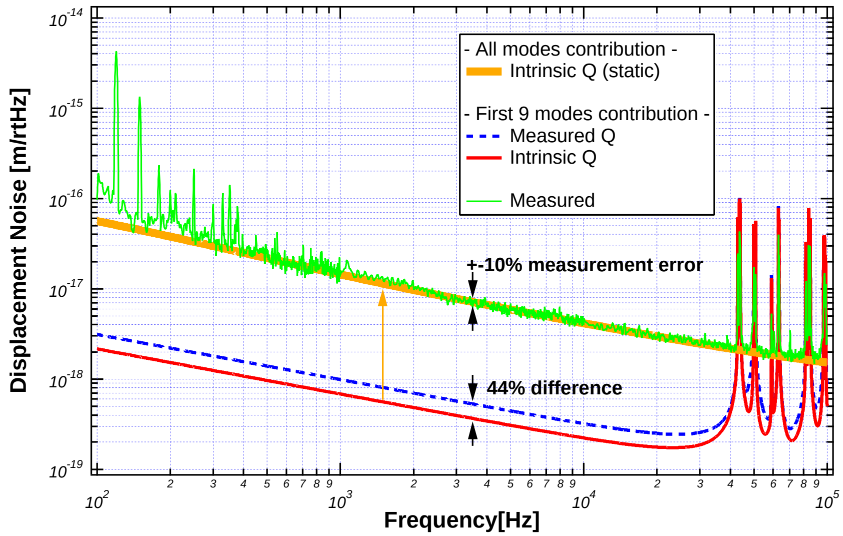

Figure 6.4: Contribution from the first nine modes on the off-resonance thermal noise.

the much number of modes were added up[4]. Therefore, if we relied on the traditional mode expansion with the measured Q, we might have overestimated the off-resonance thermal noise by ∼40%.

Our result, which agreed with the direct approach at off-resonance and disagreed with the traditional mode expansion on resonance, realize the importance of the intrinsic loss of the substrate and the unimportance of the measured loss at the resonances for the estimation of the off-resonance thermal noise. From this viewpoint, the technique to measure the intrinsic loss of bulk substrate (Appendix B) is playing an extremely important role to reduce the off-resonance thermal noise.

6.1.2 On-resonance thermal noise in CaF_2 cavity

In this section, we discuss the measured thermal noise in the CaF_2 cavity near resonance.

Figure 6.5 shows the measured results and theoretical contributions from the thermal noises and from the shot noise between 40 kHz and 100 kHz. The floor level is determined by the shot noise and the Brownian noise from the BK7 mirror. Broad peaks are the thermal noise peaks of the BK7 mirror. The noise floor and the peak level agree well with those of theoretical predictions[5]. The excessive number of other

[4] Levin [13] and Bondu [43] showed that the static direct approach coincided the modal expansion at low frequency assuming several cases. We also have confirmed dynamically the fact in a case of relatively large beam radius, in which the modal expansion converges within available computer resources.

[5] This was because the Qs of the BK7 mirrors were recovered by reloading them.

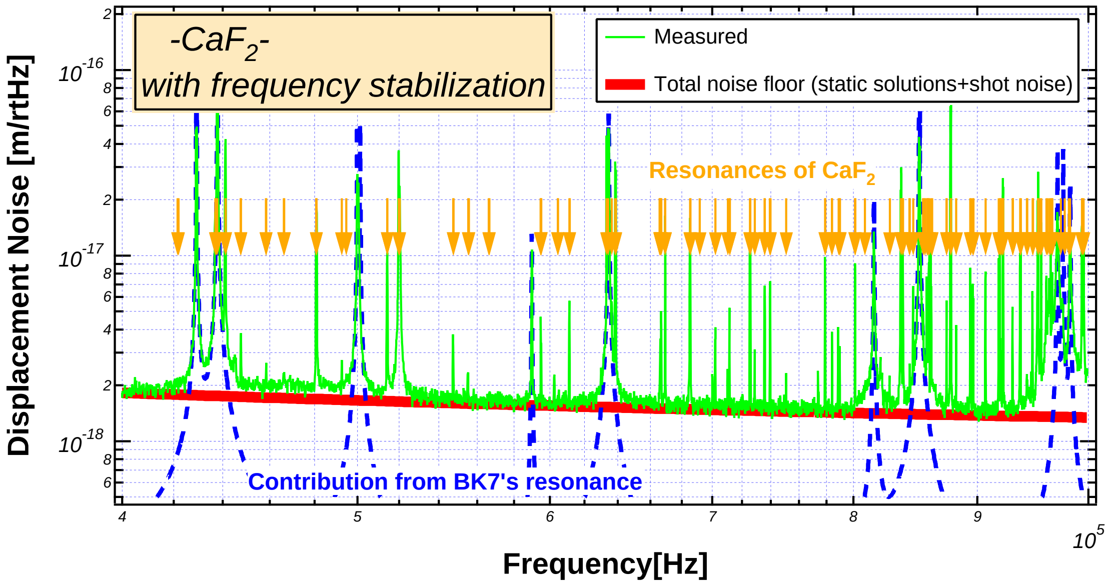

Figure 6.5: Displacement spectrum of CaF_2-BK7 cavity at high frequency range.

narrow peaks is from the resonance of CaF_2 mirror. In Fig.6.5, we show the experimentally found resonances using arrows[6].

The many numbers of peaks originate in the special feature of the modal shape in crystalline material. The cylindrical crystalline sample had longitudinal displacement at the cylindrical center even in the non-longitudinal modes [24]. The measured quality factors of some of the detected resonances were of the order of 10^6, maximum being 2×10^6. Though these modes have large effective mass, high quality factors made the thermal noise peaks visible.

Minute theoretical calculation of thermoelastic noise including resonances and anisotropy of substrate has not been done. We are planning to do them and to compare them with the measured results as we have done for the Brownian noise. Our system and such calculations, if established, will be useful for an evaluation of thermal noise including resonances in future detectors, because they are planned to use larger mirrors that have lower resonant frequency that will be close to the observation band.

6.2 Possibility of future experiment

We will, finally, discuss the possible measurements in future, using the developed interferometer discussed above.

[6]Unfortunately, since the direction of crystal axis was unknown in our sample, we could not identify the modal shape of them. By now, we have confirmed that the cylindrical axis is not in parallel with [001] or [111] by our calculation.

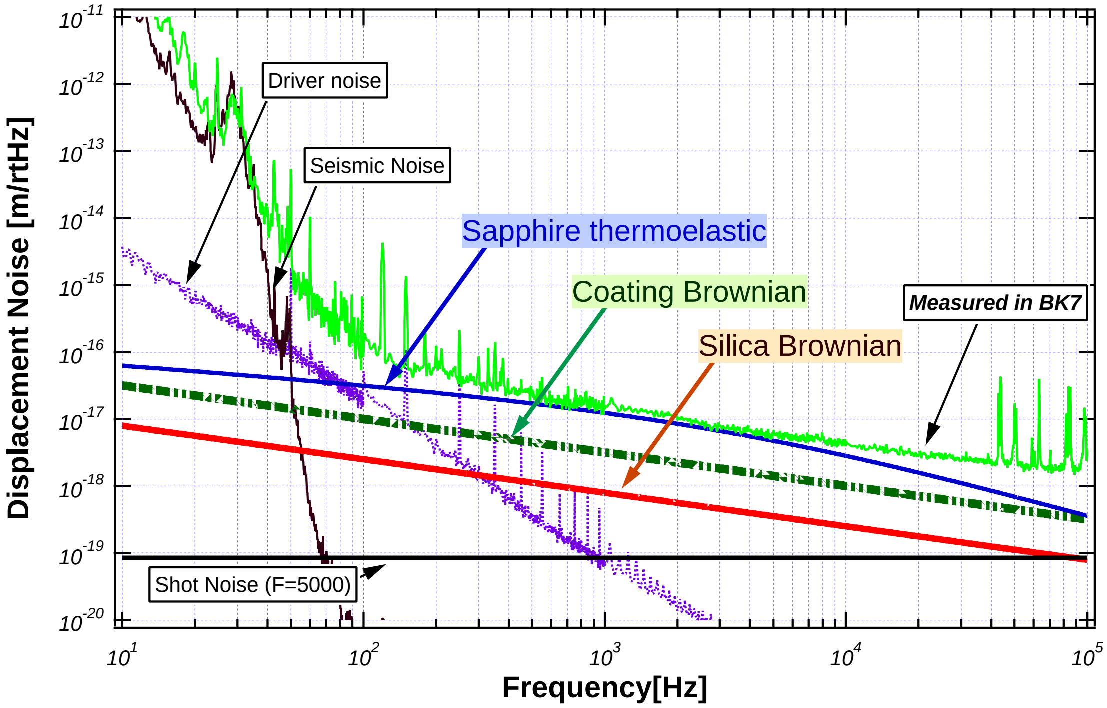

Figure 6.6: Possibility of future measurement; Possible noise sources in the future are plotted with a measured spectrum. We assumed coating loss factor $\phi_{\mathrm{coat}} d$ of 10^{-9}[m], and fused silica quality factor of 10^6.

Our interferometer has potential to measure smaller levels of mirror thermal noise at wide frequency range including off-resonance and on-resonance regions. If needed, the noise sources can be suppressed further in the following manner:

- Laser frequency noise: By improving CMRR of the differential measurement between the two cavities, which is easily done by adjusting two open-loop gains, the frequency noise can be suppressed by a factor of 10 at least. Option of longer Fabry-Perot cavity for frequency stabilization is also available.

- Laser intensity noise: By using external amplitude stabilization system, and by adjusting the offset of the servo system, the intensity noise can be easily suppressed further.

- Servo circuit noise: By taking a displacement spectrum at the feedback signal, the servo circuit noise can be suppressed to negligible level easily.

- Shot noise: Our choice of finesse in this experiment was relatively low (500). By increasing the finesse, the shot noise level is proportionally suppressed. For example, finesse of 5000 would be reasonable.

- Seismic noise: By using the low frequency vibration isolation system that is developed in our laboratory, the seismic noise should be suppressed efficiently.

- Driver circuit noise: When the seismic noise is suppressed by above-mentioned manner, the driver circuit noise will be also suppressed by reducing the coupling strength of the coil-magnet actuators. Lower noise driver circuit is also available.

- Other noise sources: Beam jitter or the other common mode noise can be suppressed by the differential measurement. Our system is a simplest design setup at this stage. We have number of options of installing other components, such as a mode cleaner, temperature stabilization system for reference cavity and other optics, alignment control system, and so on to suppress the noise further.

As an example, Fig.6.6 shows possible measurements. The first is the thermoelastic noise in sapphire, which is being considered for the substrate in future gravitational wave detectors [64, 65]. Since sapphire should have a very similar level of thermoelastic noise to that of calcium fluoride, it should certainly be measured if it is available. Another possibility is Brownian noise in fused silica, which is the most common substrate in the detectors, and it has high quality factor. In the fused-silica case, the thermal noise will be limited by the Brownian noise from the coating, if the current predictions and the measurements are accurate in our current setup with small beam radius. We are also able to check the effects of the coating losses, which recently were discovered to be important. This experiment is already underway. By changing beam radius, Brownian noise from fused silica substrates can be observed. According to our measurement, some fused silica showed lower loss at lower frequency (Section B.3.1). A weaker frequency dependence of Brownian noise than $f^{-1/2}$ caused by the decreasing loss is, if observed directly, extremely important. Direct thermal noise measurements in various kinds of fused silica have great significance for next generation detectors.

Except for the short cavity length, our measurement system is designed to be mostly identical with the real gravitational wave detectors. This system will be used as a test bench for the detectors by measuring the off-resonance and the on-resonance thermal noise directly.

Chapter 7

Conclusion

The mirror thermal noise is one of the most significant issues to be investigated in the interferometric gravitational wave detectors, because it directly limits the sensitivity in the observation band. Although the mirror thermal noise is theoretically well studied and indirectly investigated through the measurement of mechanical loss, it had not been clearly measured earlier because of its small amplitude. No one knew whether the developed theoretical and indirect experimental approach was correct or not. Verification by direct measurement was the most important work for the study of the mirror thermal noise.

We thus developed an interferometer to measure the mirror thermal noise directly. Our goal was to measure two kinds of mirror thermal noise — the Brownian noise and the thermoelastic noise — using two kinds of mirror substrate, BK7 and CaF_2. By designing each component of the system carefully, and by reducing the other noise sources, we first measured both of the mirror thermal noises and proved the validity of the theoretical models, which include the fluctuation-dissipation theorem, between 100 Hz and 100 kHz. The wide frequency band enabled us to observe Brownian thermal noise off resonance and near resonance of BK7 substrate. It also enabled us to observe the change of the frequency dependence of thermoelastic noise from a CaF_2 substrate.

Our results on BK7 strongly suggest that the off-resonance Brownian noise level is mainly determined by the intrinsic loss of the substrate, because the noise level agreed with a theoretical calculation by the direct approach with the intrinsic loss of the substrate. The modal expansion with measured quality factor did not give an accurate thermal noise estimate off resonance or near resonances. Our measurement using a real mirror also showed that the traditional mode expansion does not work with the existence of external inhomogeneous loss.

Our interferometer showed high sensitivity: $\sim 10^{-18}\ \mathrm{m}/\sqrt{\mathrm{Hz}}$ at 100 kHz. Except for the shot noise, the mirror thermal noise was the unique factor limiting the sensitivity above 100 Hz. Because our choice of finesse was relatively low ($\sim$500), the shot noise can be easily reduced by increasing finesse, if we want. Other noise sources are estimated to be smaller, by about a factor of 10 at least, over the most of the frequency range. Therefore, the system still has enough capability to detect a smaller level of mirror thermal noise in a wide frequency range. Since we designed the interferometer to have essentially identical configuration with the gravitational wave detectors, except for its cavity length, the total system will work as a test bench for the detector. For example, thermal noise due to optical coating will be directly evaluated in our system.

Along with the direct thermal noise measurement of the cavity, we have developed powerful methods to evaluate Brownian thermal noises theoretically and experimentally:

- **Numerical calculation of thermal noise (Appendix A):** We directly solved the equation of motion to calculate thermal noise numerically and dynamically using a finite element method. The method is quite general. It can be applied for any shape of the system, any distribution of loss, any frequency dependence of loss, and at any frequencies, without requiring any theoretical calculations other than the fluctuation-dissipation theorem.
- **Direct measurement of intrinsic mechanical loss (Appendix B):** We have developed a nodal support system to measure directly the intrinsic loss of the material, which is one of the most significant quantities for estimating the thermal noise off resonance. The nodal support precludes the support loss, which had dominated the measured loss in earlier conventional suspension systems. This technique was applied to evaluate many low loss samples enabling us to obtain meaningful results for gravitational wave detectors.

All of the developed systems and techniques will play an important role in investigating the mirror thermal noise directly, indirectly, and mutually. We believe that our direct measurement of mirror thermal noise has a significant meaning for the direct detection of the gravitational waves.

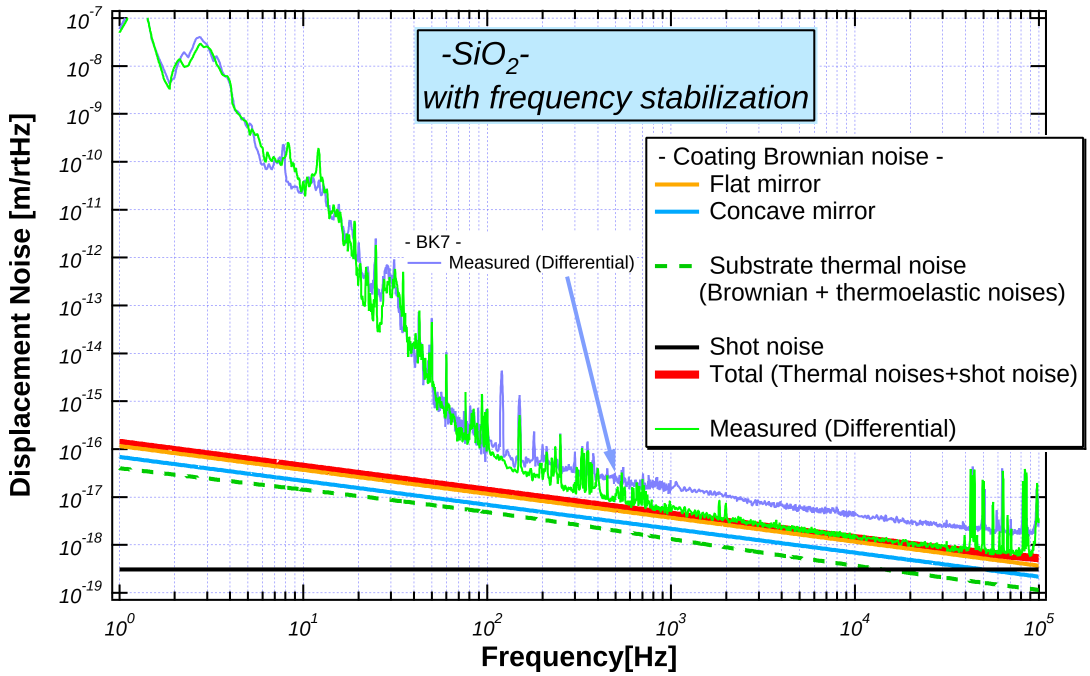

Figure 7.1: Displacement spectrum of SiO_2 cavity with the frequency stabilization.

Additional note on Dec. 6th, 2003:

After the submission of this thesis, we replaced the cavity mirrors with ones made of fused silica, and repeated the measurements. Figure 7.1 shows measured displacement spectrum in the fused silica cavity with the frequency stabilization using the reference cavity. The displacement spectrum coincided with Eq.(3.29) assuming d of 3.5 μm and ϕ_{coat} of 4×10^{-4}, which were most plausible in our case. Thus, the measured spectrum is believed to be from the coating Brownian noise. The measured spectrum was smaller by about one order of magnitude than ones measured in previous two cavity sets between about 200 Hz and 100 kHz. This supports that what we measured in those measurements originated in the thermal fluctuations in mirrors[1].

We also have expanded the numerical calculation method of thermal noise that is mentioned in Appendix A. When this thesis was submitted, the calculation was limited to Brownian noise only. It has been applied to wider cases, such as thermoelastic noise and correlated thermal noise.

[1] These results were accepted for publication in Physical Review Letters.

Appendix A

Numerical calculation of thermal noise

In this appendix, we show our method, named numerical dynamic approach, to calculate the thermal noise in the mechanics[1]. Our method is much more practical and easier than analytic calculations. Also, it covers, all of the three-dimensional mechanics, loss distribution, weight function of displacements, anisotropic materials, and the entire frequency range in principle.

A.1 Concept of numerical dynamic approach

The concept of our method is very simple: the equation of motion of the system is *numerically* solved and then FDT is applied. We used a Finite Element Method (FEM) to numerically solve the equation of motion. Actual calculation process is as follows:

1. Construction of FEM model: We define an elastic body which is properly meshed into elements in a FEM program[2]. And then a force that has a weight function is applied on the point at which thermal noise is going to be calculated.

2. Solution: we solve the equation of motion numerically at a required frequency. The required output is the imaginary part of the transfer function or dissipated energy in the system[3]. The loss can be in anywhere in the system, or can have any frequency dependence.

[1]Thermal noise discussed here is Brownian noise. Numerical calculation of thermoelastic noise is now under development.

[2]Commercial FEM program ANSYS was used.

[3]In this case, dissipated energy was calculated by multiplying output stored energy in each element and the corresponding loss angle for the element, after we solved the system without loss. Therefore, the result obtained in the lossless system, breaks down exactly at the resonance, and when the loss does not satisfy $\phi \ll 1$.

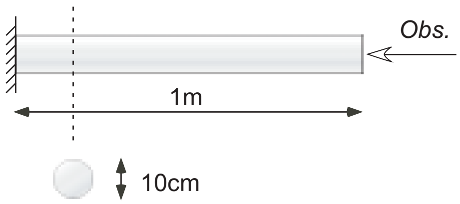

Figure A.1: Illustration of example 1; A one-dimensional bar with a length of 1 m, and a diameter of 10 cm is fixed on a wall at one of the ends. We observe a thermal fluctuation of the other end.

3. Application of FDT: Eqs.(3.6) or (3.9) was applied to convert the results into the thermal noise.

Only by this simplified scheme, we can calculate Brownian noise in any kind of dimensional system, including a mirror. The following section shows two examples: one-dimensional elastic bar, and the mirror used in the experiment.

A.2 Example 1: One-dimensional elastic bar

As one of the simplest examples, imagine the one-dimensional elastic bar made of Aluminum. The length of the bar is 1 m, and the diameter is 10 cm. One end of it is fixed to a wall, and the other is free. We calculate the thermal motion of the free end. Figure A.1 shows the schematic viewgraph for this problem.

The FEM model is constructed of 30 beam elements. For comparison, we solve this problem using the modal expansion method[4] and the transfer matrix method[5]. We assume two kinds of loss distribution: homogeneous and inhomogeneous.

A.2.1 Homogeneous loss

We define a loss that is distributed homogeneously within a volume. The loss angle is assumed to be $\phi(f) = 1/1000$ at 1 kHz. The viscous damping and the structural damping are assumed. Figure A.2 shows the result[6]. The FEM gives the same result as the transfer matrix method and the modal expansion method, even around resonance.

A.2.2 Inhomogeneous loss

We assume that the loss $\phi(f) = 30/4000$, is concentrated over 4/30 of the length from the free end[7]. Figure A.3 shows the result of the calculated thermal noise. Although

[4]Modal expansion method can be applied for homogeneous loss case.

[5]Yamamoto has reported that the other direct approaches (Levin's and Nakagawa's) resulted in an identical result as of transfer matrix method, at least at low frequency range [42].

[6]Here we calculated $\mathrm{Im}[H(\omega)]$ directly by introducing a loss from the beginning.

[7]Therefore, total average loss in the bar is 1/1000, which is same with homogeneous example.

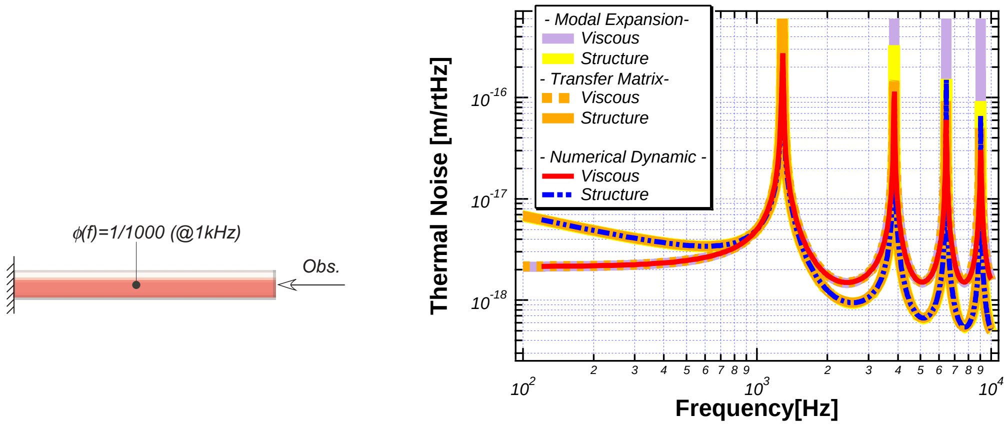

Figure A.2: Thermal noise of homogeneous loss case.

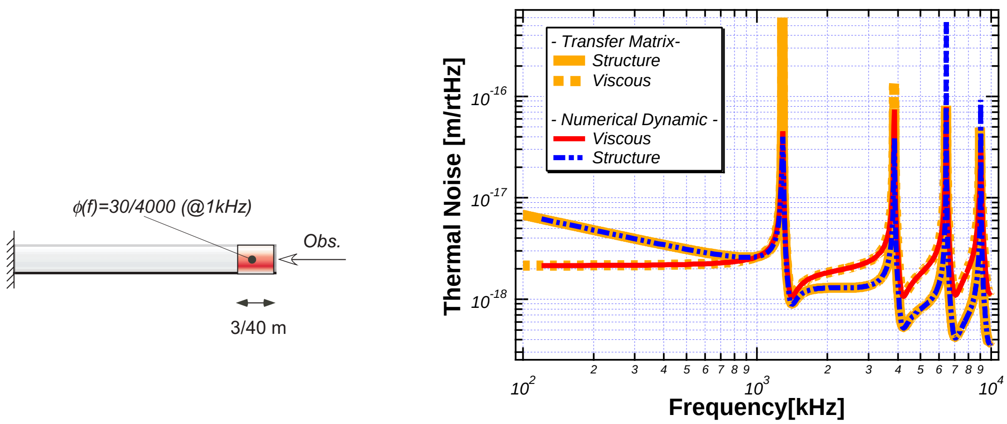

Figure A.3: Thermal noise of inhomogeneous loss case.

the peak values are not accurate[8], FEM results agree well with the transfer matrix results. The frequency dependence of thermal noise with several dips is a characteristic feature in an inhomogeneously distributed loss. This can be interpreted as a result of couplings between the internal modes [42].

A.3 Example 2: Mirror used in the experiment

Next example is the Brownian thermal noise of the mirror used in the experiment. The shape of the mirror is illustrated in Fig.4.4. Beam radii on the flat mirror and the concave mirror are 48.9 μm and 84.8 μm, respectively. The material is assumed

[8]We are showing the results obtained by $\mathrm{Im}[H(\omega)]$ for viscous damping, and W_{diss} for structural damping here. As discussed in the footnote on the previous page, use of W_{diss} results in an infinite peak value in our case. However, this is just a technical problem.

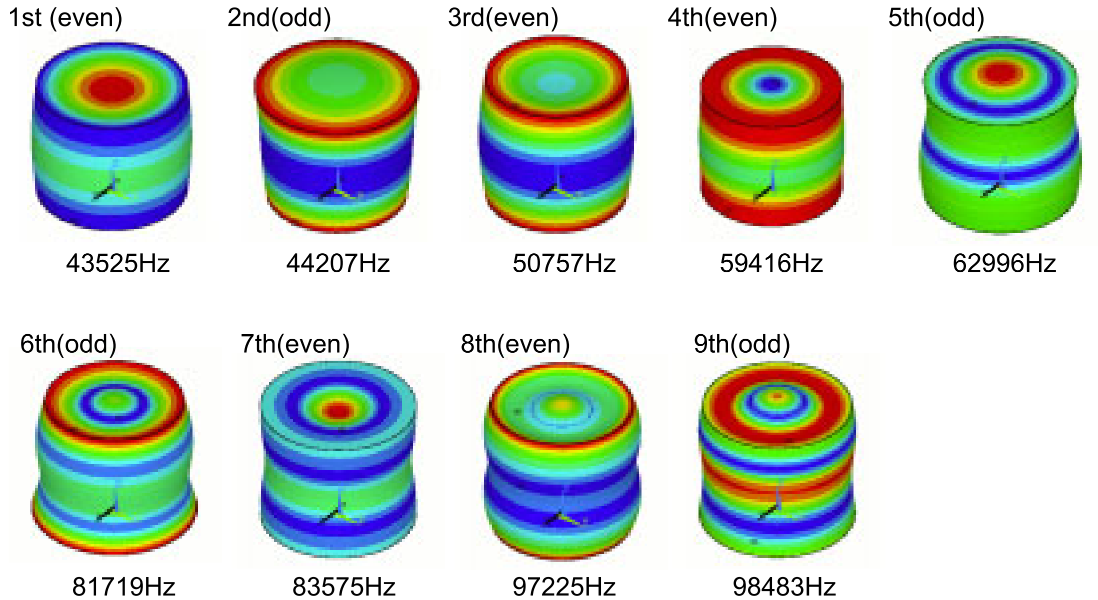

Figure A.4: Modal shape of the flat mirror.

to be the optical glass, BK7, mechanical properties of which are summarized in Table 4.2. We solve the system below 100 kHz including its resonances. In this frequency range, each mirror has nine longitudinal modes. Figure A.4 shows the longitudinal modes of the flat mirror.

In the following, we show the results obtained by the numerical dynamic approach with three cases of loss: homogeneous, loss in front surface (coating), loss in rear edge (magnet).

A.3.1 Homogeneous loss

We assumed the substrate has a constant loss of $\phi = 1/3600$. Figure A.5 shows the results obtained by the numerical dynamic approach and the static approach, Eq.(3.26), for infinite half space. In a flat mirror, the relative error for floor thermal noise level was less than 0.1%. The small beam radius made the difference very small. In a concave mirror, the relative error was 0.3%. We believe that the larger error is caused by a "hole" in the concave mirror, because the static solution is for a perfect flat volume.

Figure A.6 magnifies total thermal noise in the high frequency range. Contribution from each resonance[9], calculated by the effective mass, is also shown. A summation

[9] In this case, the modal expansion did not work well to calculate thermal noise off resonance. This is because of the small beam radius, which made it difficult to calculate every mode that contributes to the off-resonance. The number of summations in Eq.(3.19) becomes too big, making it virtually

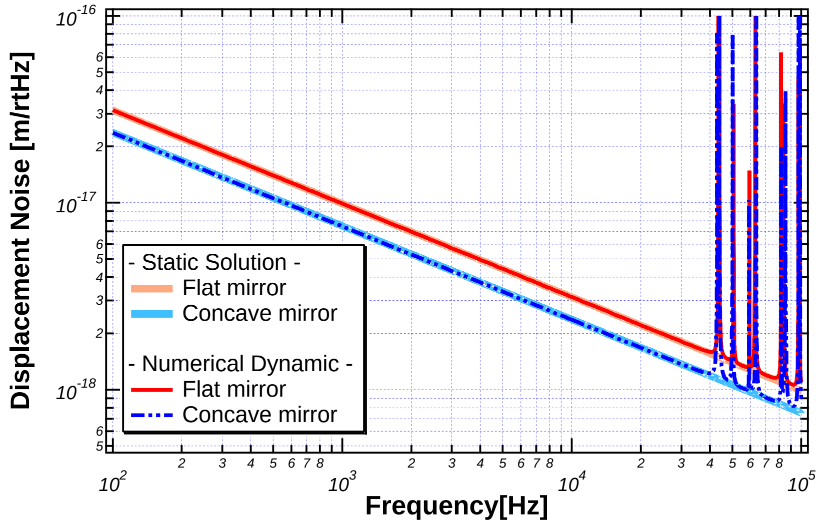

Figure A.5: Calculated thermal noise of the flat and the concave mirror (homogeneous loss); Static limits for infinite half space are shown as well.

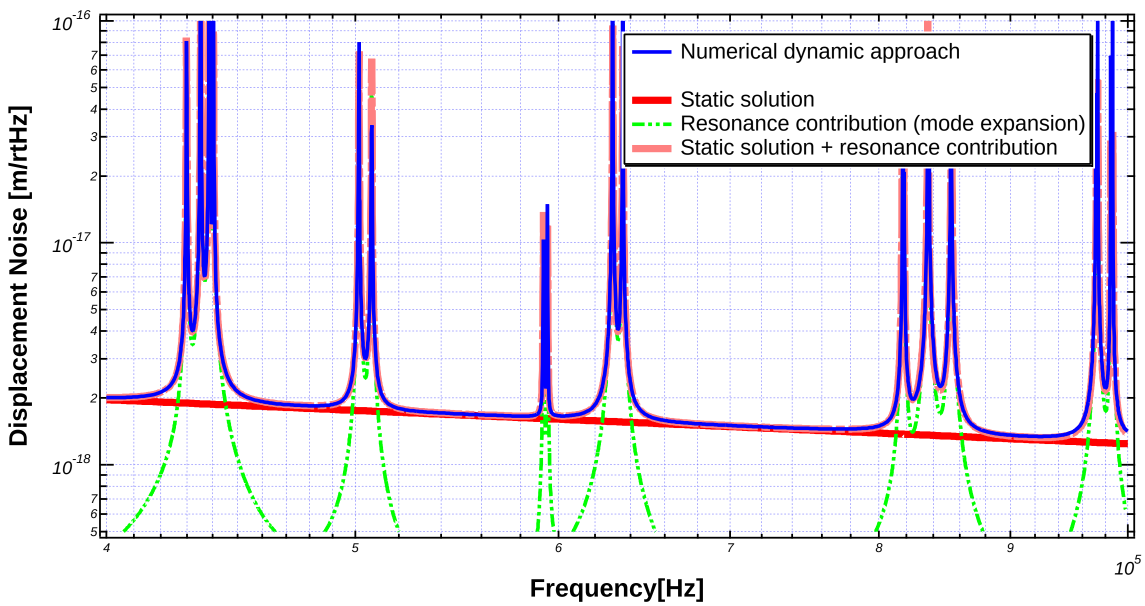

Figure A.6: Calculated thermal noise using numerical dynamic approach at high frequency range; Static solution, contributions from resonances calculated by effective mass, and their summation are shown.

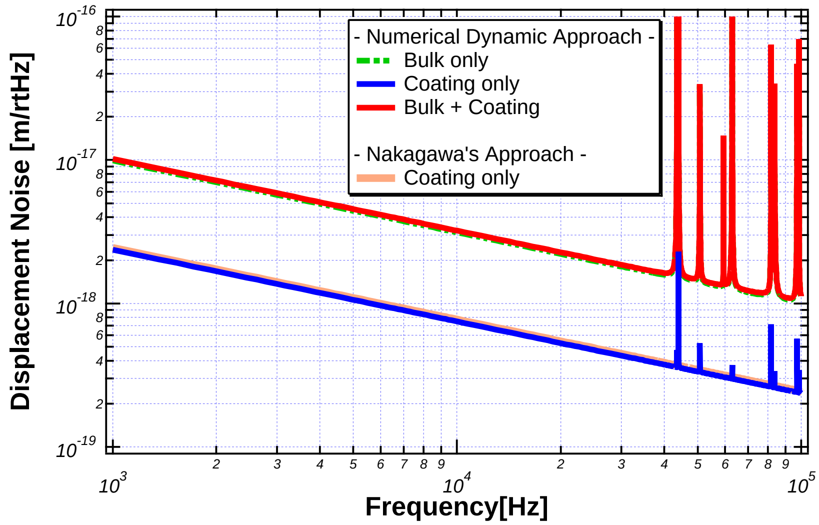

Figure A.7: Thermal noise from the optical coating on the flat mirror; Calculated thermal noise from the bulk substrate, the coating, and their total are shown. Static solution by Nakagawa [44] is also shown.

of static solution and resonance contributions agrees very well with the numerical results. This happens because the small beam radius pulls up the thermal noise floor and makes the contribution from the first nine modes smaller at this frequency range.

A.3.2 Inhomogeneous loss (coating)

We introduced a loss layer in the surface imitating an optical coating on the mirror. Figure A.7 shows the results on the flat mirror, assuming a coating loss parameter $\phi_{\text{coat}} d$ of 10^{-9} [m]. For comparison, a theoretically calculated line, Eq.(3.29), is also shown. The relative error was 3%. This is because of two approximations: 1) To obtain Eq.(3.29), beam radius is regarded as much larger than the thickness of the loss layer[10]. In this case the ratio is $\sim 1/5$. 2) We calculated the loss in the surface from the elastic energy density of the surface elements. The accuracy of our calculation can be easily improved further.

A.3.3 Inhomogeneous loss (magnet)

To imitate a magnet, which is usually attached on a mirror in a GW detector, a loss is applied on the rear edge of the mirror. We assume the loss angle of the magnet as 0.36

impossible to calculate the off-resonance thermal noise.

[10] Also, the authors of [44] assumed that the coating loss is much larger than that of the substrate. In this case, however, these two are of the same order.

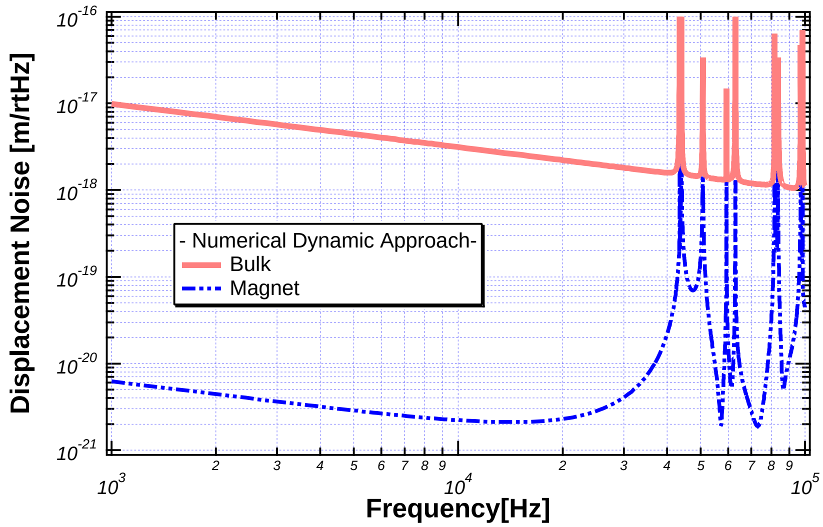

Figure A.8: Thermal noise from the magnet on the flat mirror.

(structural), and loss area as 1.5 mm × 1.5 mm. Four magnets are attached on the edge of the rear surface. Figure A.8 shows the result. In this case, the magnet-loss-induced thermal noise is much smaller than that of the bulk loss by 10^3. Our dynamic result shows the typical structure of thermal noise with dips around resonance.

It should be noted that the noise floor level of thermal noise is not changed much by the magnet, if the bulk loss is smaller by about 10^6. In that case, the quality factor of the resonance is effectively degraded by the magnet. Therefore, the decrease in quality factor by the magnet does not change the off-resonance thermal noise in usual cases. Most significant loss is intrinsic bulk loss of the substrate and other losses around the beam spot.

Appendix B

Measurement of intrinsic mechanical loss

In this appendix, we describe the measurement of intrinsic mechanical loss using a nodal support system that we invented. In the system, the samples are supported at the node of their vibration mode. This arrangement enables us to measure their internal loss directly, excluding the support system loss. The technique was applied for measuring the intrinsic loss of the mirror substrates used in the main experiment of this thesis. Most of these measurements are reported in [23, 24, 55].

B.1 Principle

Investigating the mechanical loss ϕ of low-loss samples has been an important, but difficult, subject especially in the field of detecting gravitational-waves. The difficulties arise from the existence of the loss due to the support for the measurement. The mechanical loss is usually evaluated by measuring the quality factor, Q, which is the inverse of the losses at their resonances. In the measurement of the quality factor, the measured loss, $Q_{\rm meas}^{-1}$, is composed of the internal loss of the sample, $Q_{\rm int}^{-1}$, which originates in the sample, itself, and the external loss, $Q_{\rm ext}^{-1}$:

$$Q_{\rm meas}^{-1} = Q_{\rm int}^{-1} + Q_{\rm ext}^{-1}. \tag{B.1}$$

The internal loss of a sample, $Q_{\rm int}^{-1}$, is determined by the intrinsic loss of the material, $Q_{\rm mat}^{-1}$, and by the loss due to surface roughness [17], $Q_{\rm surf}^{-1}$, and by possible further contributions:

$$Q_{\rm int}^{-1} = Q_{\rm mat}^{-1} + Q_{\rm surf}^{-1} + \cdots\ . \tag{B.2}$$

On the other hand, the external loss, $Q_{\rm ext}^{-1}$, is dominated by the loss due to the support system, $Q_{\rm sup}^{-1}$, if we can neglect other external losses, such as residual gas damping:

$$Q_{\rm ext}^{-1} = Q_{\rm sup}^{-1} + \cdots\ . \tag{B.3}$$

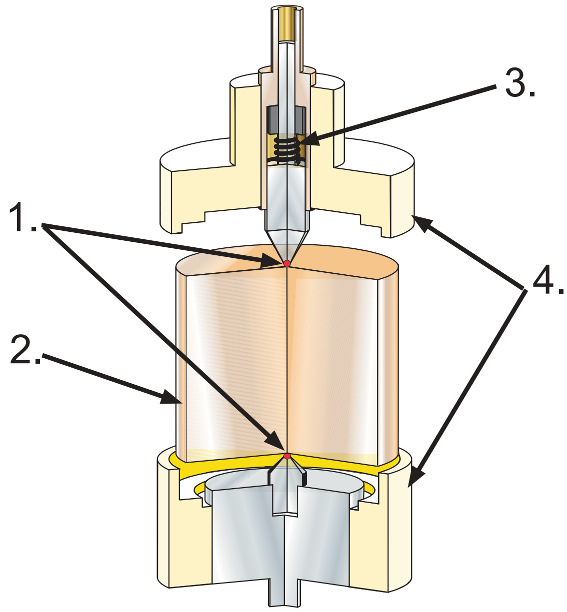

Figure B.1: Cross-section of our nodal support system; 1) ruby balls (diameter 2 mm), 2) sample, 3) spring to provide weak force (about 1N), 4) adjusters.

When the internal loss of the sample is very small, the measured quality factors can actually be dominated by the loss due to the support. The principle of our experiment to measure the internal loss directly is to use a nodal support with point contacts strategically located to eliminate any loss due to the support for a number of modes.

The measured samples are cylindrical. The modal shapes of a cylindrical isotropic sample have been well studied semi-analytically and experimentally by Hutchinson [38] and McMahon [39]. All of the modes with order[1] $n > 1$ have no displacements along the axis of the cylinder, including in particular the centers of the flat surfaces. If we support a sample at the center of the flat surface by the point contacts [76], there is no coupling between the sample and the support system for the higher order modes ($n > 1$). We have designed a support system that contacts the cylindrical sample only at the centers of the flat surfaces to realize a nodal support.

B.2 Setup

Figure B.1 shows our support system. The sample is supported between two balls having a diameter of 2 mm. The balls are made of ruby, which has a similar composition and structure to the well-known low-loss material sapphire. A ring-down method was used to measure the quality factor. We excited the sample by electrostatic or piezoelectric actuators at one of the resonant frequencies. The decay of the vibration was measured by using a Michelson interferometer.

[1]The circumferential order n $(= 0, 1, 2...)$ defines the number of nodal lines with respect to the rotation around the cylindrical axis.

B.3 Results

In this section, we show the measured results using this system and discuss the measured quality factors. We measured the following samples:

- Isotropic sample – fused silica
- Anisotropic samples – silicon and sapphire
- Substrates used in main experiment – BK7 and CaF_2
- Coating loss

In the following, we introduce the measured sample's details, measured quality factors, and its interpretation in each sample.

B.3.1 Isotropic sample – fused silica

Measured samples

Fused silica is used for many optical applications because of its extremely low optical losses between ultraviolet and infrared. Since fused silica has low mechanical loss, it has been regarded as the best among many candidate materials to minimize the thermal noise limits. Therefore, it has been installed in all current GW detectors as mirror substrates.

We prepared 13 samples of fused silica from 4 companies: Heraeus [77], Corning [78], Tosoh [79], and Shin-etsu [80]. Table B.1 gives the properties of each sample. Some of them have actually been adopted as mirror substrates in current GW detectors. Their trade names are as follows:

- Heraeus : Suprasil-1, -2, -311, -312 and Herasil-1
- Corning : 7980-0A, -0F, and -5F
- Tosoh : ED-A, -C and ES
- Shin-etsu : Suprasil P-10 and P-30

Most of the samples are TYPE III fused silica, which is synthetically made from silicon chloride by an oxygen-hydrogen flame. Heraeus Herasil-1 is TYPE II fused silica, which is made from natural quartz powder using flame fusion. The Tosoh ED series is TYPE V (or VI) fused silica, which is made by the VAD (Vapor-phase Axial Deposition) method. Most of the samples were cylinders with 6-cm height and 7-cm diameter. Only Shin-etsu samples had a 10-cm diameter. All surfaces of all the samples were commercially polished by the same company to the same level.

Table B.1: Properties of fused silica. †1 Type; †2 Bubble grade (high,0; low,8); †3 Striae grade (high,A; low,C); †4 Homogeneity of refraction index(Δn, $\times 10^{-6}$); †5 Direction of homogeneity for the specified value (3D, all three directions; 1D, specific one direction).*: NM, near mirror; EM, end mirror; BS, beam splitter; RM, recycling mirror. L, LIGO. V, VIRGO. G, GEO. T, TAMA. **: LIGO, VIRGO, and GEO use custom made 311 and 312 called SV grade that include less OH than our commercial grade samples.

Company	Trade name	†1	†2	†3	†4	†5	OH(ppm)	Used in project
Heraeus	Suprasil 1	III	0	A	5	3D	1000	G(NM*,EM)
	Suprasil 2	III	0	A	5	1D	1000	G(RM)
	Suprasil 311**	III	0	A	3	3D	200	L,V,G(BS)
	Suprasil 312**	III	0	A	4	1D	200	L(NM),V(NM,RM)
	Herasil 1	II	0	A	4	1D	150	V(EM)
Corning	7980 0A	III	0	A	1	1D	800-1000	L(EM,RM)
	7980 0F	III	0	A	5	1D	800-1000	
	7980 5F	III	5	A	5	1D	800-1000	
Tosoh	ES	III	-	A	-	1D	1300	
	ED-A	VAD	-	A	-	3D	100	
	ED-C	VAD	-	A	-	3D	1	
Shin-etsu	Suprasil P-10	III	0	A	2	3D	1200	T
	Suprasil P-30	III	0	B-C	20	3D	1200	

Some of the samples were annealed in a vacuum electric furnace to observe the annealing effect on the Qs. The Heraeus Suprasil-2, 311, Herasil-1, and Corning 7980-5F were annealed at 900°C. Also, Heraeus Suprasil-312 and Corning 7980-0F were annealed at 980°C. The 5F sample was annealed at this temperature once again. In every case, the samples were annealed for 24 hours, and cooled down in the furnace within 24 hours.

Measured quality factors

Table B.2 summarizes the results of the measured Qs. The Qs of the higher order modes were similar to each other. As an example, Fig.B.2 shows the results obtained in Heraeus Herasil-1, Suprasil-2, and Sin-etu P-10. Figure B.3 shows change in quality factors in Heraeus Suprasil-312, and Corning 7980-5F by the annealing. Higher Q samples showed a frequency-dependent Qs, which degrade at high frequency. The annealing process improved the Qs of every sample. After the annealing, the maximum Q in one sample reached 4.3×10^7 – to the best of our knowledge, this is the highest measure on a fused-silica bulk substrate. By examining Table B.1 and Table B.2, the following facts are discovered:

Table B.2: Results summary. *: The measured loss was fitted by a power law versus frequency. Fitting error is shown together.

Company	Trade name	Maximum Q	Q after annealing	Power low exponents* (after anneal)
Heraeus	Suprasil 1	1.1×10^7		0.2 ± 0.1
	Suprasil 2	1.3×10^7	2.1×10^7(900°C)	$0.2 \pm 0.1(0.4 \pm 0.1)$
	Suprasil 311	3.4×10^7	4.1×10^7(900°C)	$1.2 \pm 0.1(1.0 \pm 0.1)$
	Suprasil 312	3.4×10^7	4.3×10^7(980°C)	$0.8 \pm 0.2(0.9 \pm 0.1)$
	Herasil 1	7.2×10^5	9.7×10^5(900°C)	$0.0 \pm 0.0(0.0 \pm 0.0)$
Corning	7980 0A	1.1×10^7		0.4 ± 0.0
	7980 0F	1.1×10^7	2.1×10^7(980°C)	$0.3 \pm 0.0(0.6 \pm 0.1)$
	7980 5F	1.0×10^7	2.1×10^7(900°C)	$0.3 \pm 0.0(0.5 \pm 0.1)$
			3.3×10^7(980°C)	(0.7 ± 0.0)
Tosoh	ES	4.6×10^6		0.2 ± 0.0
	ED-A	1.9×10^7		0.7 ± 0.1
	ED-C	8.8×10^6		0.6 ± 0.2
Shin-etsu	Suprasil P-10	3.0×10^6		0.0 ± 0.0
	Suprasil P-30	1.0×10^6		0.0 ± 0.0

- The measured loss of many of the fused silica is constant across a wide frequency range. This is the clear observation of structure damping in low loss material.
- Higher Q samples tend to show a stronger frequency dependence, namely a decrease in the Qs at higher frequency.
- TYPE-III fused silica tends to show higher Qs if the OH content is less. However, this relationship does not hold with the other types of fused silica.
- Qs are not affected by direction of high homogeneity. (Suprasil-1 and 2, Suprasil-311 and 312)
- Neither bubble grade nor homogeneity of the refraction index correlates with Qs. (7980-0A, 0F, and 5F)
- Q may be degraded by poor striae grade. (Suprasil P-30)
- The annealing process improved the Qs of every sample. The degree of the improvement was dependent on the samples.

Discussion

As discussed before, the measured quality factors are determined by the internal loss of the sample Q_{int}^{-1} and by the loss due to the support system Q_{sup}^{-1}. Using the same

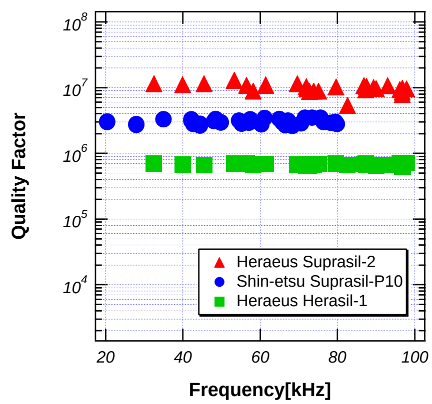

Figure B.2: Quality factors of various kinds of fused silica.

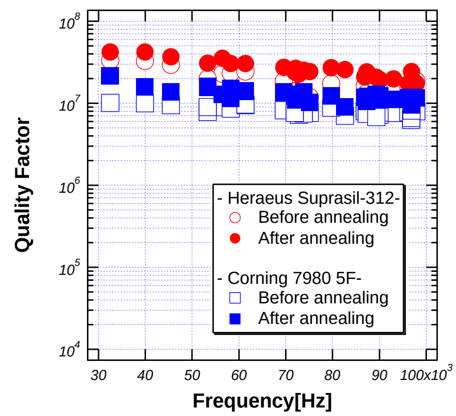

Figure B.3: Effect of annealing for fused silica quality factor.

support system, we measured a quality factor of 1×10^8 for a silicon sample (next result) in a mode with no displacement at the center. Therefore, the loss due to our support system is considered to be smaller than 10^{-8}. To estimate exactly the effect of the finite offset between the center and the contact point, we have to take into consideration the fact that each mode has a characteristic displacement amplitude around the center. In reality, the measured quality factors were uniform against frequency independent from each modal shape. This could not happen if the finite displacement at the center was the limiting factor of the measured quality factor. Therefore, the measured quality factors are believed to reflect the internal loss of the sample, $Q_{\rm int}^{-1}$.

We evaluated the contribution from the surface loss, $Q_{\rm surf}^{-1}$ within the internal loss, $Q_{\rm int}^{-1}$. The surface loss should contribute to the internal loss depending on stored strain energy:

$$\frac{1}{Q_{\rm meas}} \sim \frac{1}{Q_{\rm mat}} + \phi_{\rm surf}\, h \frac{\int_S \epsilon^2(\vec{r})dS}{\int_V \epsilon^2(\vec{r})dV}. \tag{B.4}$$

Here, $\phi_{\rm surf}$ is the loss factor of the surface, h is its depth, and $\epsilon(\vec{r})$ is the strain at the position $\vec{r}$. Integrations are done over the surface, S, and inside the whole body, V. The integration term, which we could exactly calculate, is strongly dependent on each modal shape – assuming a given surface loss, it results in a scatter of quality factors around a main trend. However, in reality, the measured values were not found to be correlated to the modal shape. We can thus conclude that the measured loss was dominated by the intrinsic loss of each material, and not by the surface loss. The details of the argument are shown in [23, 24, 55].

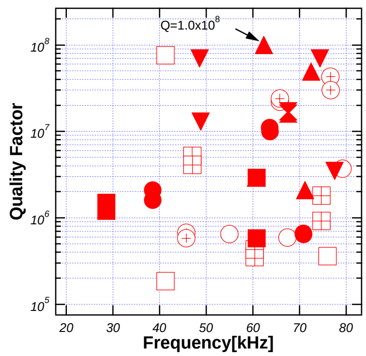

Figure B.4: Quality factors of silicon.

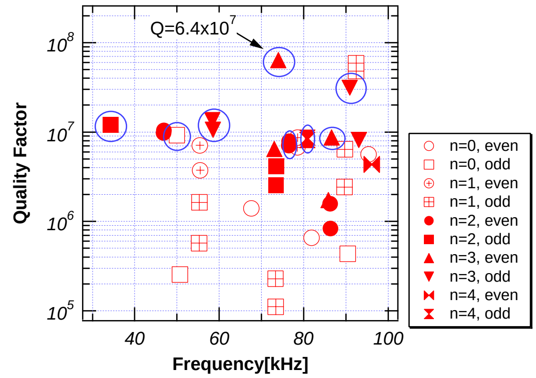

Figure B.5: Quality factors of sapphire.

B.3.2 Anisotropic samples – silicon and sapphire

Measured samples

Certain crystalline anisotropic materials are well-known for their low mechanical losses. We measured anisotropic samples made of silicon and sapphire. They were adopted as test mass materials for resonant-bar gravitational-wave detectors [17, 81], because the achievable sensitivity is inversely proportional to the mechanical loss ϕ of the test mass [82]. Also, they are candidate materials for mirrors in advanced interferometric gravitational-wave detectors [18, 64, 65, 83].

Our samples were of cylindrical shape with a diameter of 10 cm and a thickness of 6 cm. All of the surfaces were polished, but their quality of the polishing two samples differed. Both samples were single crystals. The cylindrical axis of the silicon sample was parallel to the (111)-direction of its crystal system, and that of the sapphire sample (HEMLITE grade, Crystal Systems Corp.) was parallel to the c-axis. Hence, the cylindrical axes of these two samples were three-fold axes of their elastic constants.

Measured quality factors

We calculated the resonant frequencies of silicon and sapphire using a finite element method with high accuracy (error $\sim$0.5%), and identified all of the resonances from their measured resonant frequencies. Figure B.4 shows the Qs of each mode of the silicon sample. The highest value was 1.0×10^8 for order $n = 3$, the parity even mode (62.346 kHz). The maximum Q is the highest measure for single-crystal silicon at room temperature to the best of our knowledge. Figure B.5 shows the measured Qs of the sapphire sample. The highest Q was 6.4×10^7 for order $n = 3$, the parity even mode (73.977 kHz).

Discussion

Figures B.4 and B.5 show significant differences from Fig.B.2. That is, the quality factors are much more widely distributed for crystals even for higher order modes. The reason is that all of the modes except for torsional modes and a half of the $n = 3$ modes had finite displacements at the centers of the flat surfaces at which the samples were supported. We found positive correlations between the measured losses and the calculated displacements. By this correlation analysis, from Fig.B.5, we could extract the modes, which have such small displacements that their quality factor is not expected to be affected by the support loss. After that, by using Eq.(B.4), the hypothesis of the existence of the surface loss on our sapphire sample was tested. We found positive correlations between the measured loss and the stored energy at the surface. The fitted result gave the surface loss of $\phi_{\rm surf} h = 1.3 \times 10^{-9}$ [m]. These details are shown in [24].

B.3.3 Substrates used in main experiment – BK7 and CaF_2

Measured samples

We also measured the substrate materials used in the main experiment of this thesis: BK7 and Calcium Fluoride (CaF_2). The samples for the intrinsic Q measurement were from the same company with the same trade names as those of the mirror substrate. BK7 was from OHARA corp. (exact trade name: S-BSL7), and CaF_2 was from Oyou-Koken. They were also cylindrical samples with 6-cm height and 7-cm diameter. All of the surfaces of the samples were polished, but not coated. Unfortunately, the direction of the crystal axis of the CaF_2 sample with respect to the cylindrical axis was unknown.

Measured quality factors

Figure B.6 shows the measured quality factors for BK7 (S-BSL7). The quality factor was much lower than the others, but mostly constant in all the measured frequency band. The quality factor was 3600±200. Some higher order modes showed excess loss. It was identified as the contribution from lower order modes which were close to the higher order modes, and had very low quality factor because of the support loss.

Figure B.7 shows the quality factors of CaF_2. The maximum quality factor was $3{\times}10^6$. Because, the directions of crystal axis were unknown, we could not calculate its modal shape and resonant frequency numerically – this prevented us from identifying the measured modes. We plotted all of the found resonances with their quality factors in Fig.B.7. Also, if the crystal axis is not symmetric with respect to the cylindrical axis, all of the modes have displacements at the support point as discussed in the

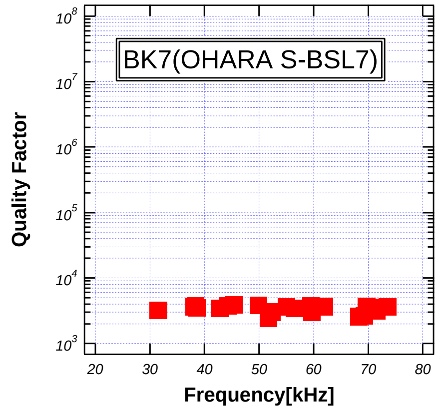

Figure B.6: Quality factors of BK7.

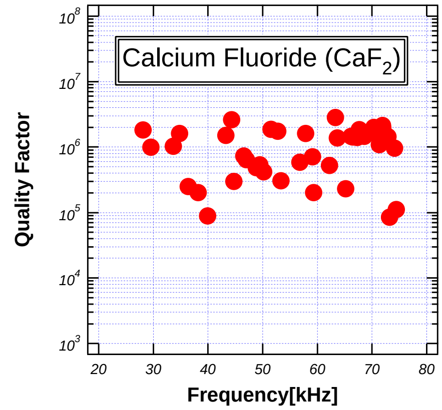

Figure B.7: Quality factors of CaF_2.

previous subsection for silicon and sapphire. Therefore, the measured maxima should be regarded as lower limits of the intrinsic quality factors of our CaF_2 sample.

Discussion

We conjecture that the relatively low quality factor of BK7 originates in its more complicated composition than the other materials here[2]. Surely, its main composition is SiO_2, but its chemical properties are different from those of fused silica. For example, the softening point of the BK7 is 718°C, while that of fused silica is about 1600°C. In the field of glass production, there is a presumption that the quality factor of glass at room temperature has positive correlation with the distance from its softening temperature. The low quality factor in BK7 might be correlated with this presumption.

As for CaF_2 , its quality factor has to be further investigated, preparing a more appropriate sample for our setup. However, it was apparent that CaF_2 has much smaller Brownian noise than BK7, if the two are used as mirror substrates as we did in the main experiment of this thesis.

B.3.4 Coating loss

Measured sample

Our nodal support system was applied to measure the mechanical loss due to optical coating. A fused silica disk with 130-mm diameter and 1-mm thick was measured using the nodal support system before and after depositing an optical coating on one of its two flat surfaces. The exact trade name of the fused silica disk is ED-A from Tosoh

[2]Estimated compositions are as follows: SiO_2: 70%, B_2O_3: 10%, K_2O: 8%, Na_2O: 8%, BaO: 3%.

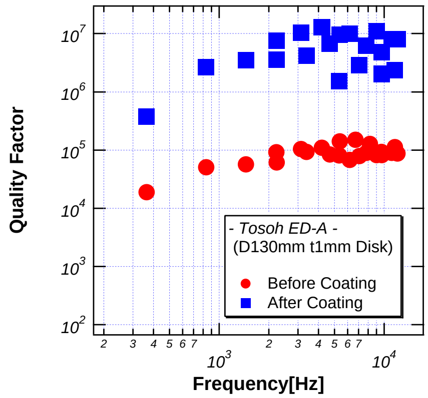

Figure B.8: Quality factors of fused silica disk before and after the coating.

Quartz Products. The sample was commercially polished including its edges. The optical coating is done at National Astronomical Observatory (NAO) in Japan using the Ion Beam Sputtering (IBS) method[3]. Its layers are made of SiO_2/Ta_2O_5, which is the most popular coating in the field of detection of gravitational wave detectors. The thickness of the coating was 5 μm. Some changes in our support system was required to support the thin disk, however, its principle was maintained.

Measured quality factor

Figure B.8 shows the measured quality factor of a fused silica disk with and without coating. While the quality factors were reaching 10^7 before applying the coating, the quality factors degraded by about two orders of magnitude.

Discussion

Because the bulk ED-A sample has a quality factor of 2×10^7 at 30 kHz, the measured quality factors of the disk before the coating were believed to be limited by the surface loss. By interpreting the increase in the loss by the coating as due to the coating itself, the coating loss was calculated. The averaged additional loss was $\phi = 1.2 \times 10^{-5}$ in the disk. By converting the additional loss to the loss in the coating[4], the coating loss was calculated as,

$$\phi_{\mathrm{coat}} = 5.2 \times 10^{-4}, \tag{B.5}$$

with a correction of the difference of Young's Modulus between the substrate and the coating. This coating loss is larger than the coating losses that have been reported by other groups [84, 85]. The possible explanation is that the additional loss was introduced by the metal jig for the coating machine, or the coating loss might be dependent

[3]This work was supported by Dr. Kouich Waseda at NAO.

[4]We have to consider the ratio of the stored strain energy between the bulk and the coating, and have to multiply a correction factor with the measured additional loss to calculate the coating loss. In our case, the correction factor was 66.7.

on the coating process. The bulk loss may be decreased by high temperature during the coating process as we proved in the annealing experiment in the bulk sample, making it difficult to interpret the measured additional loss. Further experiments and careful analysis are ongoing to investigate the coating loss. The nodal support system is also applied to the measurement of the coating loss at cryogenic temperature by the other researcher.

Bibliography

[1] A. Einstein, S.B. Preuss. Akad. Wiss, 154 (1916).

[2] J.H. Taylor and J.M. Weisberg, Astrophys. J., 345 (1989) 434.

[3] A. Abramovici *et al.*, *Science*, 256 (1992) 325.

[4] The VIRGO Collaboration, *VIRGO Final Design Report*, (1997).

[5] K. Danzmann *et al.*, *Max-Plank-Institut für Quantenoptik Report*, (1994).

[6] K. Tsubono, *Gravitational Wave Experiments*, World Scientific, pp.122 (1995).

[7] H.B. Callen and T.A. Welton, Phys. Rev., 83 (1951) 34.

[8] R.F. Greene and H.B. Callen, Phys. Rev., 83 (1951) 1231.

[9] H.B. Callen and R.F. Greene, Phys. Rev., 86 (1952) 702.

[10] R.F. Greene and H.B. Callen, Phys. Rev., 88 (1952) 1387.

[11] P.R. Saulson, Phys. Rev. D, 42 (1990) 2437.

[12] V.B. Braginsky *et al.*, Phys. Lett. A, 264 (1999) 1.

[13] Y. Levin, Phys. Rev. D, 57 (1998) 659.

[14] N. Nakagawa *et al.*, Rev. Sci. Inst., 68 (1997) 3553.

[15] Y.T. Liu and K.S. Thorne, Phys. Rev. D, 62 (2000) 122002.

[16] M. Cerdonio *et al.*, Phys. Rev. D, 63 (2001) 082003.

[17] V.B. Braginsky, V.P. Mitrofanov, V.I. Panov, Systems with Small Dissipation, Univ. Chicago Press, Chicago, (1985).

[18] J.E. Logan *et al.*, Phys. Lett. A, 161 (1991) 101.

[19] W.J. Startin *et al.*, Rev. Sci. Inst., 69 (1998) 3681.

[20] M. Taniwaki *et al.*, Phys. Lett. A, 246 (1998) 37.

[21] A.M. Gretarsson and G.M. Harry, Rev. Sci. Inst., 70 (1999) 4081.

[22] S. Rowan *et al.*, Phys. Lett. A, 265 (2000) 5.

[23] K. Numata *et al.*, Phys. Lett. A, 276 (2000) 37.

[24] K. Numata *et al.*, Phys. Lett. A, 284 (2001) 162.

[25] M. Kajima *et al.*, Phys. Lett. A, 264 (1999) 251.

[26] K. Yamamoto *et al.*, Phys. Lett. A, 280 (2001) 289.

[27] G.I. González and P.R. Saulson, Phys. Lett. A, 201 (1995) 12.

[28] H. Hirakawa and K. Narihara, Phys. Rev. Lett., 35 (1975) 330.

[29] J. Weber, Phys. Rev. Lett., 22 (1969) 1320.

[30] C.W. Misner, K.S. Thorne and J.A. Wheler, *Gravitation*, WH. Freeman and Company (1970).

[31] K. Tsubono, *Status of TAMA project*, Japanese Journal of the Physical Society of Japan, 54-5 (1999) p. 328 (in Japanese).

[32] K. Danzmann *et al.*, LISA Pre-Phase A Report – Second Edition, MPQ233, July (1998),

[33] N. Seto *et al.*, Phys. Rev. Lett., 87 (2001) 221103.

[34] V.B. Braginsky *et al.*, Phys. Lett. A, 271 (2000) 303.

[35] M. De Rosa *et al.*, Phys. Rev. Lett., 89 (2002) 237402.

[36] N. Mio, in: *Detection of gravitational waves.* (in Japanese), p. 197-229, eds: T. Nakamura, N. Mio, M. Ohashi, Kyoto University Academy Press (1998), ISBN: 4-87698-032-2.

[37] H. Nyquist, Phys. Rev., 32 (1928) 110.

[38] J.R. Hutchinson, J. Appl. Mech., 47 (1980) 901.

[39] G.W. McMahon, J. Acoust. Soc. Am., 36 (1964) 85.

[40] A. Gillespie and F. Raab, Phys. Rev. D, 52 (1995) 577.

[41] F. Bondu and J-Y. Vinet, Phys. Lett. A, 198 (1995) 74.

[42] K. Yamamoto, Ph.D. thesis, University of Tokyo, (2000).

[43] F. Bondu *et al.*, Phys. Lett. A, 246 (1998) 227.

[44] N. Nakagawa *et al.*, Phys. Rev. D, 65 (2002) 102001F.

[45] C. Zener, Phys. Rev., 52 (1937) 230.

[46] C. Zener *et al.*, Phys. Rev., 53 (1938) 100.

[47] R.H. Randall *et al.*, Phys. Rev., 56 (1939) 343.

[48] L.D. Landau and E.M. Lifshits, *Theory of Elasticity*, third ed. Pergamon, Oxford, (1986).

[49] T. Suzuki *et al.*, Phys. Lett., 67A (1978) 151.

[50] W. Duffy Jr., J. Appl. Phys., 72 (1992) 5628G.

[51] A.de Waard *et al.*, Physica B, 280 (2000) 535.

[52] J. Kovalik and P.R. Saulson, Rev. Sci. Inst., 64 (1993) 2942.

[53] S. Rowan *et al.*, Phys. Lett. A, 227 (1997) 153.

[54] G. Cagnoli *et al.*, Phys. Lett. A, 255 (1999) 230.

[55] K. Numata *et al.*, Class. Quantum. Grav., 19 (2002) 1697.

[56] E. Black, http://www.ligo.caltech.edu/docs/T/T980052-00.pdf.

[57] F. Benebid *et al.*, J. Opt. B: Quantum Semiclass. Opt., 2 (2000) 172.

[58] G. Cella *et al.*, Phys. Lett. A, 266 (2000) 1.

[59] V. Leonhardt *et al.*, Class. Quantum. Grav., 19 (2002) 1717.

[60] B.W. Barr *et al.*, Class. Quantum. Grav., 19 (2002) 1655.

[61] A. Abramovici *et al.*, Phys. Lett. A, 218 (1996) 157.

[62] R.W.P. Drever *et al.*, Appl. Phys. B, 31 (1983) 97.

[63] http://www.ohara-inc.co.jp/b/b02/b0201_op/b0201bsl/sbsl7e.htm.

[64] LIGO Project, LIGO II Conceptual Project Book, http://www.ligo.caltech.edu/docs/M/M990288-A1.pdf.

[65] K. Kuroda *et al.*, Int. J. Mod. Phys. D, 8 (1999) 557.

[66] http://www.oken.co.jp/indexe.html.

[67] http://www.soc-ltd.co.jp/.

[68] http://www.sigma-koki.com/english/index.html.

[69] http://www.ohara-inc.co.jp/b/b02/b0210_cz/b0210.htm.

[70] M. Musha *et al.*, Opt. Comm., 183 (2000) 165.

[71] S. Marka *et al.*, Class. Quantum. Grav., 19 (2002) 1605.

[72] A. Takamori, Ph.D. thesis, University of Tokyo, (2002).

[73] N. Mio *et al.*, Jpn. J. Appl. Phys., 40 (2001) 426.

[74] D. Shoemaker *et al.*, Phys. Rev. D, 38 (1988) 423.

[75] K. Kawabe, Ph.D. thesis, University of Tokyo, (1998).

[76] D.H. Douglass, *Gravitational Wave Experiments*, Proc. the Academia Nazionale dei Lincei International Symposium on Experimental Gravitation, September, 1976, Pavia, Italy, Accademia nazionale dei Lincei, pp. 323 (1977).

[77] Heraeus-Amersil Corporation, 3473 Satellite Boulevard, Duluth, GA 30136-5821, http://www.heraeus.com.

[78] Corning Incorporated Advanced Material Division, 334 Country Route 16 Canton, NY 13617, http://www.corning.com.

[79] Tosoh Quartz Corporation, 3-1435 Tachiyagawa, Yamagata-shi, Yamagata, Japan 990-2251, http://www.tosoh.com.

[80] Shin-etsu Quartz Product Corporation, 1-22-2 Nishi-shinjyuku, Shinjyuku-ku, Tokyo, Japan 160-0023.

[81] D.F. McGuigan *et al.*, J. Low. Temp. Phys., 30 (1978) 621.

[82] G.W. Gibbons and S.W. Hawking, Phys. Rev. D, 4 (1971) 2191.

[83] S. Traeger *et al.*, All-Reflective Interferometry for Gravitational-Wave Detection, in: Sydney Meshkov(Ed.), Proc. Third Edoardo Amaldi Conference, Pasadena, California, July 1999, American Institute of Physics, p. 385.

[84] D.R.M. Crooks *et al.*, Class. Quantum. Grav., 19 (2002) 883.

[85] G.M. Harry *et al.*, Class. Quantum. Grav., 19 (2002) 897.

Acknowledgement

I would like to express my thanks to all people who supported the completion of this work. It would have been impossible to perform this work without the support from many people.

First of all, I am deeply thankful to Prof. Kimio Tsubono, my supervisor, for letting me to do everything that I wanted. He encouraged me every time when I lost my confidence. I am also indebted to Dr. Masaki Ando, who is the research associate of Tsubono group, for his scientific insights. I am sure that without his appropriate advice and expertise it would have taken much longer time to reduce many of the noise sources. I want to express my thanks to Dr. Kazuhiro Yamamoto who helped me with his immense knowledge of thermal noise. Many parts of this work are based on his achievements on inhomogeneous loss. I am grateful to Mr. Akiteru Takamori who helped me technically and morally. He was very cooperating for everything. I must acknowledge Dr. Koji Arai who is a team member of TAMA. I learnt from him great attitude for research as well as scientific sophistication. I greatly appreciate Dr. Keita Kawabe, who was a research associate of Tsubono group. If he was not an in inspiring teacher when I was an undergraduate student, I would not have chosen gravitational waves as my research field.

I am also grateful to Mr. Shigemi Otsuka and Mr. Yoshikatsu Nanjyo, engineers in the department of physics. All mechanics used for my experiment, including even screws, were made by their diligent of effort. I have to thank Dr. Riccardo DeSalvo, at California Institute of Technology, who is a dynamic person. He encouraged me for everything and the list is so long that it cannot be stated here. I am also grateful to Prof. Eugene W. Cowan, at California Institute of Technology, for improving the English presentations throughout this thesis.

This research was supported in part by Research Fellowships of Japan Society for the Promotion of Science for Young Scientists, and by a Grant-in-Aid for Creative Basic Research of the Ministry of Education.

Finally, I would like to specially thank my family, parents and my sister, for their warm support for many years.